

Copyright
by
Taylor Caldwell Green IV
2008

**The Dissertation Committee for Taylor Caldwell Green IV Certifies that this is the
approved version of the following dissertation:**

**Simulation of Reactor Pulses in Fast Burst and Externally Driven
Nuclear Assemblies**

Committee:

Steven Biegalski, Co-Supervisor

Erich Schneider, Co-Supervisor

Sheldon Landsberger

Oscar Gonzalez

Michael Webber

**Simulation of Reactor Pulses in Fast Burst and Externally Driven
Nuclear Assemblies**

by

Taylor Caldwell Green IV, B.S.; M.S.

Dissertation

Presented to the Faculty of the Graduate School of

The University of Texas at Austin

in Partial Fulfillment

of the Requirements

for the Degree of

Doctor of Philosophy

The University of Texas at Austin

May, 2008

Dedication

To Bopha, and my parents Taylor and Conceicao.

Acknowledgements

Thanks to Edward Parma, Richard Coats, Michael Gregson, and James Dahl of Sandia National Laboratories for providing impetus, support, and Sandia Pulsed Reactor data vital to this research. Thanks also to my graduate supervisors, Steven Biegalski and Erich Schneider, and coordinator of the nuclear program Sheldon Landsberger, for their guidance and support. I thank professor Oscar Gonzalez for providing me the requisite background in the numerical treatment of differential equations used to perform this research. Finally, I thank professor Michael Webber for supporting this research and propelling these abstract concepts into a more functional context.

Simulation of Reactor Pulses in Fast Burst and Externally Driven Nuclear Assemblies

Publication No. _____

Taylor Caldwell Green IV, PhD.

The University of Texas at Austin, 2008

Supervisor: Steven Biegalski and Erich Schneider

The following research contributes original concepts to the fields of deterministic neutron transport modeling and reactor power excursion simulation. A deterministic neutron transport code was created to assess the value of new methods of determining neutron current, fluence, and flux values through the use of view factor and average path length calculations. The neutron transport code is also capable of modeling the highly anisotropic neutron transport of deuterium-tritium fusion external source neutrons using diffusion theory with the aid of a modified first collision source term. The neutron transport code was benchmarked with MCNP, an industry standard stochastic neutron transport code.

Deterministic neutron transport methods allow users to model large quantities of neutrons without simulating their interactions individually. Subsequently, deterministic methods allow users to more easily couple neutron transport simulations with other physics simulations. Heat transfer and thermoelastic mechanics physics simulation modules were each developed and benchmarked using COMSOL, a commercial heat

transfer and mechanics simulation software. The physics simulation modules were then coupled and used to simulate reactor pulses in fast burst and externally driven nuclear assemblies.

The coupled system of equations represents a new method of simulating reactor pulses that allows users to more fully characterize pulsed assemblies. Unlike older methods of reactor pulse simulation, the method presented in this research does not require data from the operational reactor in order to simulate its behavior. The ability to simulate the coupled neutron transport and thermo-mechanical feedback present in pulsed reactors prior their construction would significantly enhance the quality of pulsed reactor pre-construction safety analysis. Additionally, a graphical user interface is created to allow users to run simulations and visualize the results using the coupled physics simulation modules.

Table of Contents

| | |
|--|-----|
| List of Tables | x |
| List of Figures | xi |
| Chapter 1: Introduction | 1 |
| 1.1 Background | 1 |
| 1.2 Problem Statement | 6 |
| 1.3 Literature Review | 12 |
| 1.4 Summary | 13 |
| Chapter 2: Theory | 15 |
| 2.1 Finite Difference Solution | 15 |
| 2.2 Cross Sections | 24 |
| 2.3 Multi-Group Neutron Diffusion and Kinetics Equations | 40 |
| 2.4 Heat Transfer Equations | 66 |
| 2.5 Mechanics Equations | 70 |
| Chapter 3: Neutronics Benchmarking | 75 |
| 3.1 First Test Scenario | 77 |
| 3.2 Second Test Scenario | 92 |
| Chapter 4: Heat Transfer Benchmarking | 110 |
| Chapter 5: Mechanics Benchmarking | 117 |
| Chapter 6: SPR Pulse Simulation | 127 |
| Chapter 7: ZEDNA Pulse Simulation | 145 |
| Chapter 8: Conclusions | 154 |
| Appendix A: PRS User Manual | 158 |
| A.1 PRS Setup | 158 |
| A.2 Point Source Simulation | 158 |
| A.3 Criticality Calculation | 162 |

| | |
|-----------------------|-----|
| A.4 PRS Plotter | 164 |
| References..... | 167 |
| Vita | 172 |

List of Tables

| | |
|---|-----|
| Table 2.1: Energy bins for each of the group structures. | 29 |
| Table 2.2: Percentage of each energy bin spanned by the average elastic scattering collision in each group. | 37 |
| Table 6.1. FWHM and maximum temperature for pulses with varying initial reactivity (Ford, 2003). | 127 |
| Table 6.2. Critical pulse parameters from PRS and SPR experimental data (Ford, 2003). | 143 |
| Table 7.1. Critical pulse parameters from PRS for several ZEDNA pulse simulations. | 151 |

List of Figures

| | |
|---|----|
| Figure 1.1: Comparison of pulse profiles between SPR-III and a hypothetical EDNA system. | 4 |
| Figure 1.2: Proposed layout of ZEDNA system. | 5 |
| Figure 2.1: Arrangement of nodes in the finite difference scheme..... | 16 |
| Figure 2.2: Arrangement of nodes in unbalanced finite difference scheme. | 19 |
| Figure 2.3: Flux weighting spectra versus fission energies. | 26 |
| Figure 2.4: Total cross section values for ^{235}U , ^{238}U , and Mo. | 30 |
| Figure 2.5: Total cross section values for assemblies made of HEU..... | 31 |
| Figure 2.6: Total cross section values for assemblies made of LEU. | 32 |
| Figure 2.7: Fission cross section values for ^{235}U and ^{238}U | 33 |
| Figure 2.8: Fission cross section values for assemblies made of HEU. | 34 |
| Figure 2.9: Fission cross section values for assemblies made of LEU..... | 35 |
| Figure 2.10: Naming conventions of each of the simulation boundaries. | 44 |
| Figure 2.11: Illustration of the ring to ring view factor calculation..... | 47 |
| Figure 2.12: Illustration of the ring to ring neutron path length calculation..... | 49 |
| Figure 2.13: ^{235}U elastic scattering cross sections as a function of energy and scattering angle for 7 groups. | 53 |
| Figure 2.14: ^{238}U elastic scattering cross section as a function of energy and scattering angle for 7 groups. | 54 |
| Figure 2.15: Mo elastic scattering cross section as a function of energy and scattering angle..... | 55 |

| | |
|---|----|
| Figure 2.16: Point source illustration..... | 58 |
| Figure 2.17: Point source leakage scenarios..... | 61 |
| Figure 2.18: Illustration of the ring to hole neutron path length calculation..... | 65 |
| Figure 2.19: Cutaway view of the SPR III reactor..... | 71 |
| Figure 3.1: Direction of external source neutrons relative to the area simulated..... | 78 |
| Figure 3.2: Average flux with the planar neutron source..... | 79 |
| Figure 3.3: Average flux with the point neutron source..... | 81 |
| Figure 3.4: Cumulative sample cavity fluence after 10 μ s with the planar neutron source. | 83 |
| Figure 3.5: Cumulative sample cavity fluence after 10 μ s with the point neutron source. | 84 |
| Figure 3.6: Sample cavity fluence over time with the planar neutron source..... | 85 |
| Figure 3.7: Sample cavity fluence over time with the point neutron source..... | 86 |
| Figure 3.8: Radial flux profile at several times for the planar neutron source..... | 87 |
| Figure 3.9: Axial flux profile at several times for the planar neutron source..... | 89 |
| Figure 3.10: Radial flux profile at several times for the point neutron source..... | 90 |
| Figure 3.11: Axial flux profile at several times for the point neutron source..... | 91 |
| Figure 3.12: Criticality values predicted by PRS for HEU assemblies as time step size is reduced..... | 93 |
| Figure 3.13: Criticality values predicted by PRS for LEU assemblies as dt is reduced. .. | 94 |
| Figure 3.14: Criticality values predicted by PRS for HEU assemblies as grid resolution is increased..... | 95 |

| | |
|--|-----|
| Figure 3.15: Criticality values predicted by PRS for LEU assemblies as grid resolution is increased. | 96 |
| Figure 3.16: Criticality predicted by MCNP and PRS for HEU assemblies with different group structures..... | 97 |
| Figure 3.17: Criticality predicted by MCNP and PRS for LEU assemblies with different group structures..... | 98 |
| Figure 3.18: Two group neutron energy spectrum for assemblies made of HEU. | 99 |
| Figure 3.19: Three group neutron energy spectrum for assemblies made of HEU. | 101 |
| Figure 3.20: Four group neutron energy spectrum for assemblies made of HEU. | 102 |
| Figure 3.21: Five group neutron energy spectrum for assemblies made of HEU..... | 103 |
| Figure 3.22: Six group neutron energy spectrum for assemblies made of HEU. | 104 |
| Figure 3.23: Two group neutron energy spectrum for assemblies made of LEU..... | 105 |
| Figure 3.24: Three group neutron energy spectrum for assemblies made of LEU..... | 106 |
| Figure 3.25: Four group neutron energy spectrum for assemblies made of LEU..... | 107 |
| Figure 3.26: Five group neutron energy spectrum for assemblies made of LEU. | 108 |
| Figure 3.27: Six group neutron energy spectrum for assemblies made of LEU..... | 109 |
| Figure 4.1: Convergence of PRS temperature profiles with decreasing time step size. . | 111 |
| Figure 4.2: Convergence of PRS temperature profiles with decreasing dx..... | 112 |
| Figure 4.3: COMSOL and PRS temperature profiles after 1 ms. | 113 |
| Figure 4.4: COMSOL and PRS temperature profiles after 10 ms. | 114 |
| Figure 4.5: COMSOL and PRS temperature profiles after 0.1 seconds. | 115 |
| Figure 4.6: COMSOL and PRS temperature profiles after 1 s. | 116 |
| Figure 5.1: Time step convergence of the mechanics module..... | 118 |

| | |
|---|-----|
| Figure 5.2: Time step convergence of COMSOL..... | 119 |
| Figure 5.3: Grid resolution convergence for PRS..... | 120 |
| Figure 5.4: Displacement of the outer radius of the assembly, 100 μ s..... | 121 |
| Figure 5.5: Displacement of the outer radius of the assembly, 1 ms..... | 122 |
| Figure 5.6: Displacement of the inner radius of the assembly, 100 μ s..... | 123 |
| Figure 5.7: Displacement of the inner radius of the assembly, 1 ms..... | 124 |
| Figure 5.8: Displacement profile comparison..... | 125 |
| Figure 6.1: Outer radius expansion during a pulse with a 50 μ s FWHM (Ford, 2003).. | 128 |
| Figure 6.2: Inner and outer radius fuel plate expansion during a typical pulse (Ford, 2003). | 129 |
| Figure 6.3: Inner and outer radius tangential stress values (Ford, 2003)..... | 130 |
| Figure 6.4: 4.5 cent pulse simulations with various mechanics energy deposition limits. | 132 |
| Figure 6.5: 4.5 cent pulse simulations with various neutronics time step sizes..... | 133 |
| Figure 6.7: Pulse power plot from a PRS simulation of a SPR reactor pulse with an initial prompt reactivity of 4.5 cents. | 137 |
| Figure 6.7: Inner and outer radius expansion following a 4.5 cent pulse. | 137 |
| Figure 6.8: Inner and outer radius tangential stress following a 4.5 cent pulse..... | 138 |
| Figure 6.9: Pulse power plot from a PRS simulation of a SPR reactor pulse with an initial prompt reactivity of 13.4 cents. | 140 |
| Figure 6.10: Inner and outer radius expansion following 13.4 cent pulse..... | 141 |
| Figure 6.11: Inner and outer radius tangential stress following 13.4 cent pulse. | 142 |

| | |
|---|-----|
| Figure 7.1: ZEDNA pulse power with a source size of 10^{13} neutrons..... | 147 |
| Figure 7.2: Maximum assembly temperature throughout the ZEDNA pulse with a source size of 10^{13} neutrons..... | 148 |
| Figure 7.3: Inner and outer radius expansion following a pulse with a source size of 10^{13} neutrons..... | 149 |
| Figure 7.4: Inner and outer radius tangential stress following a pulse with a source size of 10^{13} neutrons. | 150 |
| Figure A.1: Graphical user interface for the PRS program. | 159 |
| Figure A.2: Graphical user interface for the PRSplotter program. | 165 |

Chapter 1: Introduction

1.1 BACKGROUND

The Sandia Pulsed Reactor (SPR) is a fast burst reactor made of highly enriched uranium (HEU) that is used to simulate weapons effects. Due to the closure of the SPR reactor in October 2006 there is a need to develop a system using a core made of low enriched uranium (LEU) that can provide a fast neutron spectrum with short pulse durations and a large experimental cavity. The use of LEU in a fast burst reactor would significantly reduce the security costs associated with its use. Externally driven nuclear assemblies (EDNA), have been studied since the 1960's (Groce, 1967; Coats, 1969; Lee, *et al.*, 1990; Griffin, *et al.*, 1994). An EDNA system is a nuclear assembly that operates below super prompt criticality that magnifies an external source of neutrons.

Older concepts proposed systems where electrons would strike a high-Z target to generate gamma rays that would then produce photoneutrons. The photoneutrons would then be multiplied by a nuclear assembly operating below super prompt criticality. Physics experiments were performed; however, no large scale machine was built. The appeal of these systems was their potential to deliver very short pulse widths due to the short pulse width of the external neutron sources.

It is necessary to present the terminology used to describe reactor operations. The rate at which the neutron population in a reactor changes can be described by its k_{eff} value, otherwise known as the reactor criticality. Equation 1-1 is used to find the k_{eff} value (Ott, 1985).

$$k_{eff} = \frac{n(t)}{n(t - \ell)} \quad (1-1)$$

Where n is the neutron population, t is time, and ℓ is the average amount of time between a neutron's birth through fission and death through leakage or absorption. When k_{eff} is greater than 1 the reactor is super-critical. Reactors with k_{eff} values less than 1 are known as sub-critical.

Neutrons produced through the decay of fission fragments represent 0.65 percent of all neutrons produced through fission of ^{235}U atoms (Lamarsh, 2001). Neutrons produced from the decay process are known as delayed neutrons because they appear long after the fission occurs. Delayed neutrons can appear roughly 1 s to several minutes after the fission. Delayed neutrons do not appear during μs time frames in which pulses occur. The symbol β is used to indicate the delayed neutron fraction. The β value for ^{235}U is used whenever a β value is needed because ^{235}U is much more likely to fission than ^{238}U .

A reactor in which the k_{eff} value is greater than 1 without the aid of delayed neutrons is called super prompt critical. During SPR pulses the reactor is super prompt critical. Since neutron lifetimes are very short k_{eff} values never exceed 1 by large amounts. It is most convenient to refer to the margin that k_{eff} exceeds 1 by referencing the reactivity value. Equation 1-2 is used to calculate the reactor reactivity above a k_{eff} value of 1 in cents.

$$\rho = 100 \frac{k_{eff} - 1}{\beta} \quad (1-2)$$

If the k_{eff} value used in the reactivity calculation was calculated without delayed neutrons the reactivity value can be referred to as the prompt reactivity. All of the reactivity and k_{eff} values throughout this text will be calculated without delayed neutrons.

At the beginning of a SPR reactor pulse the reactor will operate at a very low power with a prompt reactivity ranging from 4 to 15 cents. The reactor power will rise quickly and heat up the fuel. Thermal expansion of the fuel will decrease its density and increase the likelihood of neutron leakage instead of fission. The thermal expansion will drive the reactor criticality below 1 and end the reactor pulse. ZEDNA pulses begin operation with criticality above the super critical level but below the super prompt critical level. The reactor serves to boost the external neutron source but the thermal expansion is not necessary to shut down the runaway chain reaction. ZEDNA reactors will be brought to the sub-super prompt critical level shortly before the external source is fired. After the pulse is finished the ZEDNA reactor criticality will be lowered by the removal of reflectors. Figure 1.1 shows what a pulse from an EDNA system with a very short external source pulse width could look like in comparison with a SPR reactor pulse.

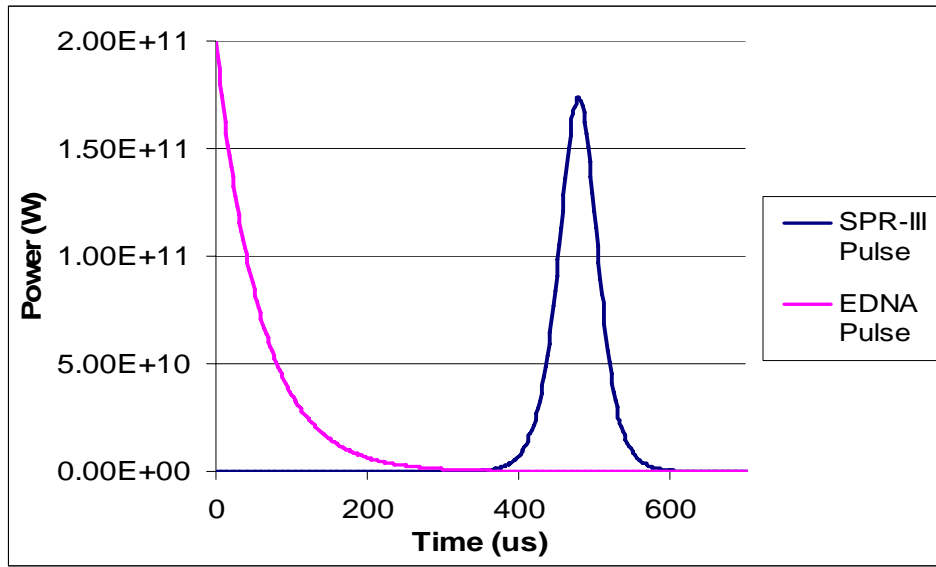


Figure 1.1: Comparison of pulse profiles between SPR-III and a hypothetical EDNA system.

More recent studies at Sandia (Dorsey, *et al.*, 2005) have proposed different types of externally driven nuclear assembly concepts that utilize LEU. Previous LEU fast burst reactors have had undesirable pre-initiation and pulse width characteristics. The higher incidence of pre-initiation is caused by the fact that spontaneous fission occurs more often in ^{238}U than ^{235}U , and LEU assemblies must be much larger than HEU assemblies that deliver the same amount of energy per pulse. The larger amount of ^{238}U causes a stronger background neutron source that results in pulse initiation before the correct amount of reactivity can be inserted. The larger pulse widths of LEU fast burst reactors may be attributed to the larger dimensions of these assemblies and a lower total macroscopic fission cross section due to the increased ^{238}U content.

The Sandia Z Machine externally driven nuclear assembly (ZEDNA) concept uses an LEU assembly coupled with the Sandia Z Machine to produce a neutron field for

weapons effects testing similar to the one produced by the SPR reactor. In the ZEDNA concept the Z-Machine is pulsed with a D-T gas puff target. The pulse is boosted by an LEU core positioned near the target as shown in Figure 1.2.

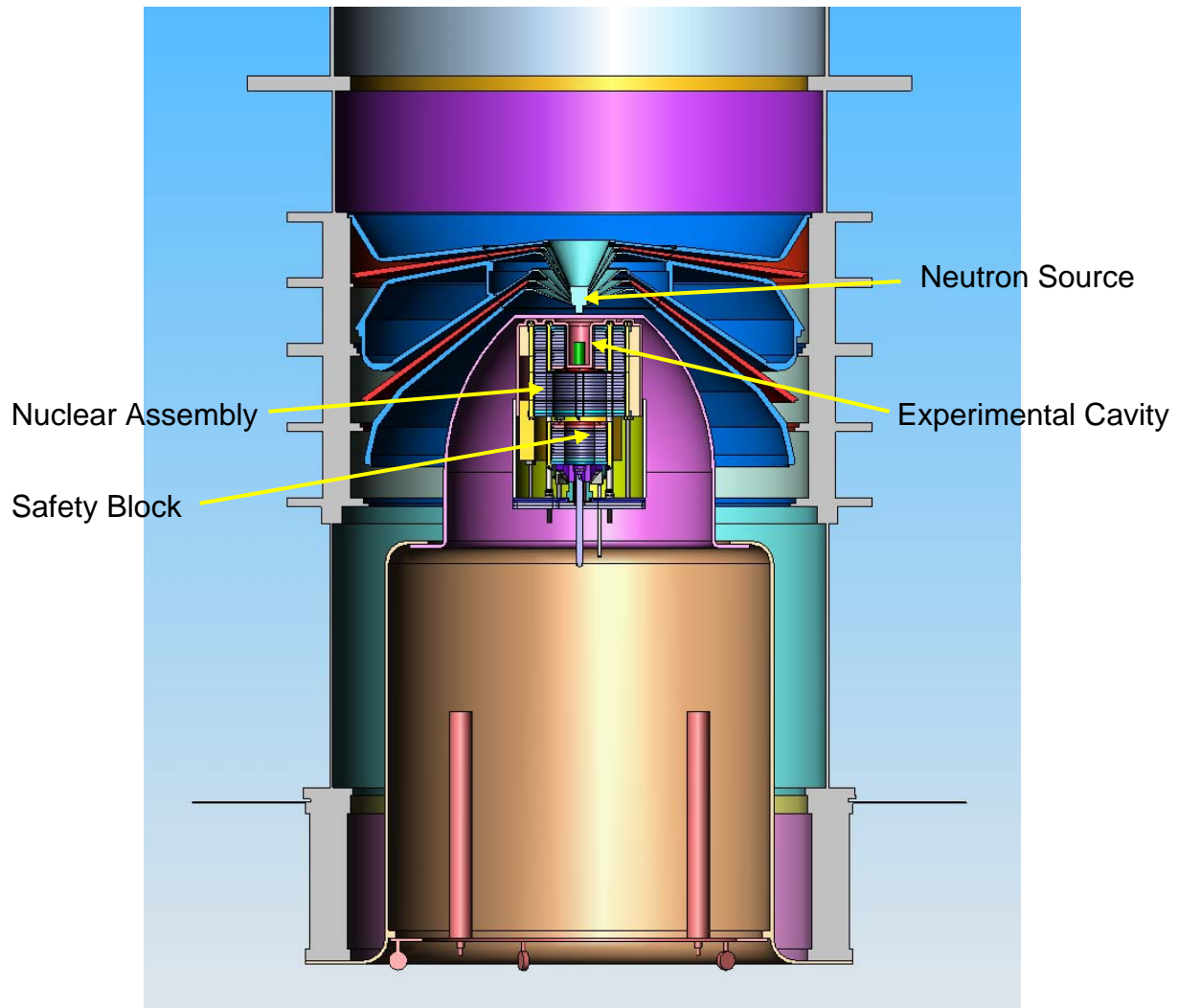


Figure 1.2: Proposed layout of ZEDNA system.

The resulting neutron field inside an experimental cavity within the LEU core would be similar to that of the SPR reactor. This research will provide a tool versatile enough to aid in the design of the ZEDNA reactor or other similar fast burst assemblies.

1.2 PROBLEM STATEMENT

The purpose of this work is to create a computer code, referred to as PRS (Pulsed Reactor Simulator) that will aid in the design of an externally driven nuclear assembly. PRS will implement the finite difference method to solve the coupled heat transfer, thermoelastic and neutronics equations. Currently, there is no program that solves the multi-group spatially and temporally dependant neutron diffusion equation coupled with the appropriate thermomechanical equations governing fast burst reactors.

PRS will also include the effects of conduction in the thermomechanical equations despite the fact that most other reactor kinetics solutions assume adiabatic heating. Conduction effects are included to calculate more accurate temperature profiles of pulses that last on the order of milliseconds in assemblies with very large thermal conductivity values. The user friendly graphical user interface will allow one to benchmark PRS with available fast burst reactor data or simulate new designs such as ZEDNA.

PRS will allow the user to characterize a reactor pulses or determine assembly criticality with 24 parameters, including:

- assembly dimensions
 - inner radius (cm)

- outer radius (cm)
- height (cm)
- fuel plate thickness (cm)
- mechanics constants
 - modulus of elasticity (GPa)
 - Poisson's ratio
 - uranium density (g cm^{-3})
 - molybdenum density (g cm^{-3})
 - coefficient of thermal expansion (K^{-1})
- neutron source description
 - planar, point, or uniformly distributed volume source
 - point source height above the assembly (cm)
 - source neutrons, for planar or point sources (n)
 - initial power, for volumes sources (MW)
- heat transfer constants
 - thermal conductivity ($\text{W m}^{-1} \text{K}^{-1}$)
 - specific heat ($\text{J kg}^{-1} \text{K}^{-1}$)
- simulation information
 - uranium enrichment, 93 or 19.9 weight percent
 - conduction heat transfer, on or off
 - pulse simulation or criticality calculation
 - criticality calculation tolerance

- length of pulse simulation
- data output frequency, pulse simulation only
- time step multiplication factor
- grid spacing multiplication factor
- number of neutron energy groups, from 1 to 6, not including the 14 MeV

ZEDNA source group

PRS will solve the neutron transport and thermoelastic equations governing reactors simultaneously in order to accurately model pulses. The partial differential equations for neutronics, heat transfer, and mechanics will be discretized spatially and temporally. Modules for each partial differential equation will take in information from the solution of the other partial differential equations, move forward one time step, and then feed information into the other modules. The pulse simulation will move forward by one time step in each module and pass data to the next module to simulate the next time step.

Reactor pulses typically begin at low power and then ramp up very quickly. The temperature rise and subsequent thermal expansion modeled in the heat transfer and mechanics modules provide the negative feedback that decrease the fission rate modeled by the neutronics module and shut down the reactor pulse. Typically, reactor pulses are simulated using the Nordheim-Fuchs model, seen in equations 1-3, 1-4, and 1-5 (Hetrick, 1971; Ott, 1985).

$$\frac{dP(t)}{dt} = \frac{[\rho(t) - \beta]}{\ell} P(t) \quad (1-3)$$

$$\rho(t) = \rho_0 - \alpha_T T(t) \quad (1-4)$$

$$T(t) = T_0 + \frac{\int_0^t P(t) dt}{m c_p} \quad (1-5)$$

Where

- P is the reactor power. (W)
- α_T is the negative temperature reactivity feedback coefficient. ($\Delta\rho \text{ K}^{-1}$)
- T is the temperature. (K)
- m is fuel mass. (kg)
- c_p is the specific heat. ($\text{J kg}^{-1} \text{ K}^{-1}$)

The Nordheim-Fuchs model allows one to avoid thermal expansion calculations through the use of a reactivity feedback coefficient. This feedback coefficient is found only by the use of empirical data from existing nuclear reactors. The lack of empirical data for reactor designs that have not yet been built or tested is the first problem that severely hinders the application of the Nordheim-Fuchs model to new pulsed reactor designs.

The second problem with the Nordheim-Fuchs model is that it does not provide any information about several important reactor pulse parameters such as temperature, displacement, stress, and sample cavity fluence. PRS does not use the Nordheim-Fuchs model and thus avoids the use of dubious catchall feedback coefficients, modeling reactor

pulse events in a more direct manner. Other reactor pulse simulations have used the results from the Nordheim-Fuchs model to calculate fuel expansion values (Wilson, 2006). However, these simulations still rely on the negative reactivity feedback coefficient to capture the effect of thermal expansion on the reactor criticality.

A more realistic simulation does require more computational time. However, it provides a much more comprehensive characterization of reactor pulse behavior. The multi-group spatially and temporally dependant neutron diffusion equation is used in lieu of the Nordheim-Fuchs model to model neutron transport and multiplication in PRS. The diffusion equation feeds information to a separate set of partial differential equations that determine reactor temperatures and thermal expansion values. Distortions in the shape of the reactor from thermal expansion then influence the next iteration of the neutron diffusion equation. Additionally, use of the diffusion equation allows one to model ZEDNA reactors, where the pulse power begins at its peak, with the introduction of an external neutron source term. PRS calculates the neutron flux profile throughout the reactor while avoiding the use of empirically determined reactivity feedback coefficients.

PRS will solve for the following variables:

- neutron flux ($\text{n s}^{-1} \text{ cm}^{-2}$)
- neutron energy spectrum ($\text{n s}^{-1} \text{ cm}^{-2} \text{ group}^{-1}$)
- sample cavity fluence (n cm^{-2})
- sample cavity neutron energy spectrum ($\text{n cm}^{-2} \text{ group}^{-1}$)
- temperature (K)
- radial expansion (cm)

- stress (MPa)

PRS simulations will be run using an executable that will function on any modern Microsoft Windows computer. Output from PRS simulations can be manipulated using another executable with a graphical user interface named PRSplotter. A user manual for both programs may be found in Appendix A.

PRS requires that the reactor is shaped in the form of a hollow cylinder. The neutron flux profile must exhibit angular symmetry. The assembly fuel must be 90 weight percent uranium and 10 weight percent molybdenum. The uranium enrichment must either be 93 or 19.9 weight percent. Constants associated with the simulation of neutron transport change as the balance of molybdenum, ^{235}U and ^{238}U change. PRS is capable of simulating different fuel compositions and enrichments if additional neutron transport simulation constants are included.

1.3 LITERATURE REVIEW

Literature regarding nuclear assemblies subject to energy pulses on the order of several MJ over roughly 100 μ s is limited. Most prior fast burst reactor analysis made use of the point-kinetics equations (Hansen, 1952; Wimett, 1960; Hetrick, 1971; Wilson, 2006). This research will rely on a time dependant multi-group neutron diffusion equation coupled with the appropriate temperature and mechanics equations to predict the behavior of EDNA systems (Lamarsh, 2001; Wimett, 1992). The point-kinetics equations are ill-suited for the analysis of these LEU assemblies due to the assembly's larger dimensions, initial asymmetric neutron flux profile, and the lack of experimentally determined data such as the temperature reactivity feedback coefficient.

Studies have been conducted on the thermomechanical effects of rapid power transients in the SPR II, SPR III, and Lady Godiva reactors (Hansen, 1952; Burgreen, 1962; Reuscher, 1969, 1971, 1973; Wimmert, 1992; Miller, 1994). However, these analyses were dependant on experimentally determined parameters. Typically the initial reciprocal burst positive period or the fuel temperature coefficient of reactivity was required for analysis. This research will use explicit versions of equations derived by Wimmert for the analysis of thermomechanical effects.

The use of a time dependant multi-group neutron diffusion equation and the appropriate thermoelastic equations will make the research applicable to reactor design problems because of the reduced the need for experimentally determined parameters. It is critical that one is capable of accurately predicting an assembly's behavior pre-operation with stringent modern safety standards.

1.4 SUMMARY

PRS will solve a coupled set of partial differential equations that govern heat transfer, thermal expansion, and neutron transport during fast burst and ZEDNA reactor pulses. Chapter two will examine the original research conducted in order to create PRS. Chapter two will first describe the spatial and temporal derivative approximations employed in the finite difference solution of the partial differential equations. Next, the solution methodology employed by the neutronics module is described.

The neutronics module contains several original solutions to neutron transport modeling problems. The inner radius boundary condition makes use of view factor calculations to predict the amount of incoming current. Several modifications were made to the standard first collision external neutron source to allow it to accurately model the source present in ZEDNA reactor pulses. The sample cavity fluence calculations also required an innovative solution methodology that employed view factor calculations.

Once the neutronics module calculations have been described, chapter two will explain the methods used to simulate heat transfer and mechanics. Heat transfer and mechanics partial differential equations were solved using the same finite difference numerical derivative approximations that were used in the neutronics module. The heat transfer module will be capable of simulating conduction and it will assume that fission heating is adiabatic. The mechanics module will model one dimensional radial expansion with zero radial stress boundary conditions.

After the solution methodology is described, chapter three will show the PRS neutronics module benchmarking using the industry standard neutron transport computer code, Monte Carlo N-Particle, MCNP (Briesmeister, 2000). However, since MCNP is not capable of modeling heat transfer or thermal expansion, the remaining modules will be benchmarked using COMSOL in chapters four and five (Zimmerman, 2006).

COMSOL is a commercial multi-physics program that contains built-in physics modules that allow users to quickly simulate a variety of engineering problems. The COMSOL program is equipped with heat transfer and thermal expansion modeling packages, but it is incapable of simulating neutron transport. Next, the three modules are coupled together and PRS is used to simulate SPR reactor pulses in chapter six. PRS simulations are then compared to experimental results. PRS ZEDNA simulations are shown in chapter seven.

Chapter 2: Theory

The solution of this coupled heat transfer, thermal expansion, and neutronics problem requires the simultaneous solution of three partial differential equations. The finite difference method was applied to the problem because of its simplicity and versatility (Burden, 2001). The method used to approximate the derivatives is derived below.

All spatial derivatives were required to allow for a non-uniform mesh, due to the uneven expansion of the fuel plates caused by fission energy deposition. A three point balanced stencil was derived to approximate spatial derivatives between the solution boundaries. When the distance between nodes is even the derivative approximations used to solve the partial differential equations simplify to the center difference method.

A three point unbalanced stencil is used to approximate boundary condition derivatives. An unbalanced stencil is required because there are no nodes beyond the boundaries that can be used to implement the balanced stencil derivative approximation.

2.1 FINITE DIFFERENCE SOLUTION

The coupled set of equations was solved using the finite difference method. Two different temporal numerical derivative approximations were used in the solution. Additionally, two types of spatial derivative approximations were found. For the solution

of the partial differential equations a 3 point balanced stencil was used. A 3 point unbalanced stencil was also derived to approximate derivatives in the boundaries.

2.1.1 Spatial Derivative with Balanced Stencil

The distance between nodes is not always uniform due to thermal expansion of the assembly in the mechanics module. Figure 2.1 illustrates the arrangement of the nodes.

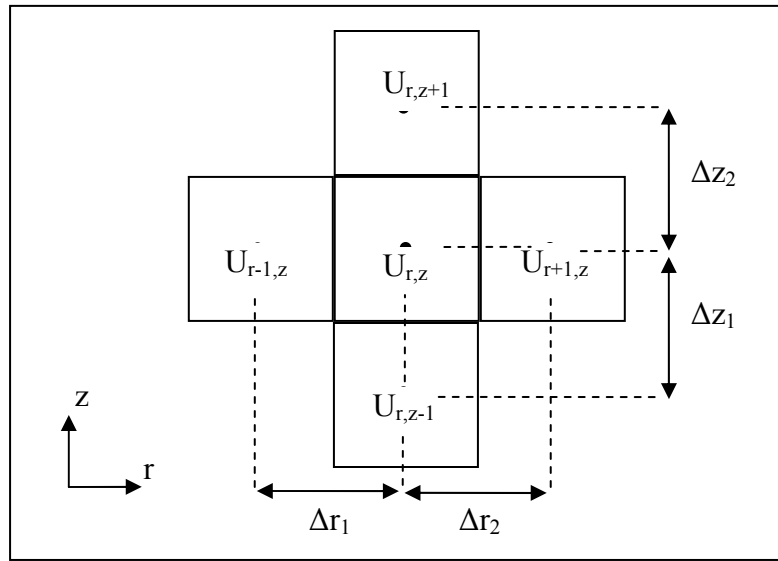


Figure 2.1: Arrangement of nodes in the finite difference scheme.

The first and second derivatives must allow for non-uniform spatial discretization. The first order radial numerical derivative with respect to U using a balanced three point stencil will take the form shown below in equation 2-1.

$$\frac{\partial U}{\partial r_{r,z}} = aU_{r-1,z} + bU_{r,z} + cU_{r+1,z} \quad (2-1)$$

Where a, b, and c are functions of the distance between nodes that will be derived below. The derivation of the first derivative with respect to r at the node $U_{r,z}$ using nodes $U_{r+1,z}$ and $U_{r-1,z}$ is shown below. First we use Taylor series expansion to approximate the values $U_{r-1,z}$ and $U_{r+1,z}$ using the value $U_{r,z}$ and knowledge about the distance between nodes in equation 2-2 (Burden, 2001).

$$\begin{aligned} U_{r-1,z} &= U_{r,z} - \Delta r_1 \frac{\partial U}{\partial r} + \frac{\Delta r_1^2}{4} \frac{\partial^2 U}{\partial r^2} \\ U_{r,z} &= U_{r,z} \\ U_{r+1,z} &= U_{r,z} + \Delta r_2 \frac{\partial U}{\partial r} + \frac{\Delta r_2^2}{4} \frac{\partial^2 U}{\partial r^2} \end{aligned} \quad (2-2)$$

Next we sum the equations after multiplying them by constants a, b, and c as seen in equation 2-3.

$$\begin{aligned} a \cdot U_{r-1,z} + b \cdot U_{r,z} + c \cdot U_{r+1,z} &= U_{r,z} [a + b + c] + \frac{\partial U}{\partial r} [-a \cdot \Delta r_1 + b \cdot \Delta r_2] \dots \\ \dots + \frac{\partial^2 U}{\partial r^2} \left[a \cdot \frac{\Delta r_1^2}{4} + b \cdot \frac{\Delta r_2^2}{4} \right] \end{aligned} \quad (2-3)$$

Now we define the constants a, b, and c such that the sum of the values between the brackets in the first and third terms on the right hand side are equal to zero and the sum of the values between the brackets on the second term on the right hand side is equal to one. The constants a, b, and c are shown below in equation 2-4.

$$\begin{aligned}
 a &= \frac{-\Delta r_2}{\Delta r_1(\Delta r_1 + \Delta r_2)} \\
 b &= \frac{-\Delta r_1 + \Delta r_2}{\Delta r_1 \cdot \Delta r_2} \\
 c &= \frac{\Delta r_1}{\Delta r_2(\Delta r_1 + \Delta r_2)}
 \end{aligned} \tag{2-4}$$

The constants a, b, and c may now be multiplied by the appropriate values to approximate the first derivative of U at location (r, z). To find the finite difference approximation of the second derivative we define the constants in Equation 2-3 such that the first and second terms on the right hand side are equal to zero and the third term is equal to one. The constants required for the second derivative are shown below in equation 2-5.

$$\begin{aligned}
 a &= \frac{2}{\Delta r_1(\Delta r_1 + \Delta r_2)} \\
 b &= \frac{-2}{\Delta r_1 \cdot \Delta r_2} \\
 c &= \frac{2}{\Delta r_2(\Delta r_1 + \Delta r_2)}
 \end{aligned} \tag{2-5}$$

The first derivative approximation is second order convergent. This means that the error in the approximation is inversely proportional to the number of nodes squared. The second derivative is only first order convergent. When the spacing between nodes is uniform the constants for the first and second derivative approximations become the same as those used in the central difference method.

2.1.2 Spatial Derivative with Unbalanced Stencil

Unbalanced finite difference derivative approximations are required to correctly apply boundary conditions that contain spatial derivatives. This differencing scheme must also allow for non-uniform grid spacing because of thermal expansion. Figure 2.2 illustrates the arrangement of the nodes for derivatives at boundary locations.

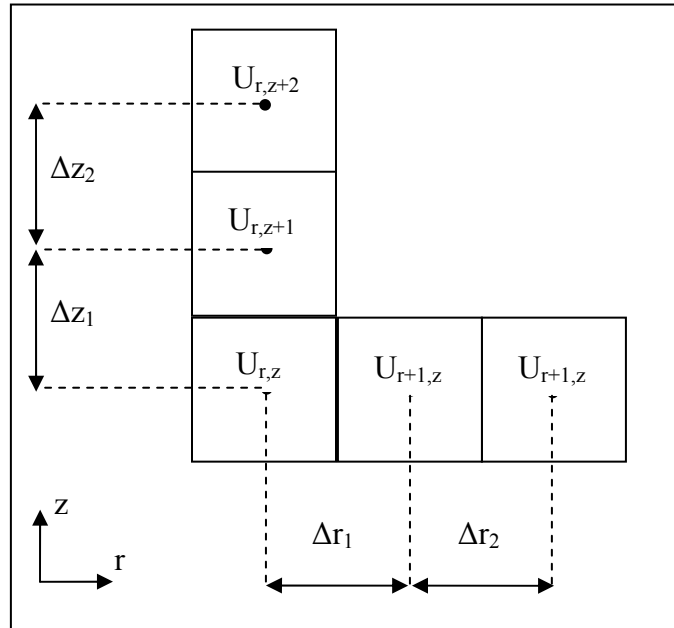


Figure 2.2: Arrangement of nodes in unbalanced finite difference scheme.

The derivation of the first derivative with respect to r at the node $U_{r,z}$ using nodes $U_{r+1,z}$ and $U_{r+2,z}$ is shown below. First we use Taylor series expansion to approximate the values $U_{r+1,z}$ and $U_{r+2,z}$ using the value $U_{r,z}$ and knowledge about the distance between nodes as shown in equation 2-6 (Burden, 2001).

$$\begin{aligned}
 U_{r,z} &= U_{r,z} \\
 U_{r+1,z} &= U_{r,z} + \Delta r_1 \frac{\partial U}{\partial r} + \frac{\Delta r_1^2}{4} \frac{\partial^2 U}{\partial r^2} \\
 U_{r+2,z} &= U_{r,z} + (\Delta r_1 + \Delta r_2) \frac{\partial U}{\partial r} + \frac{(\Delta r_1 + \Delta r_2)^2}{4} \frac{\partial^2 U}{\partial r^2}
 \end{aligned} \tag{2-6}$$

Next we sum the equations after multiplying them by constants a , b , and c as seen in equation 2-7.

$$\begin{aligned}
 a \cdot U_{r,z} + b \cdot U_{r+1,z} + c \cdot U_{r+2,z} &= U_{r,z} [a + b + c] + \frac{\partial U}{\partial r} [a \cdot \Delta r_1 + b \cdot (\Delta r_1 + \Delta r_2)] \dots \\
 \dots + \frac{\partial^2 U}{\partial r^2} \left[a \cdot \frac{\Delta r_1^2}{4} + b \cdot \frac{(\Delta r_1 + \Delta r_2)^2}{4} \right]
 \end{aligned} \tag{2-7}$$

Now we define the constants a , b , and c such that the sum of the values between the brackets in the first and third terms on the right hand side are equal to zero and the sum of the values between the brackets on the second term on the right hand side is equal to one. The constants a , b , and c are shown below in equation 2-8.

$$\begin{aligned}
a &= \frac{-2\Delta r_1 - \Delta r_2}{\Delta r_1(\Delta r_1 + \Delta r_2)} \\
b &= \frac{\Delta r_1 + \Delta r_2}{\Delta r_1 \cdot \Delta r_2} \\
c &= \frac{-\Delta r_1}{\Delta r_2(\Delta r_1 + \Delta r_2)}
\end{aligned} \tag{2-8}$$

The a, b, and c values may be multiplied by the appropriate U values and summed together to approximate the first derivative of U at location (r, z). The finite difference approximation of the second derivative was not required for any of the boundary conditions.

2.1.3 Temporal Derivative for the Neutronics Module

Of the three partial derivatives, the neutronics equation has the most stringent time step requirements to maintain numerical stability, with time step values as low as 10^{-10} seconds for some simulations. In order to ease the numerical stability requirements the backward Euler method was used to discretize the temporal derivative. The equation describing neutron transport and multiplication contains several variables that employ several subscripts and superscripts. Radial and axial locations are denoted by the i and j subscripts respectively. The neutron energy group is signified by the g subscript. The simulation time step is denoted by the n superscript. Equation 2-9 shows how the backwards Euler method is applied to a linear system of equations describing neutron transport and multiplication (Burden, 2001).

$$\begin{aligned}
(A + F)\phi(r, z, E, t) &= \frac{\partial \phi(r, z, E, t)}{\partial t} \\
(A + F)\phi_{i,j,g}^{n+1} + S_{ext,i,j,g}^n &= \frac{\phi_{i,j,g}^{n+1} - \phi_{i,j,g}^n}{\Delta t} \\
\phi_{i,j,g}^{n+1} &= \frac{\phi_{i,j,g}^n + \Delta t S_{ext,i,j,g}^n}{[I - \Delta t(A + F)]}
\end{aligned} \tag{2-9}$$

Where

- **A** is a matrix accounting for neutron diffusion, scattering, and leakage
- **F** is a matrix accounting for fission
- ϕ is the neutron flux ($\text{n cm}^{-2} \text{ s}^{-1}$)
- **S_{ext}** is a vector that adds neutrons to the system from the external source

The matrix sizes quickly became too large to be quickly handled by a desktop computer. Several functions are built into MATLAB to solve large sparse systems of linear equations. The `bicgstab` function employs the biconjugate gradient method to quickly solve large systems of linear equations without storing any matrices (Saad, 2003). To use the MATLAB function, Equation 2-9 is rearranged in the familiar $\mathbf{Ax} = \mathbf{b}$ form and instead of creating any matrices, the vectors \mathbf{Ax} and \mathbf{b} are fed into the MATLAB function. The vector \mathbf{Ax} contains all of the variables and the vector \mathbf{b} consists of constants.

2.1.4 Temporal Derivatives for the Mechanics and Heat Transfer Modules

The time step size requirements for the mechanics and heat transfer modules are much less severe than those for the neutronics module. The heat transfer and mechanics

modules marched forward in time using the forward Euler temporal derivative scheme. The forward Euler method requires much less computational time than the backward Euler scheme. However, it requires very small time step sizes to maintain numerical stability. The forward Euler method is used to reduce the inefficiency of the very small time step size required by the neutronics module by making the solution of the heat transfer and mechanics equations much faster. Equation 2-10 shows how the forward Euler method is applied first and second order temporal derivatives (Burden, 2001).

$$\begin{aligned}
 Af(x,t) &= \frac{\partial f(x,t)}{\partial t} \\
 Af^n &= \frac{f^{n+1} - f^n}{\Delta t} \\
 f_{i,j}^{n+1} &= f^n (I - \Delta t A)
 \end{aligned}
 \tag{2-10}$$

$$\begin{aligned}
 Af(x,t) &= \frac{\partial^2 f(x,t)}{\partial t^2} \\
 Af^n &= \frac{f^{n+1} - 2f^n + f^{n-1}}{\Delta t^2} \\
 f^{n+1} &= f^n (2I + \Delta t^2 A) - f^{n-1}
 \end{aligned}$$

where f is a function that is dependant on space and time. Time step size and grid resolution requirements for the heat transfer and mechanics equations were studied thoroughly to ensure that convergence would be achieved with the use of the parameters required by the neutronics module. The grid structure of the heat transfer module matches the neutronics grid structure. However, the mechanics module requires that the axial node spacing be determined by the thickness of the fuel plates.

The neutron transport modeled in the neutronics module allows PRS to predict the fission energy deposition, which drives the heat transfer and thermal expansion modeled in the subsequent modules. The PRS modules will be presented in the order that they affect reactor pulse power. First the neutron transport causes the neutron population to multiply. Next the heat transfer module increases the reactor temperature. Finally, the mechanics module causes the fuel plates to expand, providing the necessary negative feedback to the neutronics module. However, before the neutronics module can be described, the method of cross section compilation must be explained because of the importance of accurate cross section data to the modeling of neutron transport.

2.2 CROSS SECTIONS

Cross sections describe the probability that a neutron will interact with an atom in a certain way. Cross section values used in the equations described below must be accurate in order to produce a realistic simulation. Cross section values were generated using the NJOY program with point-wise data from the T-2 Nuclear Information Service (MacFarlane 1994). NJOY was used to flux weight the cross sections, taking self shielding effects into account using background cross section (σ_0) values. Equation 2-11 is used within NJOY to find the group averaged cross section (MacFarlane 1994).

$$\sigma_g = \frac{\int_{E_1}^{E_2} \phi(E) \sigma(E) dE}{\int_{E_1}^{E_2} \phi(E) dE} \quad (2-11)$$

where E_1 and E_2 are the lower and upper energies of energy group g respectively. As the size of each energy bin increases, the choice of flux weighting spectrum becomes more important. The neutron energy bins used in PRS are relatively large, so an accurate flux weighting spectrum is essential. NJOY allows users to input their own of flux weighting spectra or use one of the default flux weighting spectra. Custom flux weighting spectra were used to generate the cross sections used in PRS.

MCNP was used to find the neutron energy spectrum of assemblies made of the Uranium Molybdenum material with HEU and LEU. The neutron energy spectrum did not vary widely from one assembly geometry to the next as long as the uranium enrichment remained constant. Figure 2.3 shows the neutron energy spectrum for assemblies with both enrichments along with the neutron energy distribution produced by fission.

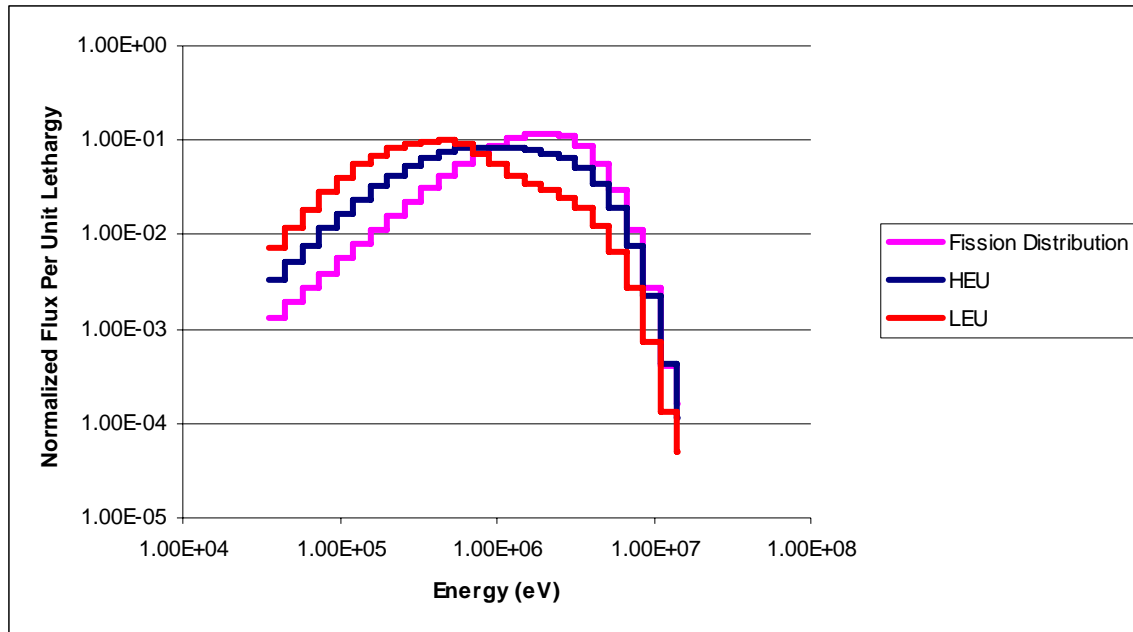


Figure 2.3: Flux weighting spectra versus fission energies.

As the enrichment of the assembly decreases the volume of fuel required to reach criticality increases. Larger assemblies have smaller leakage probabilities, which allow neutrons to scatter to lower energies. The change in leakage probabilities is evident in Figure 2.3 because the HEU system has more low energy neutrons than the fission distribution and the LEU system has more low energy neutrons than the HEU system. The range of neutron energies modeled by PRS ends at 14 MeV, due to the need to accurately model the 14 MeV source neutrons in the ZEDNA pulses. The lowest neutron energy modeled is six lethargy units below 14 MeV. The neutron energy spectrum falls off sharply below 0.03 MeV for assemblies with both levels of enrichment. Lethargy is defined using equation 2-12 (Lamarsh, 2001).

$$u(E) = \ln\left(\frac{E_M}{E}\right) \quad (2-12)$$

where E_M is the highest neutron energy in the system and E is the energy at of the lethargy value. Lethargy increases as the neutron energy decreases below the highest neutron energy. The amount of energy lost in each scattering collision changes with energy. However, the fractional energy loss per collision is independent of the energy of the incident neutron. Neutron lethargy allows one to describe the nonlinear phenomenon of energy losses due to scattering events with linear units.

Before the concept of self shielding may be introduced the reader must first be acquainted with the difference between macroscopic and microscopic cross section values. Microscopic cross sections do not account for the atom density in a given region. Macroscopic cross sections are found using equation 2-13, shown below (Lamarsh, 2001).

$$\Sigma_g = \frac{\sigma_g \rho N_a}{M} \quad (2-13)$$

where ρ is the density of the isotope (g cm^{-3}), N_a is Avogadro's number (atoms mol^{-1}), and M is the weight of the isotope (g mol^{-1}). While an increased abundance of an single isotope amongst many others may not affect the microscopic cross section, it will change the effective group averaged macroscopic cross section.

The σ_0 value approximates the effects of other isotopes in the assembly on the group averaged cross section of a specific isotope (σ_x). σ_0 is the ratio of the total macroscopic cross section of every other isotope divided by the number of atoms of the isotope of interest for a given energy group. If $\sigma_0 \gg \sigma_x$, the intragroup flux will not be changed significantly by σ_x . If $\sigma_0 \ll \sigma_x$, dips will develop in the intragroup flux. Subsequently, the reaction rate and the group averaged cross section will be reduced by the presences of species x.

Calculating the correct value of σ_0 is an iterative process. First one must assume that σ_0 is very large. After the first cross section values are calculated one can find σ_0 . The σ_0 value is used to find a new set of cross sections. The process is then repeated until the σ_0 used to find the cross section values is virtually the same as the one calculated with the new cross sections. Cross section libraries in PRS contain background cross section values ranging from 10^{10} to 10^{-2} . PRS finds the appropriate self shielding value by interpolating between the values available.

Six group different structures were created to describe cross section values between 0.03 and 13.999 MeV. The number of groups in the group structures varied from 1 to 6. The size of each bin was adjusted such that the bins are of equal width in lethargy space. An energy bin is added at 14 MeV to capture source neutrons during ZEDNA simulations. Table 2.1 shows the energy bins for each of the group structures.

Table 2.1: Energy bins for each of the group structures.

| Number of Groups | Energies (eV) | | | | | | |
|------------------|----------------------|----------------------|----------------------|----------------------|----------------------|----------------------|----------------------|
| 1 | 3.49×10^4 | 1.3999×10^7 | | | | | |
| 2 | 3.49×10^4 | 7.02×10^5 | 1.3999×10^7 | | | | |
| 3 | 3.49×10^4 | 2.58×10^4 | 1.91×10^6 | 1.3999×10^7 | | | |
| 4 | 3.49×10^4 | 1.57×10^5 | 7.02×10^5 | 3.15×10^6 | 1.3999×10^7 | | |
| 5 | 3.49×10^4 | 9.50×10^4 | 3.32×10^5 | 1.16×10^6 | 4.04×10^6 | 1.3999×10^7 | |
| 6 | 3.49×10^4 | 9.50×10^4 | 2.58×10^5 | 7.02×10^5 | 1.91×10^6 | 5.18×10^6 | 1.3999×10^7 |
| Source Group | 1.3999×10^7 | 1.4001×10^7 | | | | | |

The following cross sections are used: total, fission, absorption, capture, inelastic scattering, and elastic scattering. The scattering cross section value from each group to each group was also found. All of the PRS cross sections shown below have been calculated with flux weighting and self shielding effects taken into consideration. Figure 2.4 shows the total cross section of ^{235}U , ^{238}U , and Molybdenum.

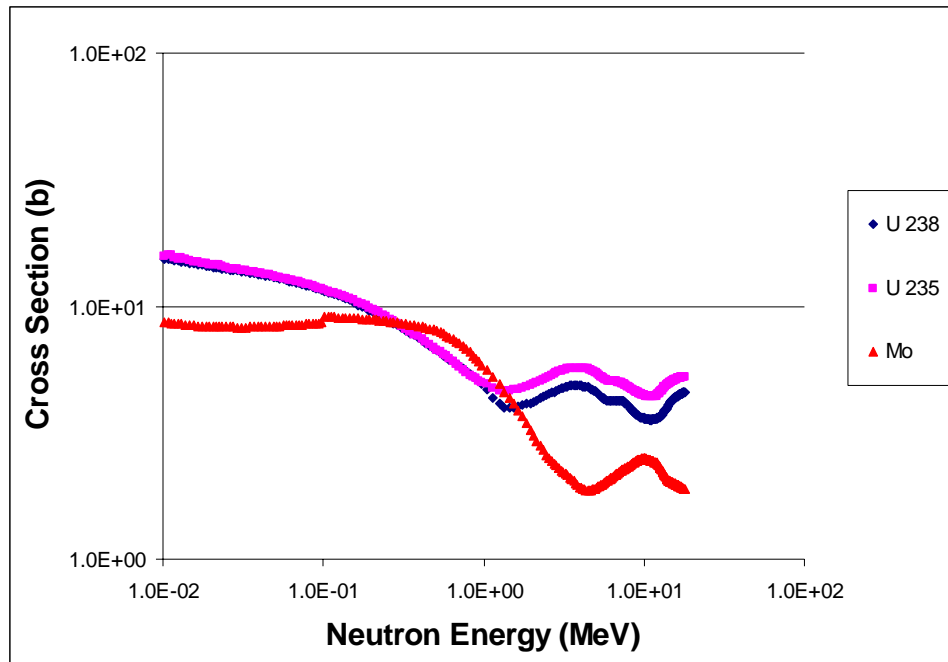


Figure 2.4: Total cross section values for ^{235}U , ^{238}U , and Mo.

The total cross section values do not vary sharply in the range of energies covered by the PRS simulation. All of the MacroscopicFigure 2.5 shows the total cross section values used by PRS for assemblies made of HEU.

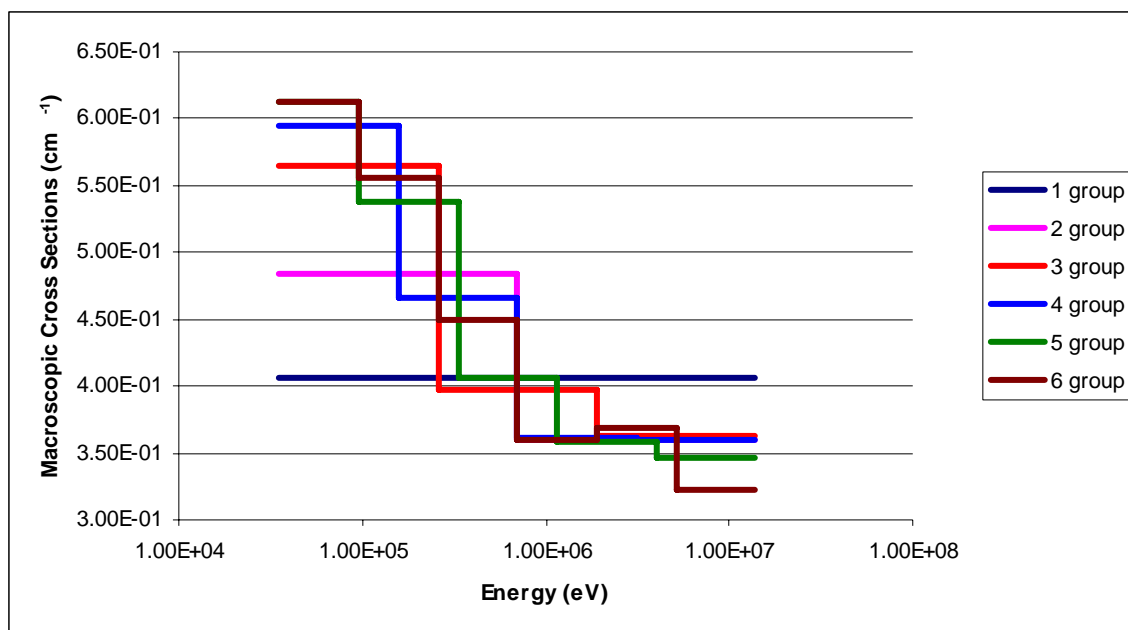


Figure 2.5: Total cross section values for assemblies made of HEU.

It is clear that the total macroscopic cross section values seen in Figure 2.5 change with energy in a fashion similar to the total microscopic cross section values seen in Figure 2.4. It was useful to look for similar sensitivity to energy changes in both the microscopic and macroscopic cross section values to ensure that PRS was using the correct cross section values. Figure 2.6 shows the total cross section values used by PRS for assemblies made of LEU.

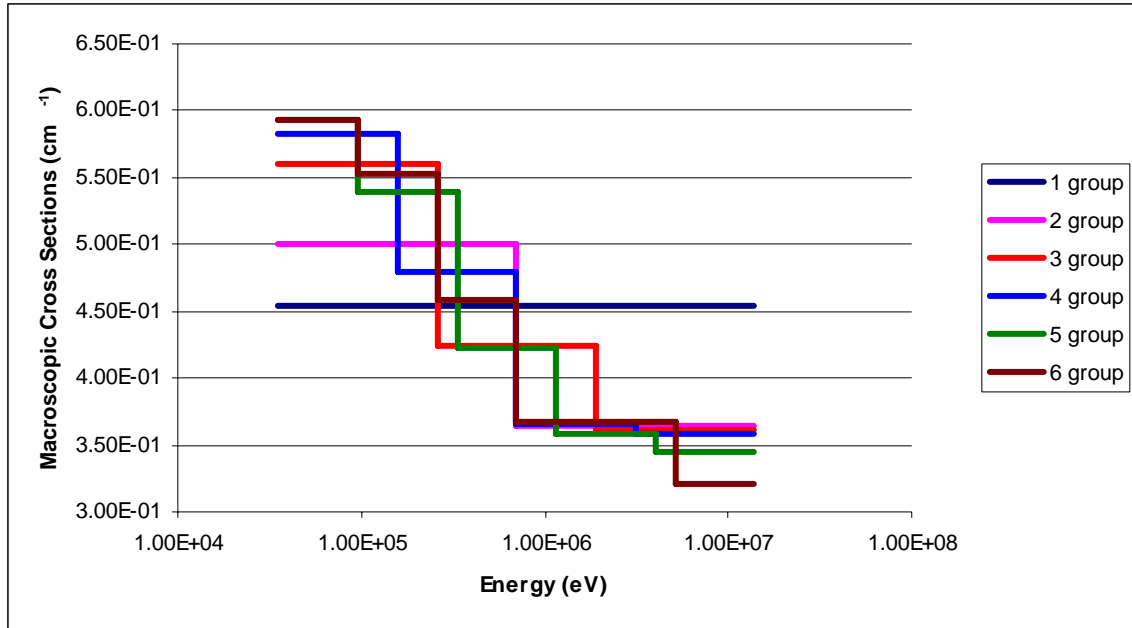


Figure 2.6: Total cross section values for assemblies made of LEU.

The total macroscopic cross sections for LEU and HEU assemblies are very similar. This is to be expected because the differences between ^{238}U and ^{235}U total microscopic cross sections are small. The total cross microscopic sections for ^{238}U and ^{235}U are dominated by their scattering cross sections, which are very similar. Figure 2.7 shows the fission cross sections for ^{235}U and ^{238}U .

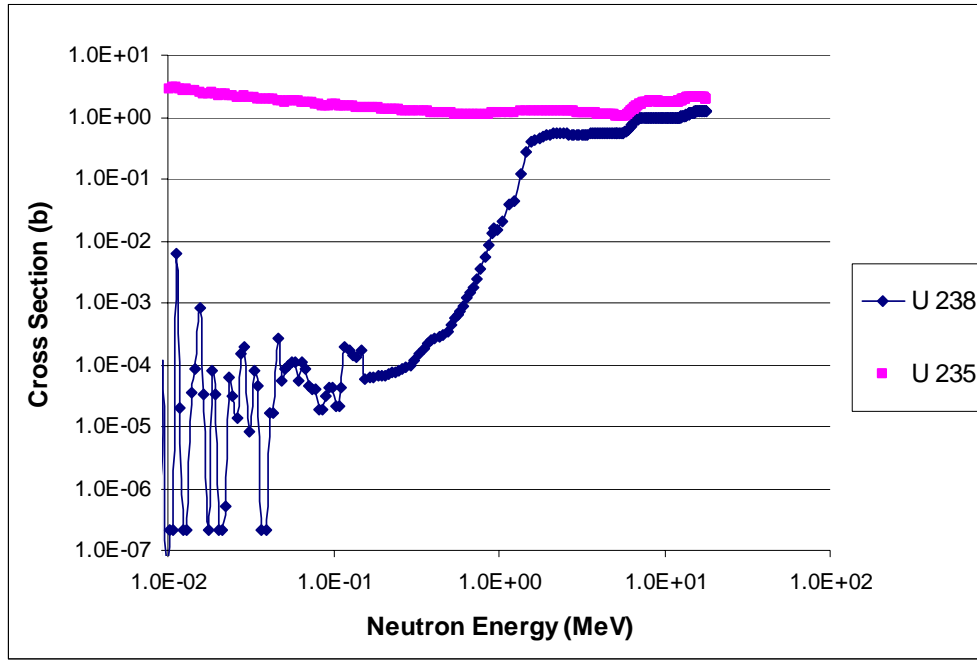


Figure 2.7: Fission cross section values for ^{235}U and ^{238}U .

^{238}U is far less likely to fission than ^{235}U at lower energies. The lower energy groups enter the very beginning of the ^{238}U resolved resonance region for fission cross sections. NJOY handles the convolution of these pointwise cross sections with the flux weighting and self shielding procedure described above.

Cross section resonances are dependent upon temperature due to Doppler broadening (Lamarsh, 2001). The effect of Doppler broadening on reactor performance is greatest if neutrons traverse many decades of energy, and thus many resonances, during the process of slowing down. The neutrons in SPR and ZEDNA reactors do not experience sufficient down scattering before leakage or absorption to cause significant neutron populations at the lower neutron energies where Doppler broadening effects are greatest. Therefore, the PRS group cross sections are not temperature dependent,

although this expedient could be refined in future work. Figure 2.8 shows the fission cross sections used by PRS for assemblies made of HEU.

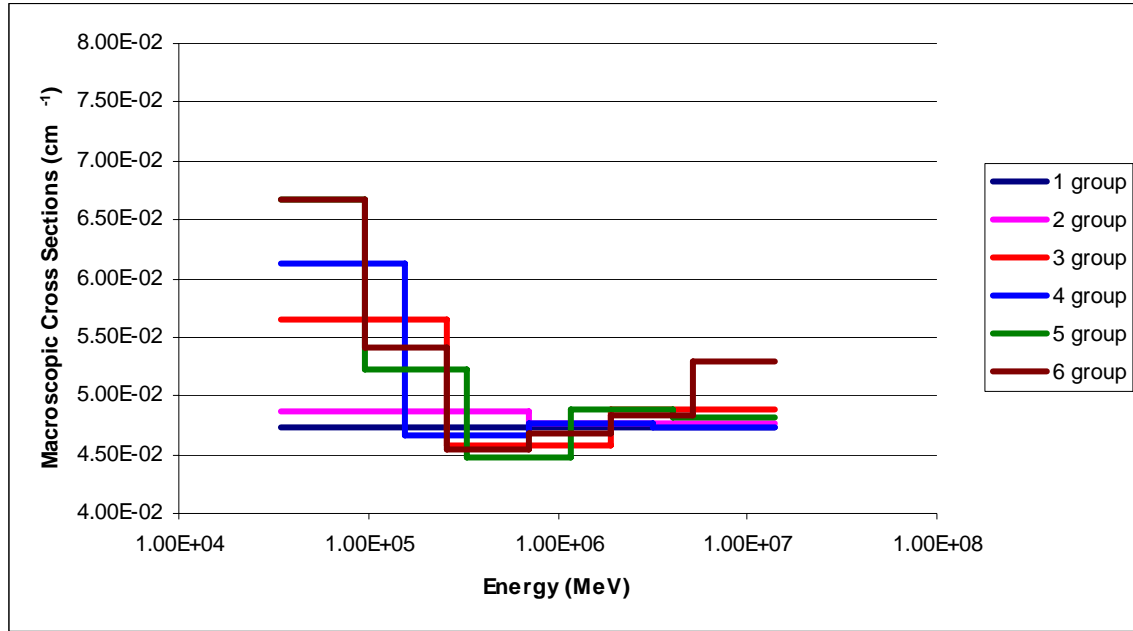


Figure 2.8: Fission cross section values for assemblies made of HEU.

The assembly fission cross section increases at lower energies despite the fact that the ^{238}U fission cross section decreases by several orders of magnitude. The increase in macroscopic fission cross section is due to the abundance of ^{235}U atoms in assemblies made of HEU. Figure 2.9 shows the fission cross sections used by PRS for assemblies made of LEU.

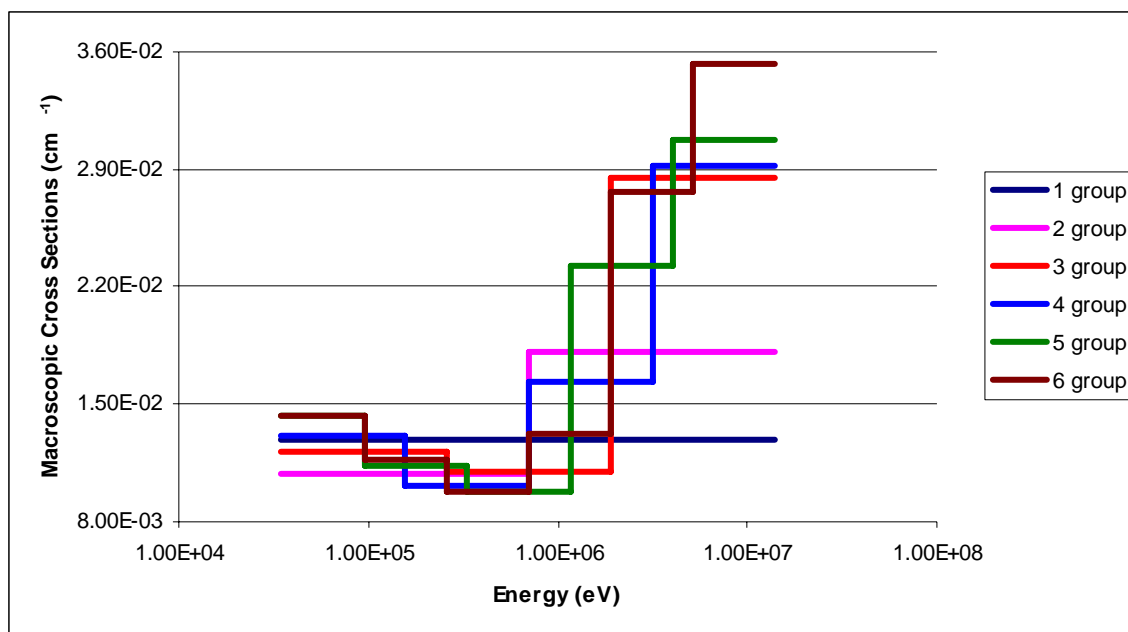


Figure 2.9: Fission cross section values for assemblies made of LEU.

The macroscopic fission cross section is much smaller for assemblies that are made of LEU, especially at lower energy groups. The decrease in fission cross section is a result of the much smaller ^{238}U fission cross section values at energies below 1 MeV as illustrated by Figure 2.7.

The group-to-group scattering cross section values, otherwise known as the scattering kernel, were the most difficult cross section values to calculate. NJOY would produce the total elastic and inelastic scattering cross sections for each group. However, NJOY would only produce the scattering cross section kernel that would yield cross section values from one group to another for elastic scattering and not inelastic scattering cross sections. Instead NJOY would only produce the inelastic scattering kernel for interactions that raised the atom to a given excited state. A person seeking the total

inelastic scattering kernel would have to sum the inelastic scattering kernels from each state together.

Unfortunately, none of the available point wise cross section data that is fed into NJOY had data for the inelastic scattering kernels with residual nuclei in all of the excited states. Raw cross section data from the T-2 Nuclear Information service run by Group T-16 of the theoretical division of Los Alamos National Laboratory was used for this research. Data from the T-2 service had inelastic scattering kernel cross section values for the first 34 excited states for ^{235}U and the first 27 excited states for ^{238}U and no data for scattered neutrons that left the nuclei in the ground state. To compensate for this deficiency scattering kernels from the available excited states were summed together and then scaled to the correct magnitude using the total inelastic scattering cross section values for each group.

Inelastic scattering cross section values were typically much smaller than elastic scattering cross section values. However, inelastic scattering interactions are very important to the accuracy of a simulation because they are far more likely to transfer a scattered neutron to a lower energy group than elastic scattering interactions. The scattering cross section within a given group is larger than any of the intergroup scattering cross sections for any of the group in any of the group structures. Equation 2-11 describes the fractional energy loss of a neutron that scatters elastically (Lamarsh, 2001).

$$\frac{E'}{E} = \frac{A^2 + 2A \cos \theta + 1}{(A + 1)^2} \quad (2-14)$$

The fractional energy loss is affected by the size of the atom and scattering angle of the collision. As atom size increases the ratio of E' and E approaches unity. Equation 2-14 also shows that when the neutron scattering interactions are isotropic, the fractional energy loss varies over a wider range of energies. Calculations within section 2.3.3 made for the external neutron source term will reveal the extent of the anisotropy of neutron scattering interactions modeled in PRS. The anisotropic neutron scattering events result in a very sharp neutron energy loss probability function.

If the peak of the neutron energy loss probability function lies within the group where the scattering event occurred it becomes very difficult to accurately predict the neutron energy spectrum using a deterministic solution. It is now useful to determine if the average elastic neutron scattering collision leaves the scattered neutron in the group in which the interaction occurred. Equation 2-14 was used to find the average energy of elastically scattered neutrons in each group. Table 2.2 shows the percentage of an energy bin spanned by the average elastic scattering collision in each group.

Table 2.2: Percentage of each energy bin spanned by the average elastic scattering collision in each group.

| Energy Bins (MeV) | | Group | HEU | LEU |
|-----------------------|-----------------------|-------|-------|-------|
| 3.49×10^{-2} | 9.50×10^{-2} | 1 | 1 | 1 |
| 9.50×10^{-2} | 2.58×10^{-1} | 2 | 0.88 | 0.86 |
| 2.58×10^{-1} | 7.02×10^{-1} | 3 | 0.68 | 0.68 |
| 7.02×10^{-1} | 1.91×10^0 | 4 | 0.49 | 0.51 |
| 1.91×10^0 | 5.18×10^0 | 5 | 0.27 | 0.25 |
| 5.18×10^0 | 1.3999×10^1 | 6 | 0.14 | 0.12 |
| 1.3999×10^1 | 1.4001×10^1 | 7 | > 100 | > 100 |

Since only a very small fraction of an energy bin is spanned by each elastic scattering collision only neutrons very near the bottom edge of an energy bin have the chance to down-scatter. NJOY attempts to account for all neutron energies within a group in its flux weighting process. The effects of the NJOY flux weighting process are evident from the non-zero elastic down scattering cross section values. However, the large energy bins and highly anisotropic behavior of the high energy neutrons induce error in the flux weighting process. If the scattering was isotropic, neutrons further away from the bottom edge of the energy bin would be able to contribute to down scattering. Additionally, if bins were smaller, the fraction of neutrons in a bin that could contribute to down scattering would increase.

Anisotropic scattering is most prominent in the highest energy groups. The Watt fission spectrum was used to determine what fraction of the fission neutrons are born in groups where down scattering is difficult to model. Equation 2-15 was used to produce the Watt fission spectrum (Lamarsh, 2001).

$$\chi(E) = 0.453e^{-1.036E} \sinh \sqrt{2.29E}$$

$$\int_0^{\infty} \chi(E) dE = 1 \quad (2-15)$$

where $\chi(E)$ is defined such that $\chi(E)*dE$ is the fraction of neutrons with energies between E and $E+dE$, and E is in MeV. According to the Watt fission spectrum, 42 percent of fission neutrons are born in the three highest energy groups defined in Table

2.2 and 80 percent of the neutrons are born in the four highest energy groups. Most neutrons are born in energy groups where down scattering is not modeled well by the coarse neutron energy group structures available.

Deficiencies in the modeling of down scattering will lead to a disproportionate fraction of the neutron population remaining at high energies. Benchmark comparisons with MCNP will allow one to observe the flaws in the coarse group structure modeling of down scattering, and gauge how much the neutron energy spectrum differences affect the accurate prediction of reactor criticality and spatial neutron flux distribution. NJOY will predict the group averaged cross section values that will match MCNP simulations only if the intragroup flux weighting function is very accurate. The function must correctly predict the fraction of the intragroup flux that is in the bottom 1% of the energy bin. Further PRS refinements could include group averaged cross sections for each assembly geometry, made with flux weighting spectra of finer resolution.

The concept of cross sections has been introduced. Several factors influence the accuracy with which group averaged cross sections model neutron transport. Cross section data varies sharply between certain energy values. At different energies cross section data may be represented by a smooth function quite accurately. Deterministic neutron transport models require one to represent cross section data with discrete values that reflect the continuous cross section data within a certain range of energies.

Accurate compilation of discrete cross section data is influence by the choice of flux weighting spectrum, self shielding factor, and the size of the energy bin. As the energy bin width approaches zero, discrepancies between continuous cross section data and discrete values vanish. The correct choice of flux weighting spectrum and self

shielding factors within each group will allow discrete values to correctly model neutron transport. The following section will introduce diffusion theory and describe the modifications that are required to apply diffusion theory to SPR and ZEDNA reactor pulses.

2.3 MULTI-GROUP NEUTRON DIFFUSION AND KINETICS EQUATIONS

The small size and odd shape of the SPR and ZEDNA assemblies presented unique challenges when the diffusion equation was used to model the transport and multiplication of neutrons in these reactors. A unique first collision external source was implemented to accurately simulate the highly anisotropic behavior of a point or planar 14 MeV deuterium-tritium fusion neutron source. The second challenge was to accurately model the re-entrant current from the inner radius of the assemblies. Both of the aforementioned problems were overcome with unique solutions.

2.3.1 Neutron Diffusion Partial Differential Equation

The governing equation for neutron transport and multiplication is shown below in equation 2-16 (Stacey, 2001).

$$D_{i,j,g} \nabla^2 \phi_{i,j,g} - (\Sigma_{a,i,j,g} + \Sigma_{s,i,j,g \rightarrow g-1}) \phi_{i,j,g} + \sum_{h=1}^G \Sigma_{s,i,j,h \rightarrow g} \phi_{i,j,h} + \dots$$

$$\sum_{h=1}^G \chi_{h,g} \nu_h \Sigma_{f,i,j,h} \phi_h + S_{ext,i,j,g} = \frac{1}{\nu_g} \frac{\partial \phi_{i,j,g}}{\partial t} \quad (2-16)$$

$$D_{i,j,g} = \frac{1}{3} (\Sigma_{t,i,j,g} - \Sigma_{s,i,j,g} \mu_g)$$

Where,

- $D_{i,j,g}$ is the diffusion length at location i,j and energy g (cm)
- $\phi_{i,j,g}$ is the flux at location i,j and energy g ($\text{n cm}^{-2} \text{s}^{-1}$)
- $\Sigma_{a,i,j,g}$ is the group-averaged macroscopic absorption cross section at location i,j and energy g (cm^{-1})
- $\Sigma_{t,i,j,g}$ is the group-averaged macroscopic total cross section at location i,j and energy g (cm^{-1})
- $\Sigma_{s,i,j,g \rightarrow g-1}$ is the group-averaged macroscopic scattering cross section at location i,j and energy g to the group below (cm^{-1})
- $\Sigma_{s,i,j,g+1 \rightarrow g}$ is the group-averaged macroscopic scattering cross section at location i,j and energy g from the group above (cm^{-1})
- $\chi_{h,g}$ is the fraction of fission neutrons that occur at energy h that produce neutrons in energy group g
- ν_g is the average number of fission neutrons released as the result of fissions induced by neutrons in the group of interest
- $\Sigma_{f,i,j,g}$ is the group-averaged macroscopic fission cross-section at location i,j and energy g (cm^{-1})

- v_g is the group-averaged neutron velocity (cm s^{-1})
- t is time (s)
- $\Sigma_{s,i,j,g}$ is the group-averaged macroscopic scattering cross section at location i,j and energy g (cm^{-1})
- μ_g is the group-averaged value of the cosine of the angle at which neutrons are scattered in the medium
- $S_{\text{ext},i,j,g}$ is the external neutron source at location i,j and energy g ($\text{n cm}^{-3} \text{s}^{-1}$)

PRS operated under the assumption that the effect of neutron upscattering is negligible. This assumption is valid because all of the group energies are well above thermal energies. Macroscopic cross section values vary at different assembly locations because the density in the assembly is non-uniform due to uneven heating. The neutron diffusion equation works best under three conditions:

- The medium is not a strong absorber
- Scattering is isotropic
- Several free paths away from the edge of an assembly

All three of the conditions are violated to some degree in the majority of the circumstances in the simulations. The effects of violating these conditions are mitigated by the use of a unique external neutron source term and boundary condition. The boundary conditions associated with the neutronics module partial differential equation

are described below. The section following the description of the boundary conditions will describe the external neutron source term.

2.3.2 Neutronics Module Boundary Conditions

At the top, bottom, and outer edges a zero re-entrant flux boundary condition is used. The zero re-entrant flux boundary condition is common, and it is a useful approximation to the actual problem. Neutrons exiting the inner radius of the reactors may either re-enter the assembly at another location along the inner radius or escape the reactor through holes at the top and bottom of the sample cavity. A unique boundary condition was developed for the inner radius that aimed to account for neutron losses from the sample cavity and predict the location and time of flight delay of re-entrant neutrons. Figure 2.10 illustrates the naming conventions of each of the simulation boundaries.

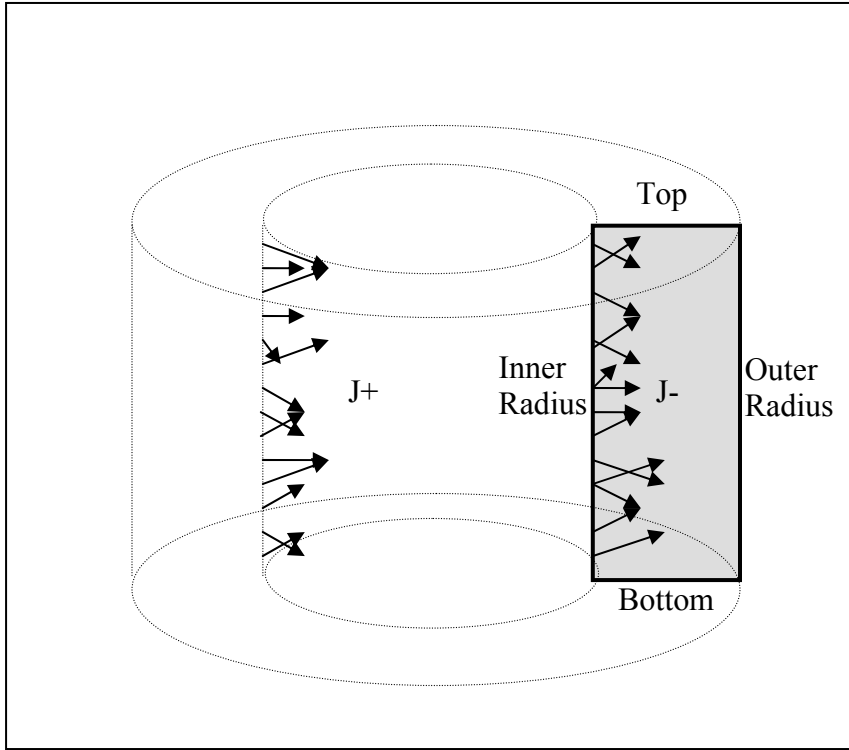


Figure 2.10: Naming conventions of each of the simulation boundaries.

The angular symmetry inherent in the reactors was utilized to reduce the computational workload by simulating only a 2 dimensional slice of the 3 dimensional problem. The shaded region in Figure 2.3 represents simulated area in PRS calculations. Equation 2-17 is used to calculate the re-entrant current given the flux values within the assembly (Stacey, 2001).

$$J^- = \frac{1}{4}\phi + \frac{1}{2}D\frac{\partial\phi}{\partial x} \quad (2-17)$$

Since there is no re-entrant current at the top, bottom, and outer radius boundaries, equation 2-17 may be rearranged to find the flux at the boundaries. Equation 2-18 shows the boundary condition derived from the fact that there is zero re-entrant flux.

$$\phi = 2D \frac{\partial \phi}{\partial x} \quad (2-18)$$

Equation 2-18 may only be used at the top, bottom, and outer radius boundaries because there is a significant amount of re-entrant flux at the inner radius. At the inner radius neutrons may exit the surface and re-enter at another point or escape from the holes in the top and bottom. PRS calculates the current exiting the inner radius, J^+ , using equation 2-19 (Stacey, 2001).

$$J^+ = \frac{1}{4} \phi - \frac{1}{2} D \frac{\partial \phi}{\partial x} \quad (2-19)$$

The exiting current is used in conjunction with view factors, vf , to find the re-entrant current, J . The view factors are used to determine the likelihood that outward current from cell i will re-enter at cell j .

The re-entrant current can not be immediately placed back into the assembly. The time required for the neutron to cross the sample cavity can last several time steps and can have a large effect on the criticality predicted by the model. The only time this effect is negligible is when the cavity is very narrow or if the assembly criticality is exactly

equal to one. If the criticality is greater than one, the incoming current at a given time step is smaller than the exiting current that will eventually re-enter the assembly. Equation 2-20 shows how the re-entrant current at the inner radius at height j, group g, and time n, is found.

$$J_{j,g}^{-,n} = \sum_{t=1}^n \sum_{i=1}^J J_{1,j,g}^{+,t-\frac{\langle|\vec{r}|\rangle(i,j)}{v_g}} v f(i, j) \quad (2-20)$$

In the equation above, the superscript identifies the time. The j subscript indicates the height along the inner radius where neutrons re-enter the assembly. The i subscript denotes the height along the inner radius where the neutron exited the assembly. $\langle|\vec{r}|\rangle$ is the average distance across the sample cavity from node i to node j. v_g is the neutron velocity for neutrons in group g. A neutron's time of flight for a given path length is the ratio of the path length over the neutron velocity. Neutron velocities were found using Equation 2-21 (Lamarsh, 2001).

$$v = \sqrt{\frac{2E}{m}} \quad (2-21)$$

Relativistic effects in the neutron velocity calculation were neglected because the kinetic energy of neutrons at or below 14 MeV is far smaller than the rest mass energy of a neutron. Group energies used in the neutron velocity were flux weighted to ensure that

the neutron velocity assigned to each group best characterized that section of the neutron population.

The view factor calculations required by the inner radius boundary condition were first used to describe radiative heat transfer (Incropera, 2002). The view factor from surface A to surface B is the fraction of isotropically emitted particles from surface A that strike surface B. The view factors used were those for a finite section of a right circular cylinder to another separated finite section. Figure 2.11 illustrates geometry of the ring to ring view factor calculations.

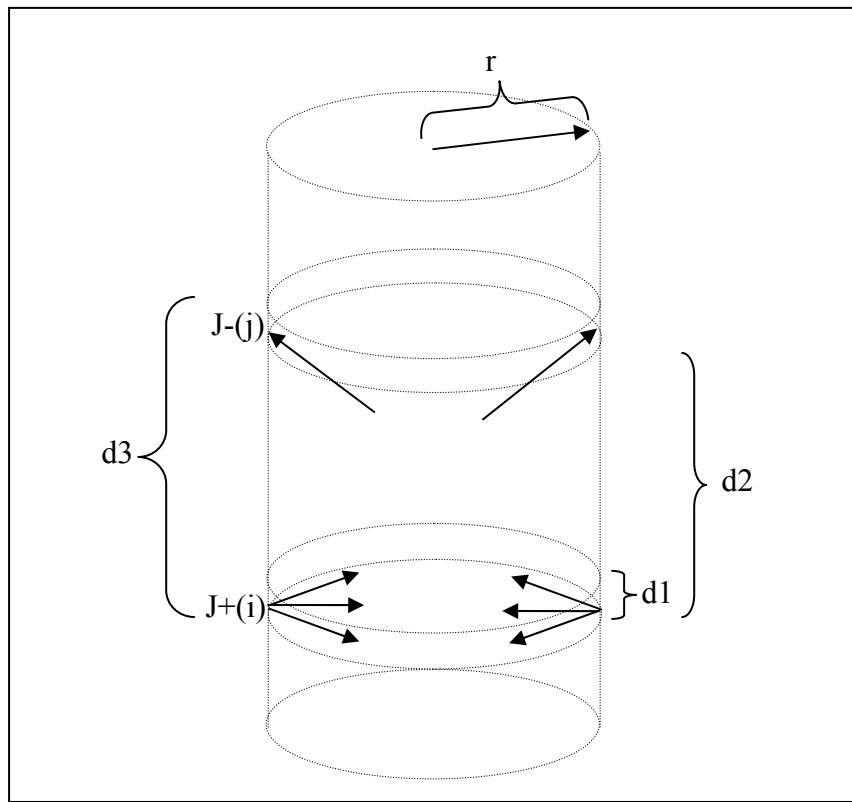


Figure 2.11: Illustration of the ring to ring view factor calculation.

Equation 2-22 is used to find the ring to ring view factors (Buschman, 1961).

$$\begin{aligned}
 L_1 &= d_1 / r \\
 L_2 &= d_2 / r \\
 L_3 &= d_3 / r \\
 X(L) &= (L^2 + 4)^{1/2} \\
 vf(i, j) &= \frac{1}{4(L_3 - L_2)} [2L_1(L_3 - L_2) + (L_3 - L_1)X(L_3 - L_1) - (L_2 - L_1)X(L_2 - L_1) - L_3X(L_3) + L_2X(L_2)]
 \end{aligned} \tag{2-22}$$

Once the likelihood of re-entrance is known the next step is to find the average distance traveled by neutrons leaving ring i and re-entering ring j. Figure 2.12 illustrates the ring to ring neutron path length calculation.

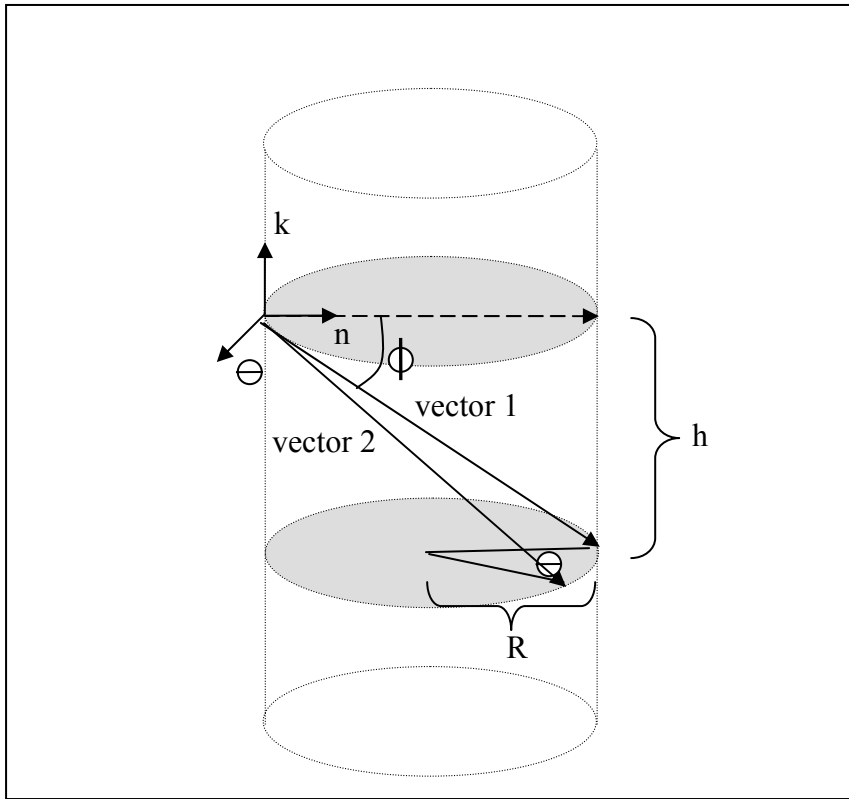


Figure 2.12: Illustration of the ring to ring neutron path length calculation.

When θ is zero the neutron entering the lower node will travel along vector 1. Of the neutrons that exit the assembly at the point shown in Figure 2.5 and re-enter the assembly at the bottom node, more neutrons are likely to enter the lower node near the entry location of vector 1 than the entry location near vector 2. The area around vector 1 is more likely because the solid angle between the exit point and the band with thickness dy represented by the lower shaded region is dependant on the angle θ . As θ approaches 180 degrees the target made by the bottom node vanishes. The average neutron path length between two nodes was found using Equation 2-23, shown below.

$$\begin{aligned}
\tilde{r} &= R(1 + \cos \theta) \hat{n} - h \hat{k} + R \sin \theta \hat{\theta} \\
\cos \phi &= \frac{\tilde{r} \cdot \hat{n}}{|\tilde{r}|} \\
\langle |\tilde{r}| \rangle &= \frac{\int_0^{2\pi} |\tilde{r}| \cos \phi \, d\theta}{\int_0^{2\pi} \cos \phi \, d\theta}
\end{aligned} \tag{2-23}$$

The need for a weighted average of different neutron path lengths may be made clear by studying alternative methods of neutron path length calculations. If one calculates the distance between the rings by finding the distance between two randomly selected points on each ring many times, the distance would be too small. The random points method fails because it does not account for the change in target size as θ increases. Also, if one assumes the distance between the rings was the maximum distance described by vector 1, it would be too large because the neutrons may also re-enter in other places. The ratio of the temporally and spatially dependant re-entrant and exiting flux are found using equations 2-19 and 2-17 respectively, as seen in equation 2-24.

$$JR_{j,g}^n = \frac{J_{1,j,g}^{-,n}}{J_{1,j,g}^{+,n}} \tag{2-24}$$

The right hand side of equation 2-17 (J^-) is set equal to the product of the right hand side of equation 2-19 (J^+) and the ratio of currents. The equation involving the ratio

of currents and the exiting and re-entrant currents is then rearranged to solve for the flux at the inner radius. Equation 2-25 is used to find the flux at the inner radius.

$$\phi_{j,g}^{n+1} = 2D_{j,g} \frac{\partial \phi_{j,g}^n}{\partial x} \frac{(1 + JR_{j,g}^n)}{(1 - JR_{j,g}^n)} \quad (2-25)$$

The inner radius boundary condition shown above is original and it was developed specifically for this application. If PRS predicts a radial flux profile with the correct shape and magnitude, it will confirm the validity of equation 2-25. The external neutron source term will be validated by an axial flux profile of the correct size and shape.

2.3.3 External Neutron Source

An external source term is required because of the highly anisotropic behavior of the neutrons present in the ZEDNA pulse simulations. The anisotropic behavior of the neutrons simulated by PRS was verified by finding the angular dependency of the scattering cross section values. Scattering cross section values as a function of scattering angle were found for each of the energy groups in the group structure with the finest resolution using Equation 2-26, shown below (Lewis, 1993).

$$\begin{aligned}
\sigma_{s,g}(\mu_n) &= \sum_{l=0}^{\infty} (2l+1) \sigma_{s,g,l} P_l(\mu_n) \\
P_0(\mu_n) &= 1 \quad l=0 \\
P_l(\mu_n) &= \frac{1}{2^l l!} \frac{d^l}{d\mu_n^l} (\mu^2 - 1)^l \quad l=1,2,3,\dots
\end{aligned} \tag{2-26}$$

Where,

- $\sigma_{s,g}(\mu_n)$ is the scattering cross section in group g with scattering angle μ_n
- l is the Legendre order
- $\sigma_{s,g,l}$ is the scattering cross section in group g and Legendre order l
- $P_l(\mu_n)$ is the Legendre polynomial

The error in the Legendre polynomial expansion vanishes as the Legendre order approaches infinity. The scattering cross sections for different Legendre orders were generated using NJOY. Figure 2.6 shows the elastic scattering cross section of neutrons incident upon ^{235}U atoms for a range of scattering angles and energies in an assembly made of HEU. The energy group structure used in Figure 2.13 is shown in Table 2.2.

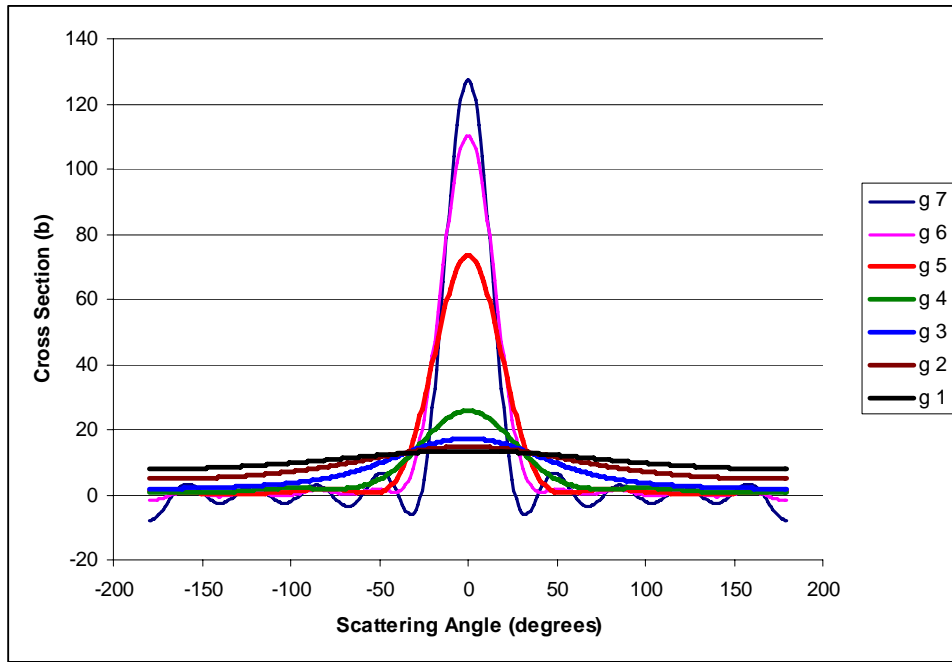


Figure 2.13: ^{235}U elastic scattering cross sections as a function of energy and scattering angle for 7 groups.

The group structure is shown in table 2.2 places the lowest energy values in group 1 and the highest energies in group 7. Figure 2.6 was created using 9th order Legendre polynomials. The negative cross section values are due to the polynomial expansions inability to fully capture the sharp change in cross section values at high energies. The cross section data shows that scattered neutrons, particularly in the three highest groups, are very likely to continue to travel forward. Figure 2.14 shows the elastic scattering cross section of neutrons incident upon ^{238}U atoms for a range of scattering angles and energies in an assembly made of HEU.

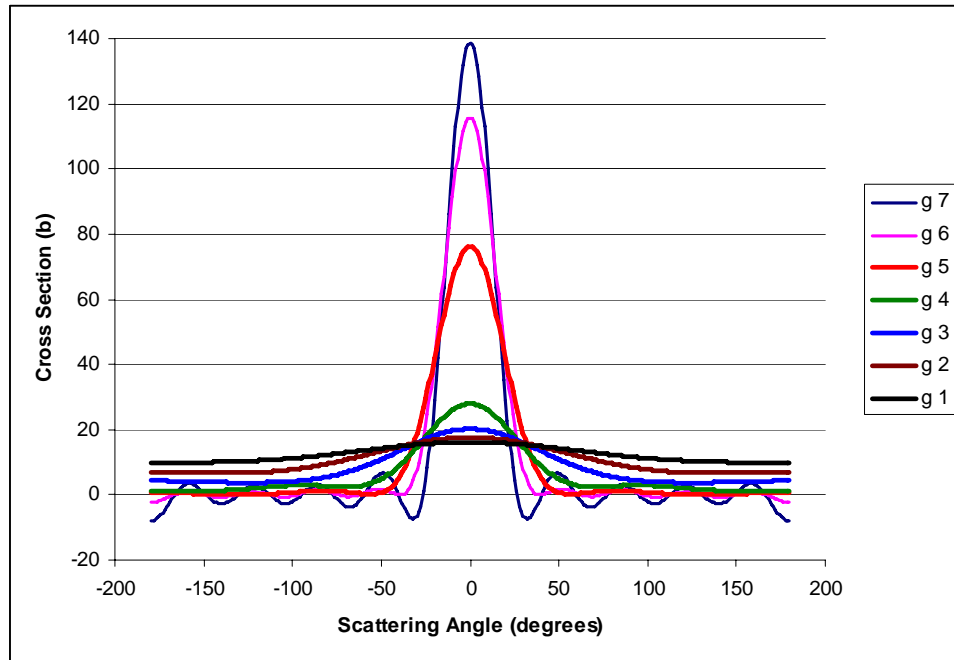


Figure 2.14: ^{238}U elastic scattering cross section as a function of energy and scattering angle for 7 groups.

Once again the three highest groups have a high likelihood of forward scattering. The scattering cross section values for ^{238}U are larger than those for ^{235}U . Figure 2.15 shows the elastic scattering cross section of neutrons incident upon Molybdenum atoms for a range of scattering angles in an assembly made of HEU.

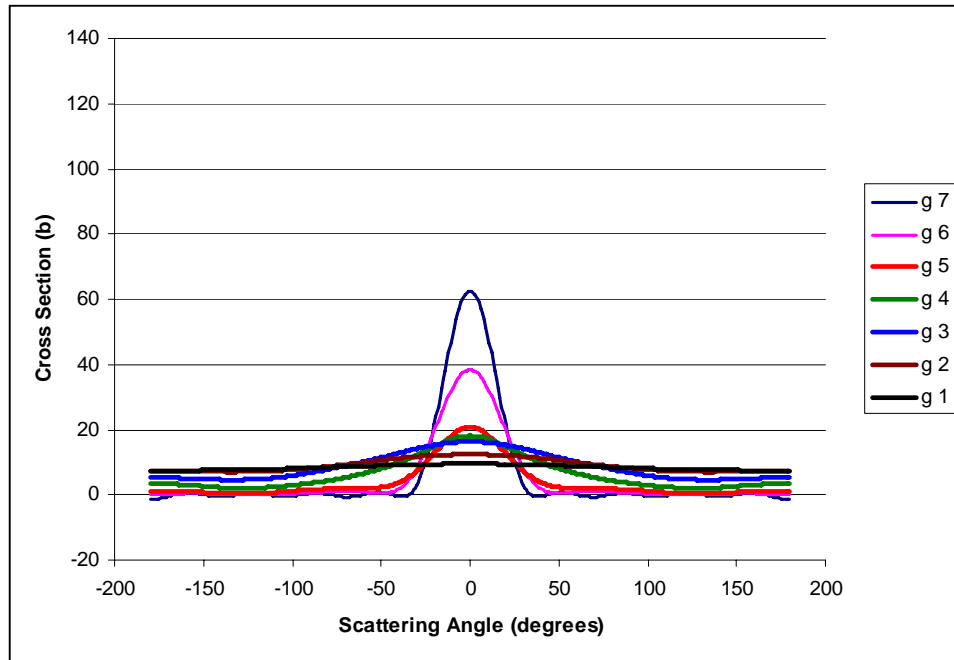


Figure 2.15: Mo elastic scattering cross section as a function of energy and scattering angle.

Scattering cross sections are similar for assemblies made of LEU; however, scattering is slightly less anisotropic because the flux weighted average energy in each group is slightly lower. The diffusion equation is most accurate when neutrons have no strong directional bias. Many scattering interactions are required before the initial source of 14 MeV neutrons traveling in a single direction becomes a completely isotropic cloud of neutrons.

Fortunately, the small size of the ZEDNA assemblies causes many of the source neutrons that are not absorbed to scatter only once before leaking out of the assembly. The large leakage probabilities negate the need to track several scattering events because many neutrons at very high energies are absorbed or leak before they scatter enough to

become isotropic. However, the large leakage probability must be accounted for to avoid significantly over predicting flux values in the assembly. Equation 2-27 describes the external source term calculation.

$$S_{i,j,g}^{\frac{x_1}{\partial t v_7}} = \frac{I_{0,i,j}}{(x_2 - x_1)\Sigma_{t,1}} \left(e^{-\Sigma_{t,1}x_1} - e^{-\Sigma_{t,1}x_2} \right) \times \left[(1 - \ell_i)(1 - \ell_o)(1 - \ell_t)(1 - \ell_b)\Sigma_{s,7 \rightarrow g} + \Sigma_{f,7}v_7\chi_{7,g} \right] \quad (2-27)$$

Where,

- ℓ_i is the leakage probability at the inner radius for cell (i, j) (-)
- ℓ_o is the leakage probability at the outer radius for cell (i, j) (-)
- ℓ_t is the leakage probability along the top edge for cell (i, j) (-)
- ℓ_b is the leakage probability along the bottom edge for cell (i, j) (-)
- $I_{0,i,j}$ is the source strength as it enters the assembly at cell (i, j) (n)
- x_1 is the distance traveled by the source through the reactor as it enters cell (i, j) (cm)
- x_2 is the distance traveled by the source through the reactor as it exits cell (i, j) (cm)

The ZEDNA source neutrons all appear in the highest energy group. In the case of planar sources the $I_{0,i,j}$ term does not depend on the axial location. For planar sources the initial source strength is only dependent on the fraction of the surface area at the top

of the assembly occupied by the column of cells at radius r_i . Initial source strength for planar sources is found using Equation 2-28.

$$I_{0,i,j} = n \frac{\left(r_i + \frac{dr}{2}\right)^2 + \left(r_i - \frac{dr}{2}\right)^2}{r_{outer}^2 - r_{inner}^2} \quad (2-28)$$

Here n is the total number of neutrons impinging on the assembly. Since the planar source begins at the top of the assembly and the direction of the planar source neutrons is normal to the top of the assembly, source penetration depths x_1 and x_2 are found by subtracting the height of the top and bottom surfaces of each cell from the total assembly height. Calculation of the $I_{0,i,j}$, x_1 , and x_2 terms are more difficult for simulations involving point sources because, in these cases, neutrons enter the assembly at many different angles, and locations along the inner radius and top surface. Figure 2.16 shows some of the different paths neutrons may travel to arrive at a given cell.

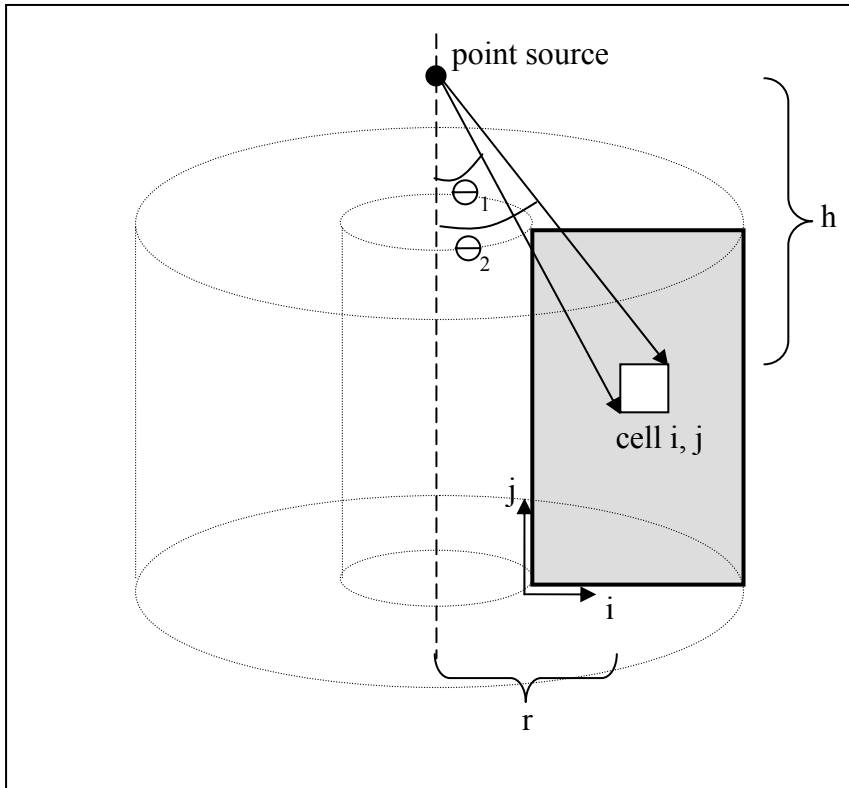


Figure 2.16: Point source illustration.

The angles θ_1 and θ_2 are the minimum and maximum angles with respect to the center line that neutrons striking the cell will have. For each cell, PRS calculated 20 evenly spaced angles between θ_1 and θ_2 . Then found the entrance and exit distances for each angle, and used the average entrance and exit distances for the x_1 and x_2 values shown in Equation 2-20.

The number of neutrons that strike a cell is dependant on the distance from the source and the angle made by the cells inside and top walls with respect to the source. Two view factor calculations were made to find the number of neutrons striking the top

and inside walls of each cell. Equation 2-29, shown below, finds the $I_{0,i,j}$ term for point sources (Feingold, 1970; Naraghi, 1982).

$$\begin{aligned}
 vf_{top} &= \frac{1}{2} \left[\left(1 - \frac{1}{\left(1 + \frac{\left(r_i + \frac{\Delta x}{2} \right)^2}{h_j^2} \right)^{\frac{1}{2}}} \right) - \left(1 - \frac{1}{\left(1 + \frac{\left(r_i - \frac{\Delta x}{2} \right)^2}{h_j^2} \right)^{\frac{1}{2}}} \right) \right] \\
 vf_{side} &= \frac{1}{2} \left[\frac{1}{\left(1 + \frac{r_i^2}{\left(h_j + \frac{\Delta y}{2} \right)^2} \right)^{\frac{1}{2}}} - \frac{1}{\left(1 + \frac{r_i^2}{\left(h_j - \frac{\Delta y}{2} \right)^2} \right)^{\frac{1}{2}}} \right] \\
 I_{0,i,j} &= n(vf_{top} + vf_{side})
 \end{aligned} \tag{2-29}$$

Where n is the total number of neutrons emitted by the point source in all directions. Some of the source strength values found using Equations 2-28 and 2-29 near the edges of the assembly were modified by the leakage terms. Leakage terms were necessary to account for neutrons that would escape the assembly after their first

scattering collision due to highly anisotropic motion that is not modeled well by the diffusion equation.

The goal of the leakage probabilities is to remove neutrons near the edge of the assembly that are moving toward the nearest edge. These neutrons are not likely to experience enough scattering collisions to exhibit isotropic behavior before leaking out of the system. The source term removes these neutrons because the diffusion equation is ill suited to handle their highly anisotropic behavior. Without the aid of leakage probabilities the diffusion equation will predict a grossly insufficient amount of neutron leakage after the first scattering event.

The group averaged transport mean free path and scattering angle were used to create two scattering vectors for source neutrons, of each energy group, in each cell, to determine which neutrons were lost to leakage. Figure 2.17 shows the four different leakage scenarios encountered in the simulations with point sources.

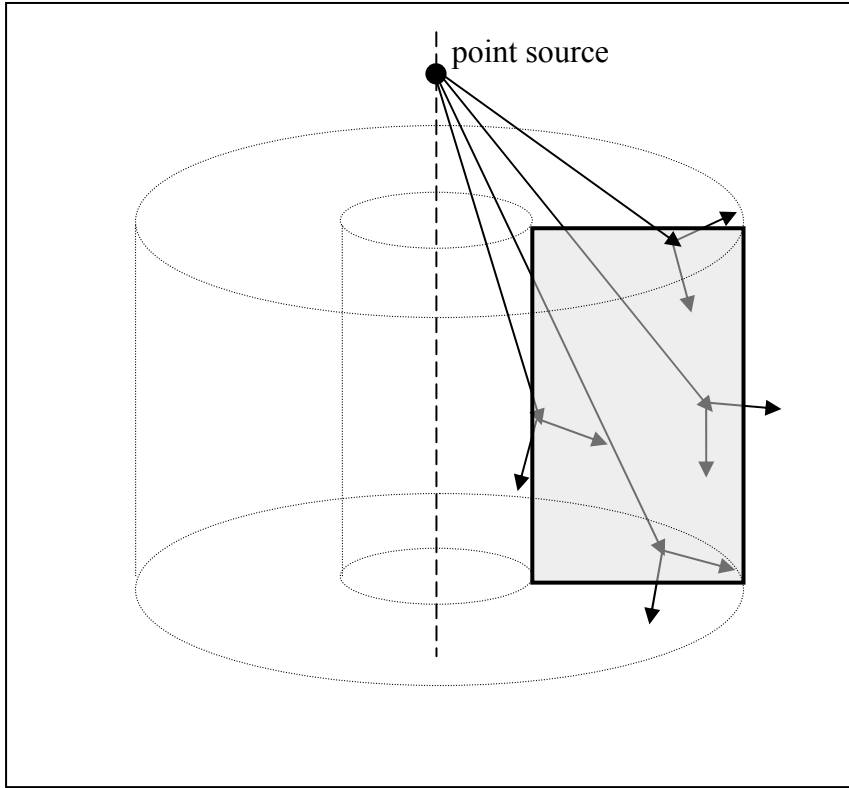


Figure 2.17: Point source leakage scenarios.

If the end point of either of the scattering vectors in the four scenarios is outside of the assembly, a leakage probability greater than zero is assigned to the scattered neutrons in the source term for a given energy and cell. If the end point of the scattering vectors for the inside or top edges are outside of the assembly the ℓ_i or ℓ_t leakage probability is set equal to 0.5. If the end point of the scattering vectors for the outside or bottom edges are outside of the assembly the ℓ_o or ℓ_b leakage probability is set equal to 1. For the planar source ℓ_i is always zero due to the high likelihood of forward scattering, and ℓ_i and ℓ_o are 0.5 if the endpoint of either scattering vector is outside of the assembly. ℓ_b is set equal to 1 if the endpoint of the scattering vector is outside of the assembly.

A volume source is also available for SPR pulse simulations. Unlike ZEDNA assemblies, SPR assemblies begin in a super prompt-critical condition. This affects the shape of SPR pulses, which begin at very low powers and ramp up gradually. The ramp up reduces the need for a complex external neutron source. Regardless of the initial source, the flux in the assembly quickly takes the shape of the fundamental harmonic. PRS finds the average flux in the assembly for a given power and places a uniform amount of flux throughout the reactor. The initial power selected by the user is used to find the required fission reaction rate per unit volume using Equation 2-30 (Lamarsh, 2001).

$$RR_{fiss} = \frac{P}{(2.88 \times 10^{-11})V} \quad (2-30)$$

Where P is power in Watts, V is the fuel volume, and 2.88×10^{-11} is the number of J produced per fission. The average flux throughout the assembly for all groups is then found using Equation 2-31 (Lamarsh, 2001).

$$\phi_{tot} = \frac{RR_{fiss}}{\Sigma_f} \quad (2-31)$$

Where Σ_f is the one group fission cross section for the entire neutron energy spectrum and ϕ_{tot} is the total flux in the assembly over all groups. Once the flux for all

energies is known the initial flux at each node and group group is found using Equation 2-32 (Lamarsh, 2001).

$$\phi_{i,j,g}^1 = \phi_{tot} \chi_g \quad (2-32)$$

Where the superscript on the source term denotes the simulation time step, the i is the radial position, j is the axial position, g is the group, and χ_g is the fraction of fission neutrons produced in group g.

2.3.4 Sample Cavity Fluence

The purpose of SPR and ZEDNA reactors is to irradiate samples placed in the cylindrical cavities at the center of the reactors. It is useful to be able to predict what fluence the samples experience. Fluence in the sample cavity is calculated using the neutron path length per unit volume method shown in Equation 2-33 below.

$$\begin{aligned} \phi &= n \nu \left(\frac{n}{cm^2 s} \right) \\ \Phi &= \int_0^t \phi dt \left(\frac{n}{cm^2} \right) \\ \Phi_g &= \frac{1}{vol} \sum_{t=1}^n \sum_{j=1}^J \sum_{i=1}^J 2\pi R \Delta y \Delta t J_{1,j,g}^{+,t} \langle |\tilde{r}| \rangle(i,j) \nu f(i,j) \left(\frac{n}{cm^2} \right) \end{aligned} \quad (2-33)$$

Where vol is the volume of the sample cavity. The exiting current J^+ is multiplied by the time step size and the surface area that the current passes through at each node to

find the quantity of neutrons that enter the sample cavity. The view factors predict what fraction of the current goes in each direction. Finally the neutron path lengths predict the distances the neutrons will travel in the cavities. Additional calculations must be carried out to find the view factors and neutron path lengths for neutrons exiting the top and bottom holes of the assembly. The view factor from a node at the inner radius to the hole at the top or bottom of the cavity is found using Equation 2-34, shown below (Leuenberger, 1956).

$$vf(hole, j) = \frac{1}{4} \left\{ \left(1 + \frac{h_j}{\Delta y} \right) \left[4 + \left(\frac{\Delta y}{r} + \frac{h_j}{r} \right)^2 \right]^{\frac{1}{2}} - \left(\frac{\Delta y}{r} + \frac{2h_j}{r} \right) - \frac{h_j}{\Delta y} \left(4 + \left(\frac{h_j}{r} \right)^2 \right)^{\frac{1}{2}} \right\} \quad (2-34)$$

Where h_j is the vertical distance from the nearest edge of the cell (1, j) to the hole, r is the inner radius of the assembly, and Δy is the height of the cell. The path length of neutrons escaping the top and bottom holes was found in a manner similar to the ring to ring path lengths. If neutrons are emitted isotropically from the inner radius, they are more likely to escape from portions of the hole that are closer to the node of origin. Figure 2.18 illustrates the path length of neutrons escaping the holes at the top and bottom of the sample cavity.

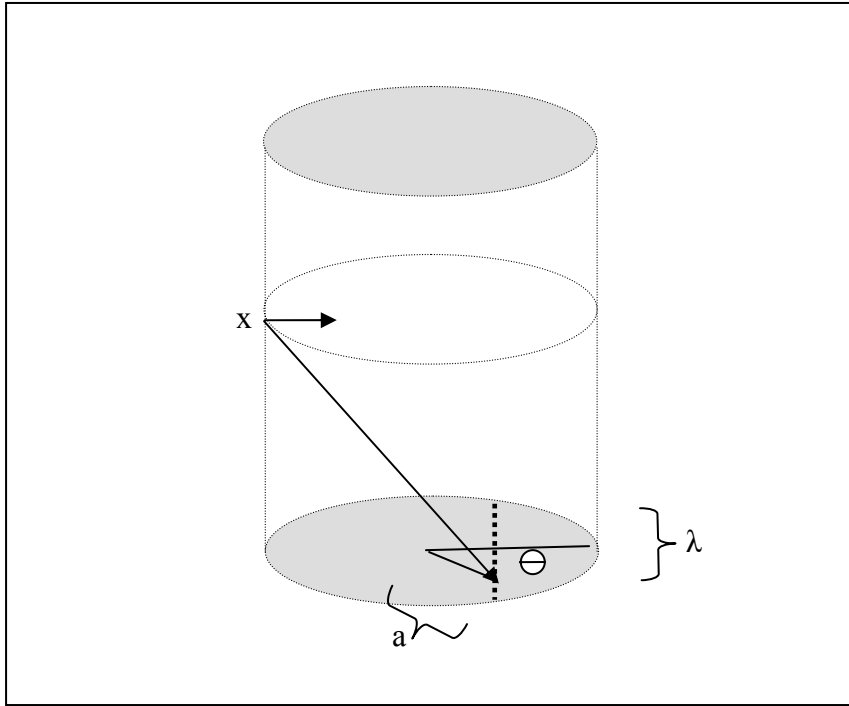


Figure 2.18: Illustration of the ring to hole neutron path length calculation.

The neutron path lengths of neutrons exiting the top and bottom holes in the cavity are found using Equation 2-35.

$$\langle |\tilde{r}| \rangle = \frac{\int_0^{2\pi R} \int_0^{\frac{\pi}{2}} |\tilde{r}| \lambda \cos\left(\frac{x}{2R} \frac{\pi}{2}\right) \partial a \partial \theta}{\int_0^{2\pi R} \int_0^{\frac{\pi}{2}} \lambda \cos\left(\frac{x}{2R} \frac{\pi}{2}\right) \partial a \partial \theta}$$

$$x = a(1 + \cos \theta)$$

$$\lambda = 2\sqrt{x(2R - x)}$$
(2-35)

Where x is the distance in the direction shown in Figure 2.11. λ is the chord length of the circle at the distance x . The chord lengths are weighted to increase in size

with smaller x values. Path length weighting by chord length is necessary due to the skewed perspective of the hole experienced by neutrons exiting from each node. From the perspective of the exiting neutron the hole is skewed to look pear-shaped instead of being perfectly circular. The skewed perspective is the result of a much larger solid angle between the neutron exit location and portions of the hole it is nearest to. In other words, an isotropic source of neutrons leaving a point on the cavity surface will give rise to a spatially non-uniform current density crossing outward from the top and bottom of the cavity.

Once the neutronics module produces the correct neutron flux values for a given time step, the heat transfer module must predict the resultant temperature rise.

2.4 HEAT TRANSFER EQUATIONS

The heat transfer module may account for conduction heat transfer and fission heating. The user may also only simulate fission heating while neglecting conduction heat transfer in the interest of maximizing computational efficiency. If an initial scoping simulation that accounts for conduction with a grossly overestimated thermal conductivity value does not produce different temperature profile data than a similar simulation that neglects conduction, it would be prudent to avoid the superfluous conduction heat transfer calculations. PRS will allow the user the option of accounting for conduction heat transfer to increase its versatility. Regardless of whether or not the user chooses to account for conduction, an assumption of adiabatic heating is made for all simulations.

Adiabatic heating means that all heat transfer out of the assembly is negligible. This assumption is valid because the amount of heat deposited into the system is several orders of magnitude larger than the amount of heat lost to the surroundings during the simulations. Rough estimates of the rate of heat loss by conduction and convection will be made to justify the adiabatic heating assumption. Equation 2-36 describes heat loss due to radiative heat transfer (Incropera, 2002; Mills, 1999).

$$q_{rad} = A_1 v f_{1,2} \varepsilon \sigma (T_1^4 - T_2^4) \text{ (Watts)} \quad (2-36)$$

Where A_1 is the surface area of the object emitting heat, $v f_{1,2}$ is the view factor between the objects emitting and receiving heat, ε is the emissivity of the object, σ is the Stefan-Boltzmann constant with the value of $5.670 \times 10^{-8} \text{ (W m}^{-2} \text{ K}^{-4}\text{)}$, T_1 is the temperature at the surface, and T_2 is the temperature of the surroundings. Circumstances that make radiative heat transfer as large as possible will be used for this calculation to ensure that its effects are not underestimated. An emissivity of 1 will be used in the calculation because that is the largest value possible for any object. A view factor of 1 will be used to assume that all radiation emitted will be absorbed by the surroundings. A cylinder with an outer radius of 30 cm, and a height of 40 cm, is used for the area calculations. Temperatures of 1000 K and 300 K were used for the surface and surroundings respectively. Using the values listed above the rate of heat loss due to radiative heat transfer is 6.4 kW. Equation 2-37 describes heat loss due to convection heat transfer (Incropera, 2002; Mills, 1999).

$$q_{conv} = A_1 h (T_1 - T_2) \text{ (Watts)} \quad (2-37)$$

Where h is the convection heat transfer coefficient. The same area and temperature values were used in the convection and radiative heat transfer calculation to avoid under-predicting heat losses. Typical heat transfer coefficients for free convection of gasses range from 2 to 25 $\text{W m}^{-2} \text{K}^{-1}$ (Incropera, 2002). A heat transfer coefficient of 25 $\text{W m}^{-2} \text{K}^{-1}$ was used for this calculation. The rate of heat loss due to convection heat transfer for the scenario described above is 2.0 kW.

For the scenario most favorable for heat loss to the surroundings the combined rate of energy loss to the surroundings due to radiative and convection heat transfer is 8.4 kW. The rate of energy put into the system due to fission for a nominal pulse can be found by dividing the total energy put into the system by the time required for a pulse. A 10 MJ pulse could be expected to last roughly 100 μs , this type of pulse yields an average power of 10^8 kW. Since the rate of heat gain during a pulse is 7 orders of magnitude large than the rate of heat loss, for the scenario in which heat loss is most likely, the effects of heat loss can be assumed to be negligible. Now that the PRS assumption of adiabatic heating has been proven to be sound, the method of simulating fission heating and conduction heat transfer will be examined.

The temperature profile will closely match the neutron flux profile until the effects of conduction heat transfer become significant. Conduction heat transfer is only non-negligible in simulations with very long pulses and large thermal conductivity

coefficients. Users will have the option to remove the effect of conduction from the simulation and speed up the calculation, should they decide that conduction heat transfer is negligible. Equation 2-38 is used to determine the amount of heat per unit volume produced within a given cell from all neutron energies after a single neutronics module time step.

$$\dot{Q}_{fiss}''' = dt \cdot 180 \left(\frac{MeV}{fiss} \right) \cdot 1.602177e-13 \left(\frac{J}{MeV} \right) \sum_{g=1}^G \phi_g \Sigma_{fiss,g} \quad (2-38)$$

Where all the constants above have been defined in the previous sections. Each fission releases 180 MeV of energy immediately into the assembly in the form of fission fragments, neutrons, and gamma rays. Roughly 20 more MeV of energy are eventually deposited into the assembly by fission product decay. However, fission product decay energy may take several seconds or minutes to appear in the system. As a result of the slow nature of fission product decay energy deposition, only 180 MeV is deposited into the assembly for each fission in the simulations.

When the effects of conduction are neglected, the change in temperature for a cell is equal to the total fission energy deposited into the cell for the duration of the pulse divided by the cells mass and the specific heat of the material. If the effects of conduction are not neglected the heat diffusion equation, Equation 2-39, is used to determine the spatially and temporally dependant temperature values within the simulation (Incropera, 2002; Mills, 1999).

$$\rho c_p \frac{\partial T}{\partial t} = \dot{Q}_{fiss}''' + k \left(\frac{1}{r} \frac{\partial T}{\partial r} + \frac{\partial^2 T}{\partial r^2} + \frac{\partial^2 T}{\partial z^2} \right) \quad (2-39)$$

Where,

- T is temperature of the assembly (K)
- \dot{Q}_{fiss} is the fission power deposited into the cell for the time step (W cm^{-3})
- RR_{fiss} is the fission reaction rate at the time step ($\text{reactions cm}^{-3} \text{ s}^{-1}$)
- c_p is the specific heat of the assembly material ($\text{J g}^{-1} \text{ K}^{-1}$)
- k is the thermal conductivity of the assembly ($\text{W cm}^{-1} \text{ K}^{-1}$)
- ρ is density of the assembly material (g cm^{-3})

Since there is no heat transfer in or out at the boundaries, the spatial derivative with respect to temperature is zero at the boundaries. Once neutron transport and temperature rise data has been calculated for a given time step, PRS simulates the subsequent thermal expansion present in a reactor pulses.

2.5 MECHANICS EQUATIONS

SPR reactors and ZEDNA designs have all been constructed in a similar fashion. Several thin fuel plates with holes in the center are stacked on top of each other and bolted together. Axial expansion of the fuel plates is much larger near the inner radius of the assembly where the fission density is highest. In order to reduce axial stresses and

negate axial wave propagation, contact between successive fuel rings is limited to areas near the outer radius. Figure 2.19 shows a cutaway view of the SPR III reactor.

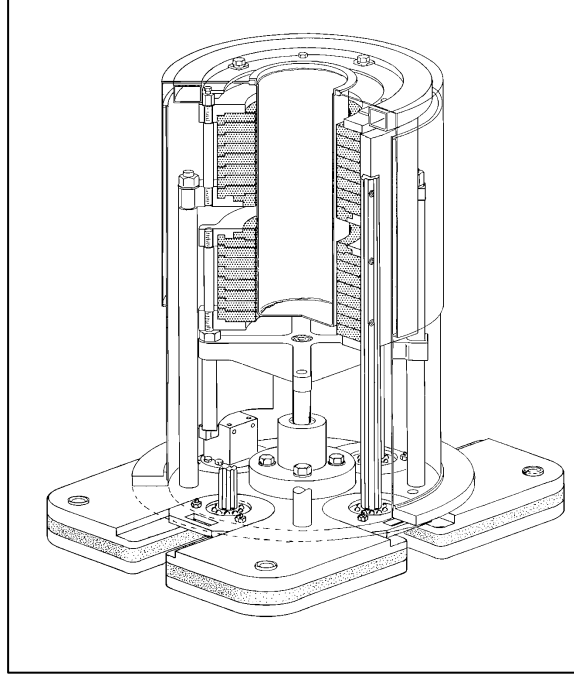


Figure 2.19: Cutaway view of the SPR III reactor.

Equation 2-40 governs the dynamic thermoelastic behavior of a linear isotropic material for a cylindrical coordinate system with angular symmetry (Reuscher, 1971; Kausel, 2006).

$$\frac{\partial^2 u}{\partial r^2} + \frac{1}{r} \frac{\partial u}{\partial r} - \frac{u}{r^2} - \frac{1+\nu}{1-\nu} \alpha \frac{\partial T}{\partial r} = \frac{1}{c^2} \frac{\partial^2 u}{\partial t^2} \quad (2-40)$$

$$c^2 = \frac{E(1-\nu)}{(1+\nu)(1-2\nu)\rho}$$

Where

- u is the change in radial position of each node (cm)
- r is the radial position in the assembly (cm)
- ν is Poisson's ratio for the assembly material
- α is the thermal expansion coefficient (K^{-1})
- T is the change in temperature of the assembly as compared to the assembly temperature at the beginning of the pulse (K)
- c^2 is the maximum wave propagation speed in the assembly squared ($cm^2 s^{-2}$)
- E is the modulus of elasticity for the assembly material ($kg s^{-2} cm^{-1}$)

The primary assumption made in the application of Equation 2-40 to SPR and ZEDNA reactors is that shear and axial stresses at the top and bottom surfaces of each fuel plate are negligible. These assumptions are not entirely valid due to surface friction between plates and axial expansion of fuel plates in areas where successive rings are in contact. However, these assumptions have been made by others in the past to analyze SPR reactor pulses and they will allow for high enough fidelity in the predictions made by the mechanics module to simulate reactor pulse behavior (Wimmet 1992). The inner and outer surfaces of the assembly are free to expand and contract without striking any other surfaces. The free movement of the boundaries causes radial stress to vanish at the inner and outer radii. Radial stress can be found using Equation 2-41 (Reuscher, 1971).

$$\sigma_r(r, z, t) = (2\mu + \lambda) \frac{\partial u}{\partial r} + \frac{\lambda u}{r} - (3\lambda + 2\mu) \alpha T(r, z, t)$$

$$\lambda = \frac{\nu E}{(1 + \nu)(1 - 2\nu)} \quad (2-41)$$

$$\mu = \frac{E}{2(1 + \nu)}$$

Equation 2-41 is manipulated to form the appropriate boundary conditions at the inner and outer radii. Radial displacement causes stress in the axial, radial, and tangential directions. Equation 2-42 was used to calculate stress in the radial and tangential directions (Reuscher, 1971).

$$\sigma_z(r, z, t) = \lambda \frac{\partial u}{\partial r} + \frac{\lambda u}{r} - (3\lambda + 2\mu) \alpha T(r, z, t)$$

$$\sigma_\theta(r, z, t) = \lambda \frac{\partial u}{\partial r} + (2\mu + \lambda) \frac{u}{r} - (3\lambda + 2\mu) \alpha T(r, z, t) \quad (2-42)$$

The Von Mises Criterion for failure of ductile materials, also known as the distortional energy criterion, states that yielding occurs when the Mises stress exceeds the yield stress. Equation 2-43 was used to find the Mises stress (Bedford, 2000, 2002).

$$\sigma_M = \frac{1}{\sqrt{2}} \sqrt{(\sigma_r - \sigma_z)^2 + (\sigma_z - \sigma_\theta)^2 + (\sigma_\theta - \sigma_r)^2} \quad (2-43)$$

PRS calculates the Mises stress induced at each point in the assembly at each time step. The user can compare the maximum Mises stress to the dynamic yield stress at the

appropriate temperature to determine if the material will deform plastically or crack during a pulse.

Since the methodology used within each module has been examined, the results of benchmark comparisons made to check the veracity of data produced in each module may now be presented. The benchmark comparison results will be presented following the order that the solution methodologies were introduced. The neutronics benchmarking with MCNP is first, followed by the mechanics and heat transfer modules comparisons with COMSOL.

Chapter 3: Neutronics Benchmarking

The neutronics module was isolated and compared to MCNP in two different scenarios to test the validity of the modules external neutron source term, inner radius boundary condition, fluence calculation, and criticality predictions.

The first test scenario will test each of the original contributions to the field of deterministic neutron transport modeling made during the creation of PRS. Both codes will model a reactor of a given criticality during sub prompt critical pulses. Results from planar and point neutron source simulations will be shown. The codes will predict the axial and radial neutron flux profiles during the first 10 neutron lifetimes to determine how well the external source term and boundary conditions simulate the spatial and temporal propagation of the neutrons. The codes will also produce total fluence and neutron energy spectrum data for the sample cavity to determine the merit of the fluence calculation method. The value of the original contributions may be judged by how closely results from MCNP and PRS agree in the first test scenario.

The second test scenario will compare PRS and MCNP criticality predictions. The criticality of reactors made of HEU and LEU will be calculated using MCNP and then compared to PRS criticality calculations with a range of neutron energy groups. Discrepancies in criticality predictions between MCNP and PRS will be removed before pulse simulations through the adjustment of reactor dimensions. PRS may be run in

criticality calculation mode as dimensions are varied until the correct criticality is produced.

If reactor dimension adjustments are small enough, they will not significantly influence mechanics module data and pulse simulation results will not suffer. Comparisons with experimental SPR data will allow one to determine if adjustments in reactor dimensions are too large. If the PRS simulation reactor dimensions do not match the experimental dimensions closely enough more energy groups can be added to the simulation to improve the criticality prediction.

In order to achieve numerical stability the maximum grid spacing and time step values were dictated by the minimum diffusion length and neutron lifetime values. The neutron lifetime for a given group is found using Equation 3-1, shown below (Hetrick, 1971; Stacey, 2001).

$$\Lambda_g = \frac{1}{\nu_g \Sigma_{fg}} \quad (3-1)$$

$$l_g = \Lambda_g k_{eff}$$

Where Λ_g is the neutron generation time. k_{eff} was found by taking the ratio of total neutron populations after a one average neutron lifetime. The number of time steps taken between k_{eff} values was found by dividing the average neutron lifetime by the time step size. The average neutron lifetime is found by taking a neutron density weighted average of the neutron lifetimes of each group. The k_{eff} values from both PRS and MCNP represent the ratio of prompt neutron populations only. Delayed neutron

populations, produced by fission product decay, are negligible in the time frames during which reactor pulses occur.

3.1 FIRST TEST SCENARIO

The first scenario used for comparison included an HEU assembly with inner and outer radii of 10 and 16 cm respectively. The assembly had a height of 30 cm. An external source of 14 MeV neutrons in the form of either a point or a planar source acted on the assembly. This scenario confirms that the source term is properly depositing the neutrons into the assembly, and that the boundary conditions are predicting the correct radial and axial flux profile shapes. The fluence values within the sample cavity are also compared at several times.

The planar external neutron source consists of 10^{15} neutrons at 14 MeV, beginning at the top of the assembly, moving downward, evenly distributed between the inner and outer radius as shown in Figure 3.1.

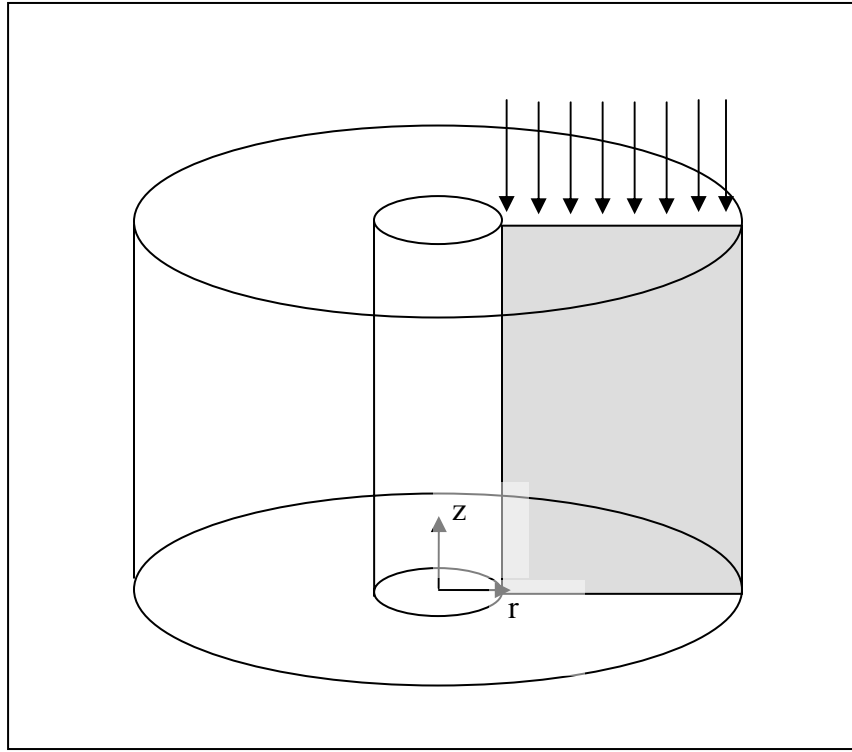


Figure 3.1: Direction of external source neutrons relative to the area simulated.

For the point source, 10^{15} neutrons at 14 MeV are emitted isotropically at the centerline at a height of 5 cm above the assembly. Only a fraction of the point source neutrons emitted strike the assembly. The MCNP and PRS simulations are compared at time intervals ranging from 1 to 10 neutron lifetimes. The average neutron lifetime in the simulations with assemblies made of HEU is 7.129 shakes. One shake is equivalent to 10 ns.

The k_{eff} value of the assembly in MCNP was 0.98069. The outer radius dimension was modified by adding 2.2 millimeters in the PRS simulation in order to produce the same k_{eff} value as seen the MCNP simulation. The outer radius of the PRS simulation was modified because it was important to remove the influence of criticality

errors on external source benchmarking. Gaps between fuel plates were not accounted for in the fuel density calculation. The fuel is treated as a solid block of uranium and molybdenum at a nominal density. Only the results from trials with 7 neutron energy groups are shown here. Figure 3.2 shows how the average flux in the assembly, with the planar neutron source, changes over time.

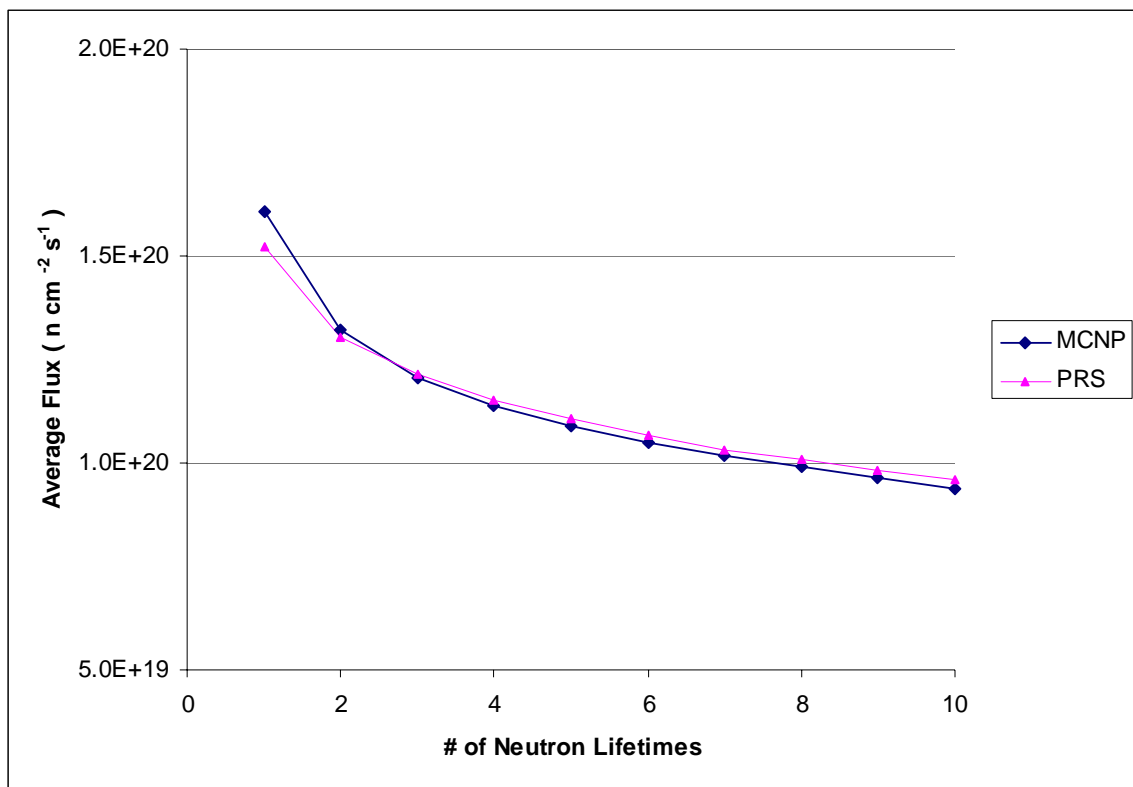


Figure 3.2: Average flux with the planar neutron source.

The largest difference between the PRS and MCNP simulations occurs at the first data point. There is a five percent difference in the total flux value predicted after one neutron lifetime by PRS and MCNP. The following total flux values differ by less than

five percent. The sharp drop in flux values seen between 1 and 3 neutron lifetimes may be attributed to the flight time of neutrons crossing the sample cavity. In the first several neutron lifetimes there is little inward current at the inner radius because it takes several time steps for the lower energy neutrons to travel most of the flight paths.

The initial treatment of the inward current calculation is a source of error in the total flux values. When the source neutrons scatter into the sample cavity immediately after entering the assembly they are still more likely to be headed downward than upward. Since the inward current calculation assumes that the neutrons entering the sample cavity have no angular bias, it will not calculate the flight path and likelihood of re-entry of the initial sample cavity neutrons correctly. Figure 3.3 shows how the average flux in the assembly with the point neutron source changes over time.

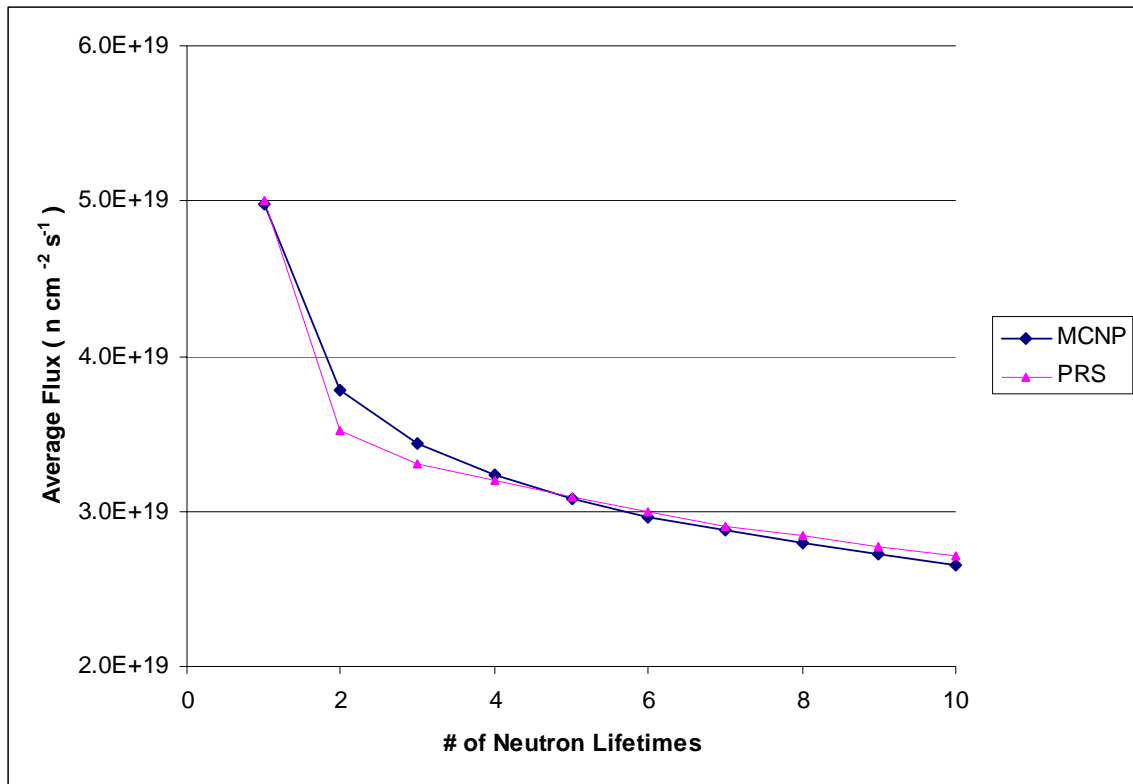


Figure 3.3: Average flux with the point neutron source.

The average neutron lifetime of the assembly lasts 14 neutron time steps and the external point source neutrons are deposited into the assembly over the first 10 time steps. The inward current calculation is shut off while the point source propagates through the assembly to avoid over predicting the current re-entering the assembly. The point source neutrons do not contribute to the inward current because of their initial outward direction and high likelihood of forward scattering.

The PRS simulation predicts a total flux value 7 percent lower than the MCNP simulation after the second neutron lifetime. MCNP produces a smoother total flux curve than PRS due to the treatment of sample cavity neutrons. PRS must assign a single time

delay value to neutrons traveling from one node to another; while neutrons traversing the sample cavity in MCNP, leaving from and returning to areas equivalent to the nodes in PRS, have a wide range of flight paths.

The assignment of an average flight distance value causes the inward current to arrive after discrete amounts of time in PRS instead of being more spread out as it is in MCNP. If the flight paths in PRS are too long the drop in flux will be too sharp, as seen in the point source average flux plot. Flight paths that are too short will cause the average flux plot to be smoother than it should be, as seen in the planar source average flux plot. The method used to calculate the average distance between two rings, which represent nodes at the inner radius, is described near the end of section 2.2. Figure 3.4 shows the sample cavity fluence in the planar neutron source simulation over a range of energies after 10 μ s.

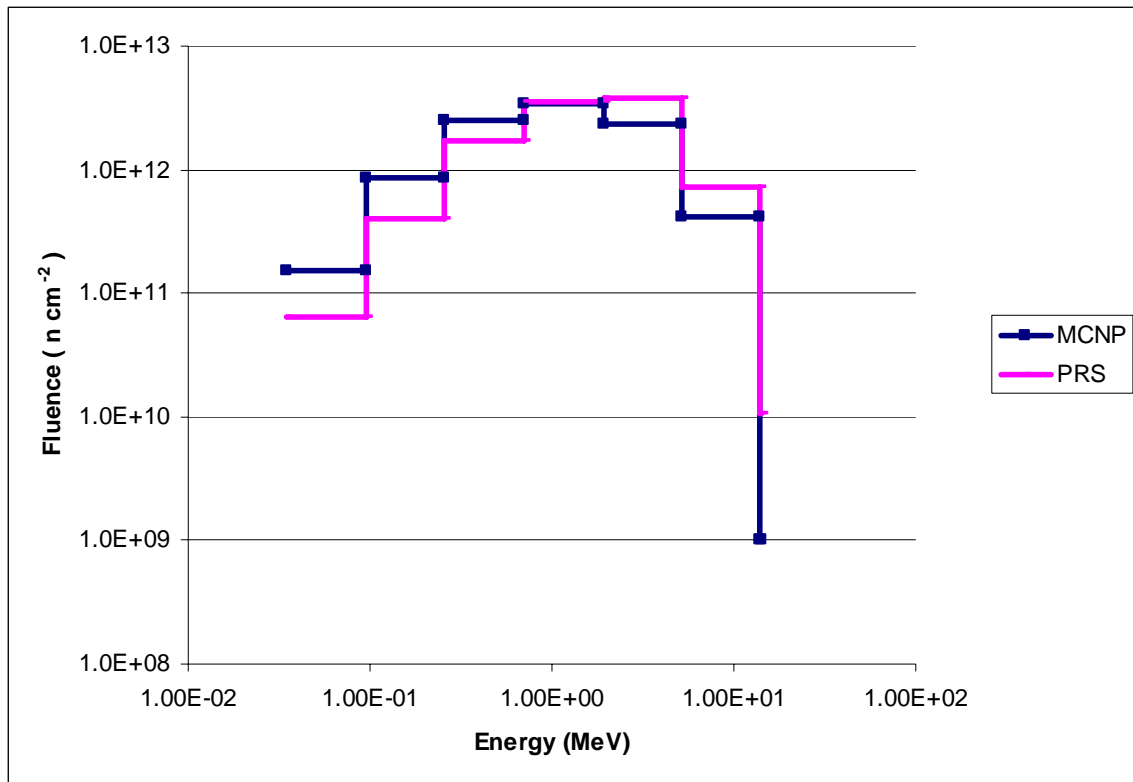


Figure 3.4: Cumulative sample cavity fluence after 10 μ s with the planar neutron source.

PRS produces a spectrum of fluence values that favors higher energies more than MCNP. However, both MCNP and PRS predict roughly the same amount of total fluence after 10 μ s. The planar source did not contribute directly to the cavity fluence because it began and ended at the inner and outer radii of the assembly in both simulations. Figure 3.5 shows the sample cavity fluence in the point neutron source simulation over a range of energies after 10 μ s.

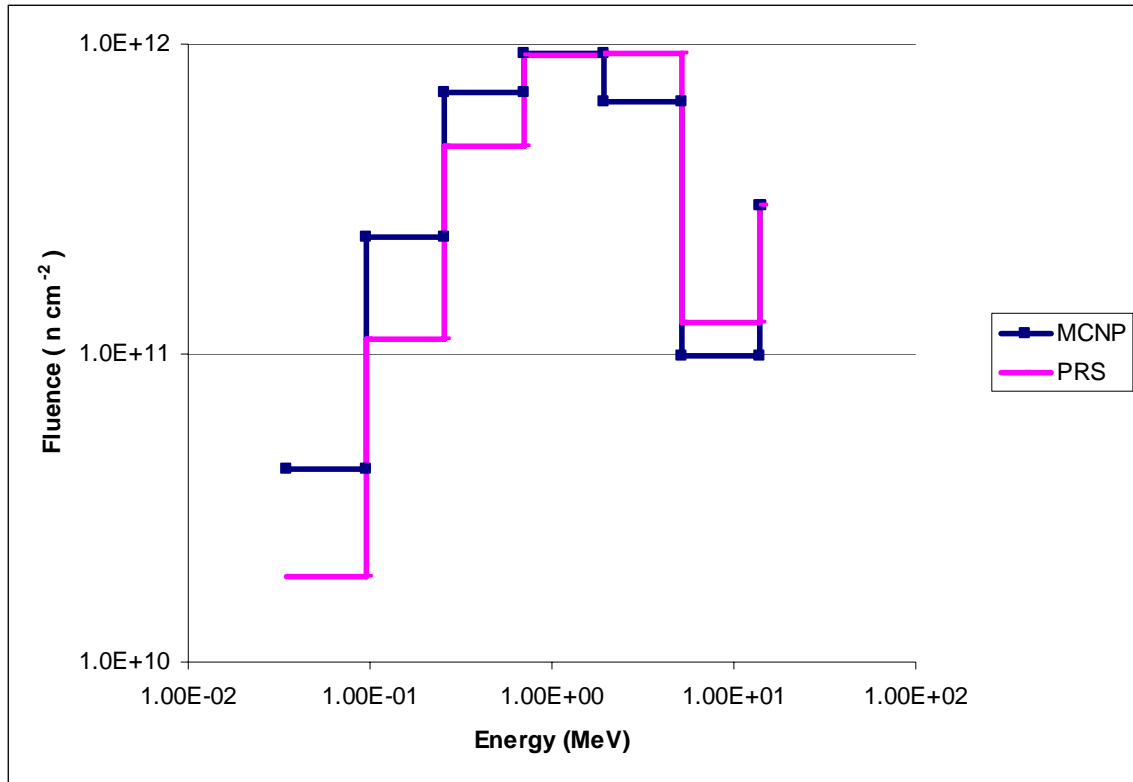


Figure 3.5: Cumulative sample cavity fluence after 10 μ s with the point neutron source.

The fluence at the highest energy group was caused by neutrons emitted directly from the point source. The fluence in the spectrum below the highest energy group is due to neutron source multiplication by the assembly. The PRS simulation has an overabundance of high energy neutron fluence due to the flawed simulation of down scattering caused by the coarse neutron group structure. Figure 3.6 shows the growth of the sample cavity fluence in the planar neutron source simulation from 1 to 10 shakes. 1 shake is equivalent to 10 ns.

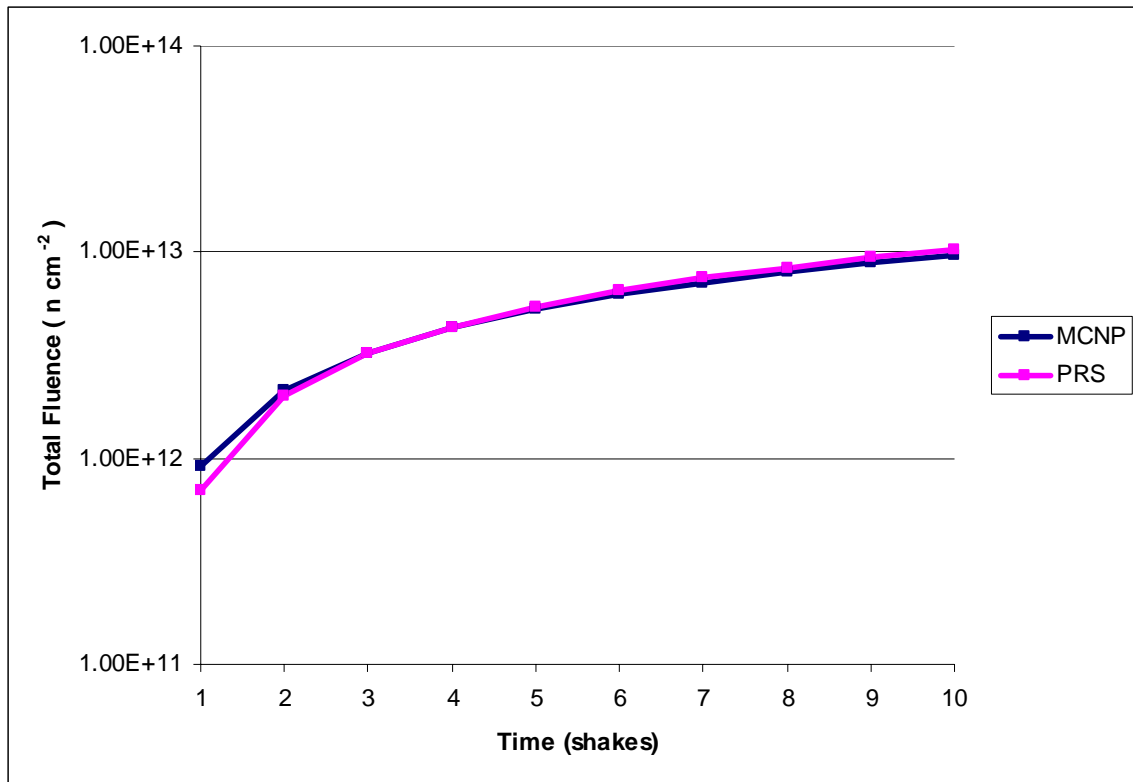


Figure 3.6: Sample cavity fluence over time with the planar neutron source.

The difference in fluence values at the first data point is caused by the method used to calculate fluence in PRS. MCNP adds to the total fluence value as the neutron traverses the sample cavity. Conversely, PRS only contributes a neutrons motion to the total fluence calculation after it has crossed the sample cavity. The fluence calculation was made by summing the product of all of the current escaping the sample cavity at a given time step multiplied by the path length the current traveled. Neutrons remaining in the cavity do not contribute to the total fluence until they escape.

It would have been much more cumbersome and computationally inefficient to calculate and add the fraction of the flight path traveled by the sample cavity neutrons at

the end of each time step. Differences in total fluence values beyond 10 shakes can be attributed to minor differences in the criticality of the two simulations. Figure 3.7 shows the growth of the sample cavity fluence in the point neutron source simulation from 1 to 10 shakes.

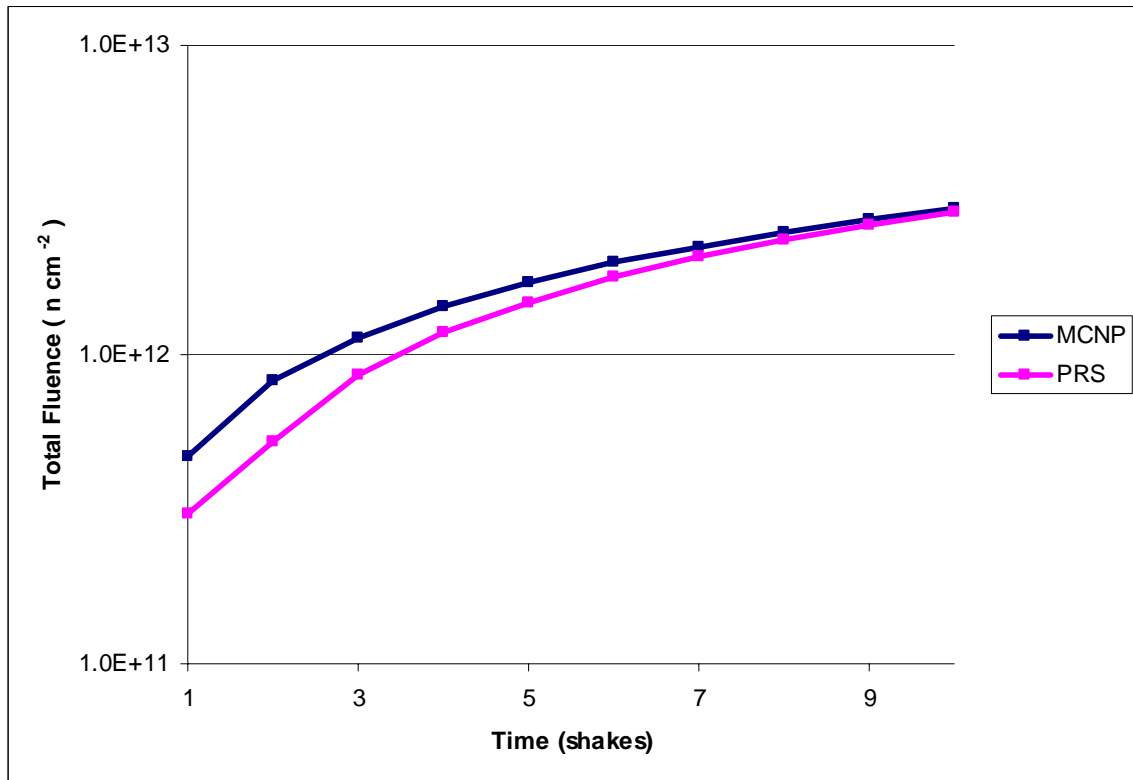


Figure 3.7: Sample cavity fluence over time with the point neutron source.

The PRS fluence at 1 shake differs from MCNP by 35% for the point source simulation, while the difference between MCNP and PRS was 24% at the first data point in the planar source simulation. The larger initial discrepancy between PRS and MCNP is due to the fact that PRS accounts for a neutrons motion through the cavity only after it

has escaped, as described above, and the delay before current re-enters at the inner radius is longer for point source simulations due to the initial outward direction of the source neutrons. The early fluence calculations from PRS will under predict fluence values because neutrons are not counted until they escape the sample cavity. However, the PRS and MCNP simulations converge eventually because PRS correctly accounts for all of the neutrons. Figure 3.8 shows the radial flux profile of the assembly at several points in time for the planar source simulations.

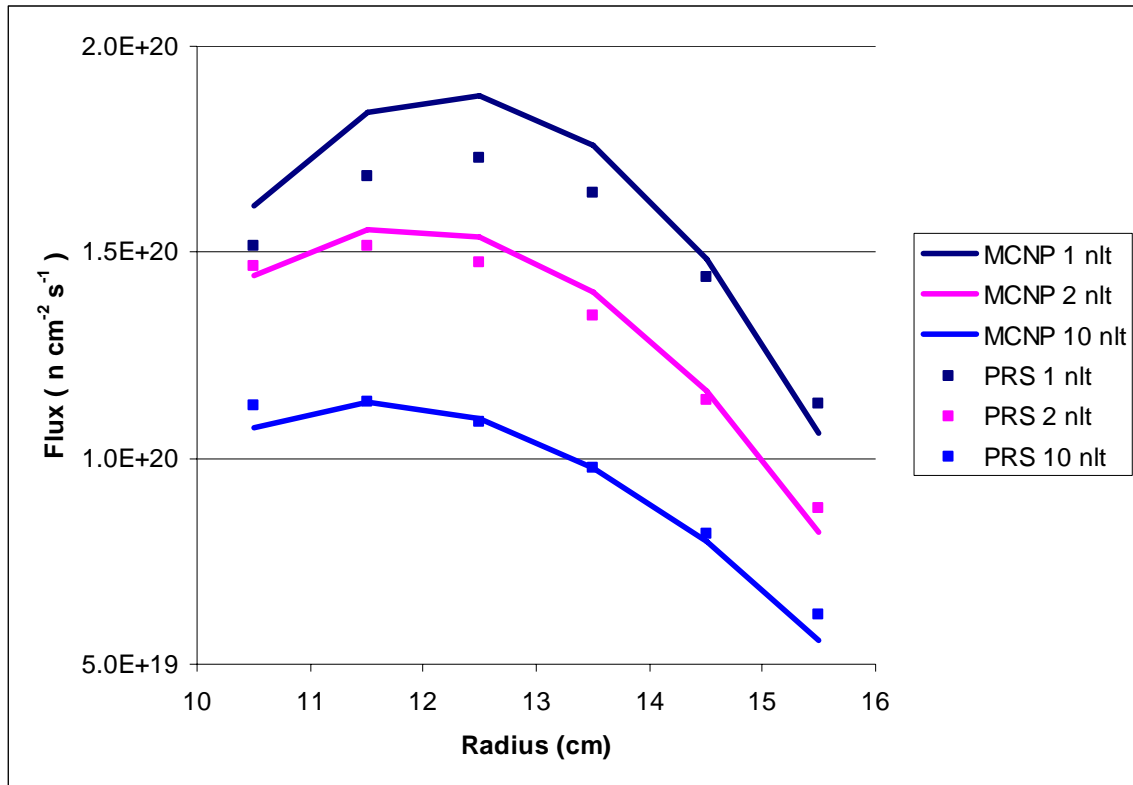


Figure 3.8: Radial flux profile at several times for the planar neutron source.

The disagreement between PRS and MCNP after the first neutron lifetime is due to the different methods used to handle the external source neutrons. The MCNP flux tally includes uncollided 14 MeV source neutrons that have not yet passed through the assembly. The PRS simulation uses the source term to replace the uncollided 14 MeV neutrons with the scattered source neutrons and neutrons caused by fission of the source neutrons. The removal of the uncollided 14 MeV neutrons does not affect the other modules because all source term fission reactions are tallied and added to the subsequent heating calculations. After 10 neutron lifetimes the shape of the radial flux profiles shows close agreement. Agreement in the radial flux profile shapes confirms that the inner radius boundary condition is predicting the correct amount of re-entrant current. Figure 3.9 shows the axial flux profile of the assembly at several points in time for the planar source simulations.

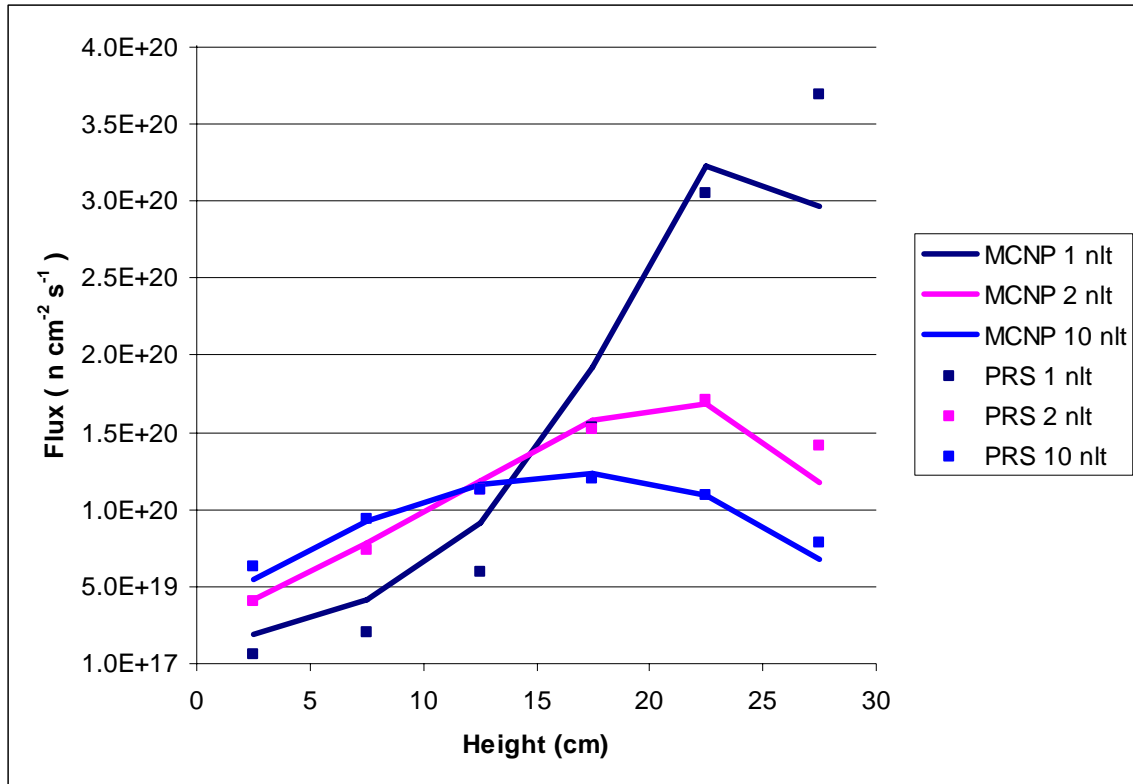


Figure 3.9: Axial flux profile at several times for the planar neutron source.

After one neutron lifetime, the axial flux profile produced PRS favors the top of the assembly more than the axial flux profile produced by MCNP. The PRS external source term deposits the source neutrons into the assembly after their first interaction with the assembly. PRS treats the once scattered neutrons as though they have no directional bias and allows them to slowly diffuse into the assembly. MCNP shows that the once scattered neutrons still behave anisotropically because neutrons at the top of the assembly move downward more quickly than in the PRS simulation. However, after 10 neutron lifetimes MCNP and PRS produce axial flux profiles that are very similar.

Figure 3.10 shows the radial flux profile of the assembly at several points in time for the point source simulations.

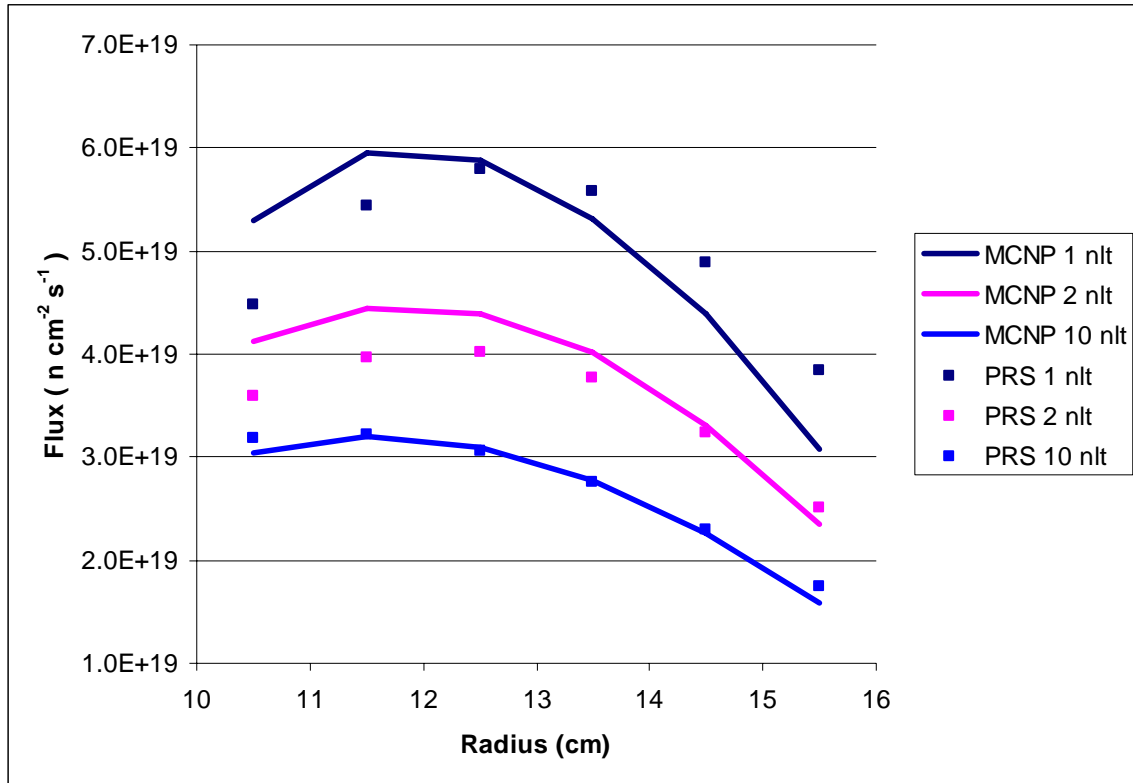


Figure 3.10: Radial flux profile at several times for the point neutron source.

The MCNP radial flux profiles, after 1 and 2 neutron lifetimes, favor the inner radius more than the radial flux profile produced by PRS. After 10 neutron lifetimes, MCNP and PRS produce radial flux profiles that match with each other closely. Differences between PRS and MCNP early in the simulation are due to the lack of uncollided source neutrons in the flux tallies and the delay in re-entrant flux at the inner radius. Once the re-entrant flux begins to bolster the flux at the inner radius, and

uncollided source neutrons have leaked, PRS and MCNP show close agreement. Figure 3.11 shows the axial flux profile of the assembly at several points in time for the point source simulations.

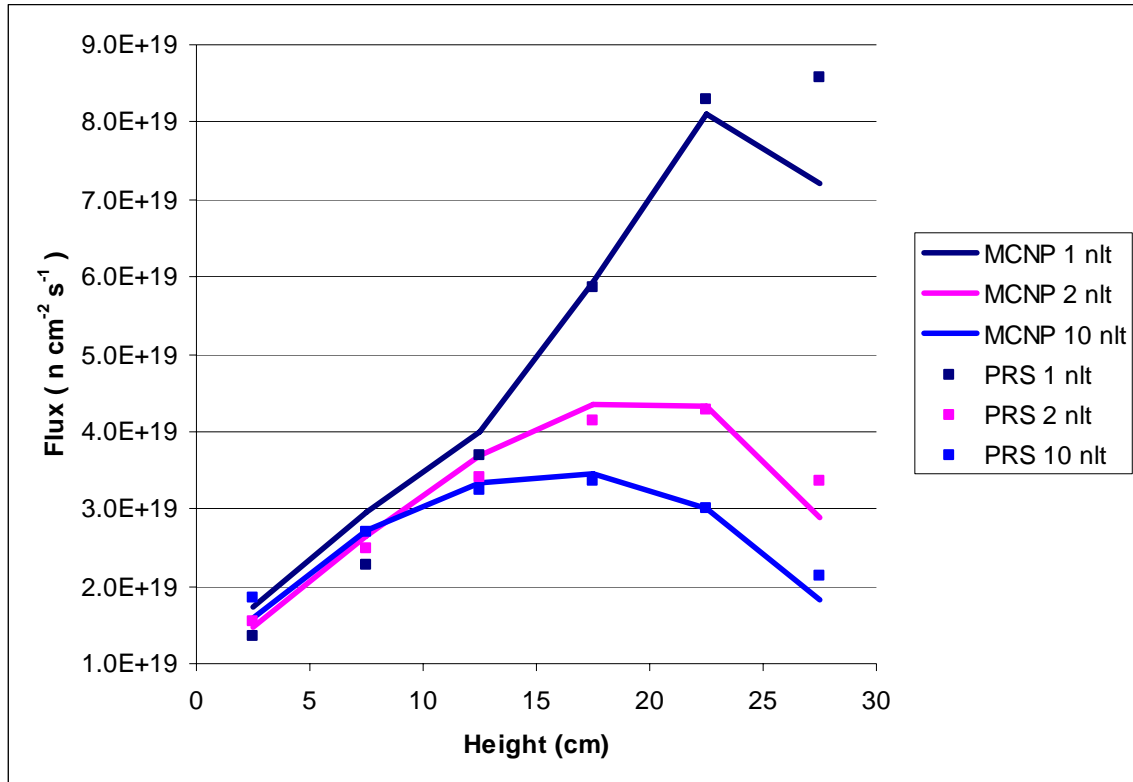


Figure 3.11: Axial flux profile at several times for the point neutron source.

The point and planar external neutron source axial flux profiles are very similar. PRS predicts larger flux values near the top of the assembly initially due to the anisotropic behavior of the once scattered neutrons. After the first couple of neutron lifetimes PRS and MCNP begin to produce the same axial flux profiles.

3.2 SECOND TEST SCENARIO

Accurate criticality predictions from the neutronics module allow the dimensions of the simulated assemblies to closely match the assembly dimensions present during experiments. The second scenario compares the criticality of HEU and LEU assemblies calculated by the neutronics module and MCNP. The inner radius for both enrichments was 5 cm. The outer radii of the HEU and LEU assemblies were 10.94 and 24.8 cm respectively. The heights of the HEU and LEU assemblies were 30 and 40 cm respectively. The dimensions of the HEU and LEU simulations changed to ensure that both assemblies would have k_{eff} values near 1. The second test scenario assembly made of HEU had an MCNP k_{eff} value of 0.99028. The assembly made of LEU had an MCNP k_{eff} value of 0.97967. The second scenario used a smaller inner radius than the first scenario to reduce the size of the assemblies and shorten the amount of computational time required to produce the results.

Six different group structures are present in PRS. The user can reduce the number of groups in a simulation to decrease computational time or increase the number of groups to produce a simulation with a geometry and criticality that more closely matches benchmark results.

The average neutron lifetime is found by taking the neutron density weighted average of the neutron lifetimes of all of the neutron energy groups. The k_{eff} value was found by taking the ratio of the neutron population sizes after a certain number of time steps in the simulation. Time step sizes that are not much smaller than, or equal to, the average neutron lifetime cause the simulation to calculate the ratio of neutron populations either too far apart or too close together. This k_{eff} calculation error is eliminated as the

time step size is reduced because the average neutron lifetime is likely to be near a multiple of the time step size. Figure 3.12 shows how the criticality value predicted by the different group structures changes as the time step size is reduced and grid spacing is equal to the smallest diffusion length for an assembly made of HEU.

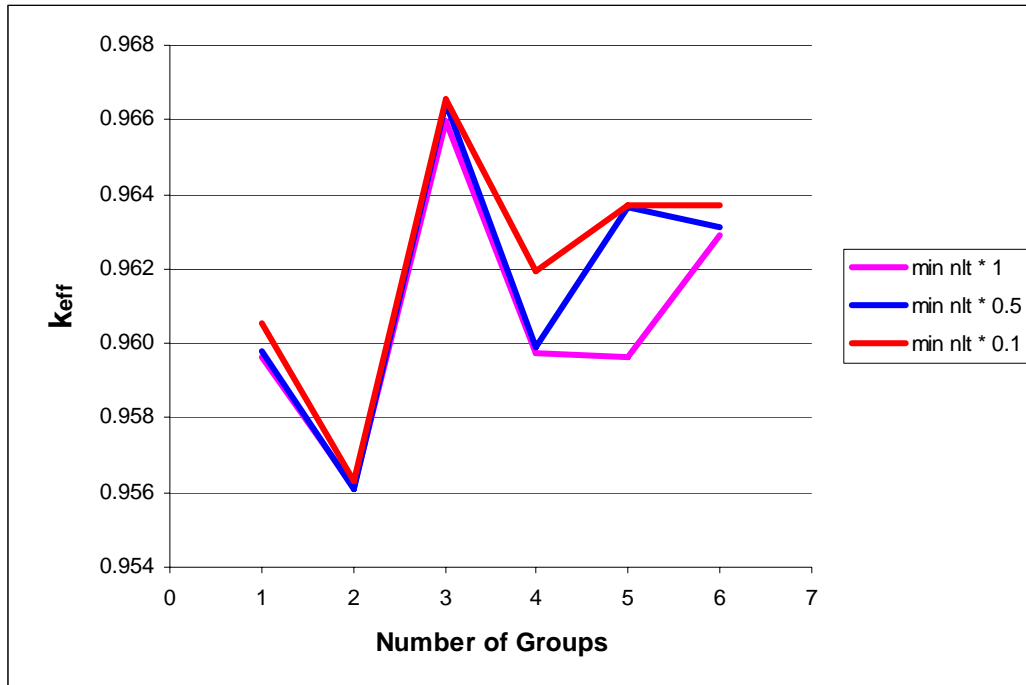


Figure 3.12: Criticality values predicted by PRS for HEU assemblies as time step size is reduced.

The k_{eff} values predicted by the two and three group structures change considerably as the time step is reduced, whereas a reduction in time step size beyond half the minimum neutron lifetime results in very small changes in criticality values for groups 1, 4, 5, and 6. These results are consistent with the time step size and average neutron lifetime synchronization error described above. Figure 3.13 shows how the

criticality value predicted by the different group structures changes as the time step size is reduced and grid spacing is equal to the smallest diffusion length for an assembly made of LEU.

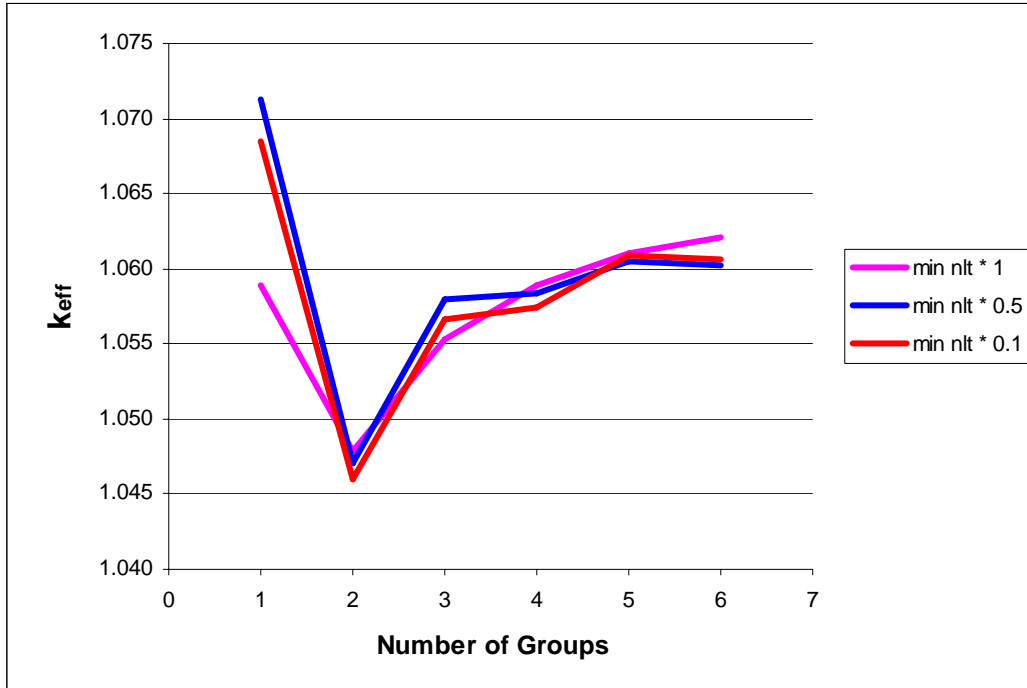


Figure 3.13: Criticality values predicted by PRS for LEU assemblies as dt is reduced.

Criticality values produced for assemblies made of LEU show trends similar to those seen for the assemblies made of HEU. Criticality values from the 2 group neutron energy structure show the largest change as the step size is decreased. Increases in grid resolution caused a much greater increase in computational time than decreases in step size. Figure 3.14 shows how the k_{eff} values predicted by PSR of assemblies made of

HEU for the different group structures changed as the grid resolution was varied from 1.5 to 0.5 with the time step size equal to one tenth of the minimum neutron lifetime.

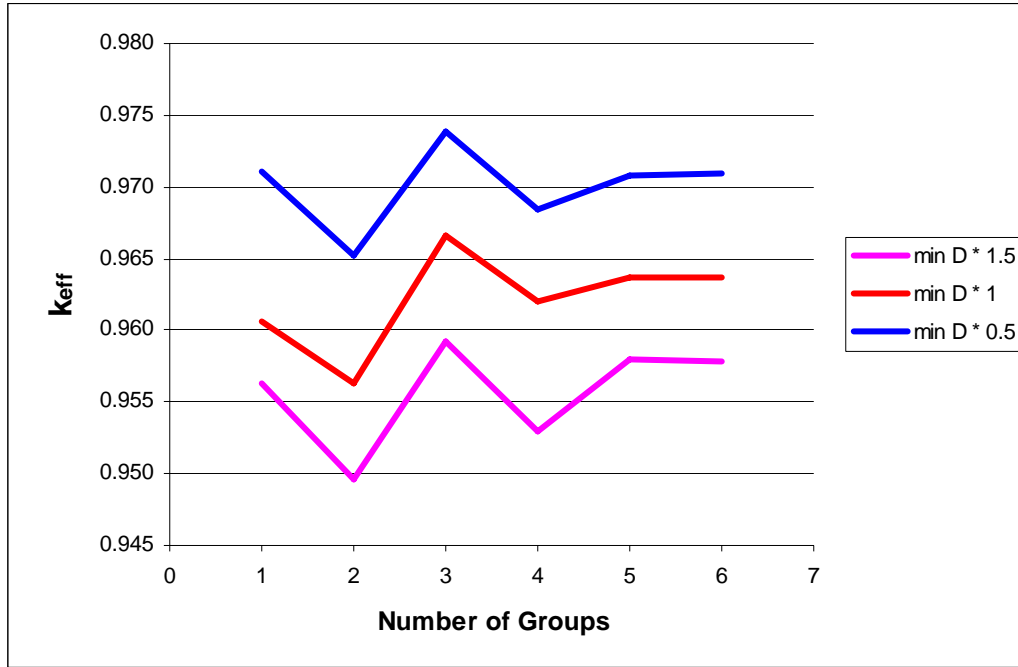


Figure 3.14: Criticality values predicted by PRS for HEU assemblies as grid resolution is increased.

k_{eff} values approach 0.99, the k_{eff} value predicted by MCNP, as the grid resolution increases. The reduced discrepancy between MCNP and PSR can be attributed to the improved the accuracy of the numerical derivatives caused by the smaller distances between nodes. Figure 3.15 shows how the k_{eff} values predicted by PSR of assemblies made of LEU for the different group structures changed as the grid resolution was varied from 1.5 to 0.5 with the time step size equal to the minimum neutron lifetime.

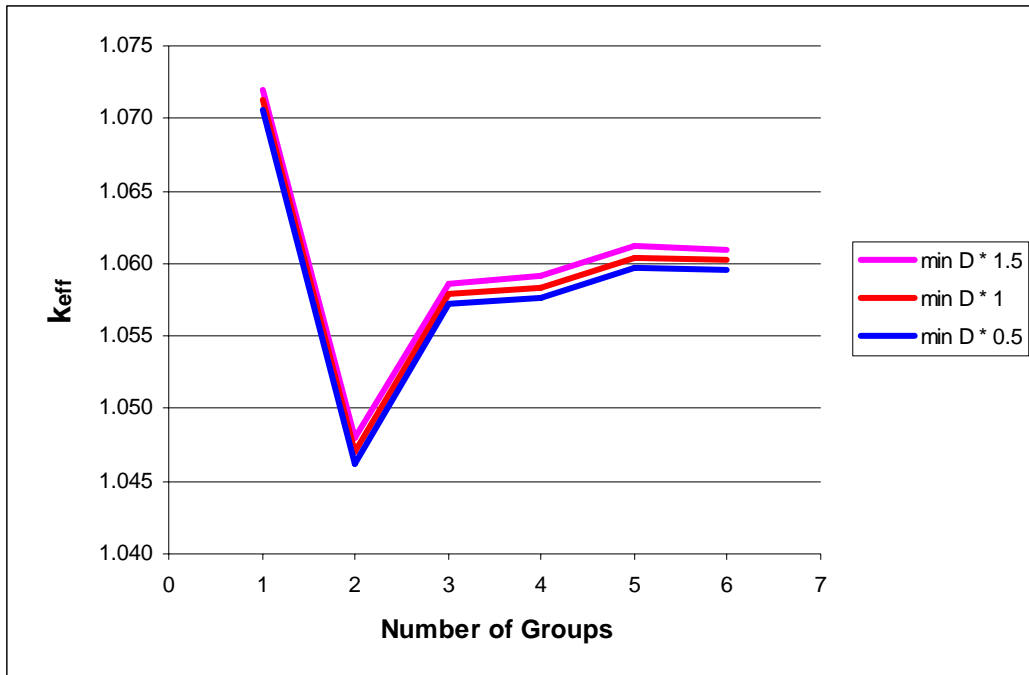


Figure 3.15: Criticality values predicted by PRS for LEU assemblies as grid resolution is increased.

k_{eff} values produced for assemblies made of LEU are not as sensitive to changes in grid resolution as k_{eff} values for assemblies made of HEU. Figure 3.16 compares the criticality values predicted by MCNP and PRS for an assembly made of HEU.

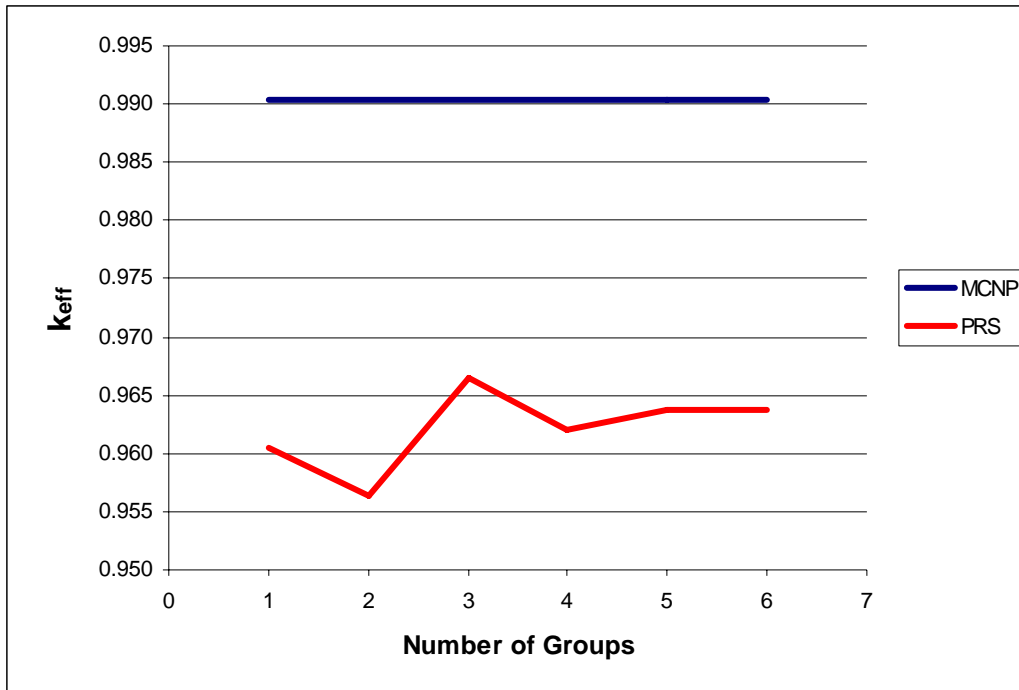


Figure 3.16: Criticality predicted by MCNP and PRS for HEU assemblies with different group structures.

The time step size and grid spacing used during simulations of HEU assemblies significantly influenced the criticality predicted by PRS. In each simulation shown in Figure 3.16 the time step size was one tenth of the minimum neutron lifetime and the grid spacing was equal to the smallest diffusion length. Figure 3.17 shows the criticality values predicted by MCNP and PRS for an assembly made of LEU.

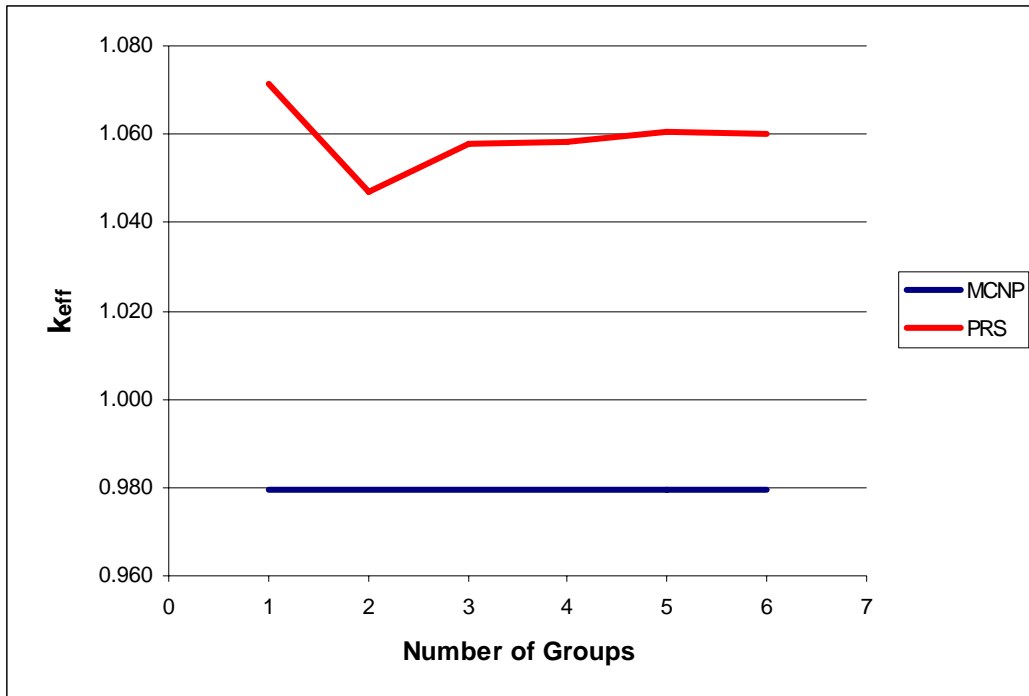


Figure 3.17: Criticality predicted by MCNP and PRS for LEU assemblies with different group structures.

The time step size and grid spacing used during simulations of LEU assemblies had a much smaller influence on the criticality predicted by PRS than in the HEU assembly simulations. In the simulations shown in the Figure 3.17 the time step size was half of the minimum neutron lifetime and the grid spacing was equal to the smallest diffusion length.

It is useful to compare neutron energy spectra produced by PRS to MCNP neutron energy spectra. It was important to compare neutron energy spectra from MCNP and PRS simulations that had settled into their steady state form to remove any bias that might be caused by the initial neutron source. Neutron energy spectra from MCNP were found from decks that ran in kcode mode to remove any initial source bias. Initial source

bias was avoided in the PRS results by using the neutron energy spectrum produced at the end of the criticality calculation. Figure 3.18 compares the 2 group PRS simulation of an assembly made of HEU to MCNP.

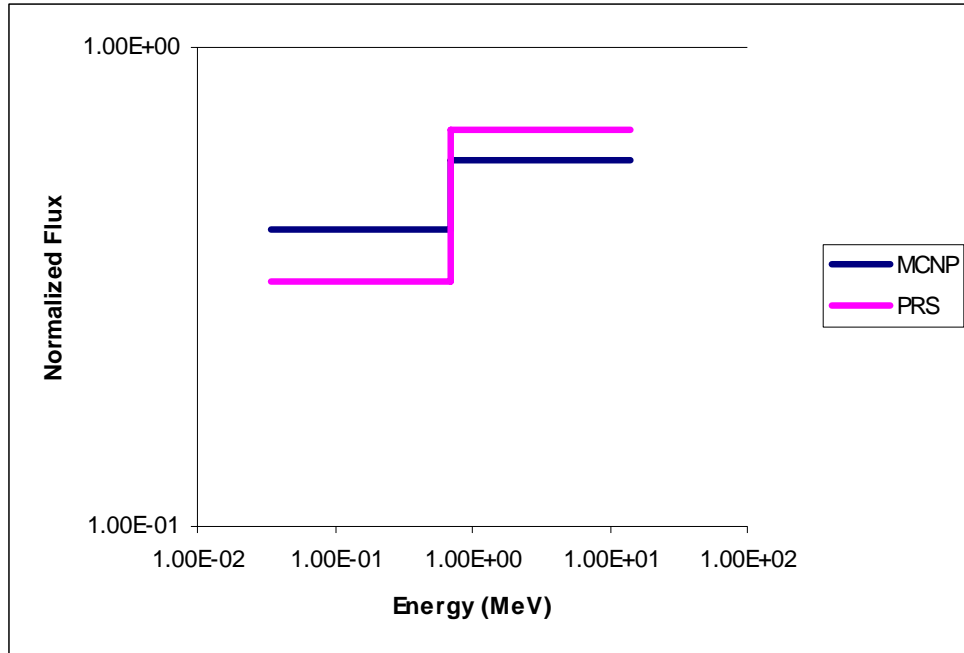


Figure 3.18: Two group neutron energy spectrum for assemblies made of HEU.

MCNP predicts more neutrons in the lower energy group than PRS. The two group simulation had an error of 2.9 % in its criticality prediction when the grid spacing was equal to the diffusion length. Monte Carlo methods of simulating neutron transport are better suited to model neutron down scattering than deterministic neutron transport models with large energy bins. In MCNP neutrons that undergo scattering collisions, at neutron energies well above the thermal range, will loss some fraction of their total energy.

The scattering cross section within a given group is larger than any of the intergroup scattering cross sections unless energy bins are exceedingly small. As a result, a significant portion of scattered neutrons remain in the same group and lose no energy at all. The probability of energy loss for a scattering event, at the high energies in the simulation, does not vary gradually over a large range of energy loss values. If the sharp peak of the energy loss probability function lies within an energy group the likelihood of down scattering will be under predicted because no loss of energy will occur.

Additional error in the simulation of neutron down-scattering was introduced by the incomplete inelastic down scattering information provided by the T-2 Nuclear Information Service. A more comprehensive discussion of the scattering kernel can be found in Section 2.2. As the number of energy bins is increased the error inherent in the deterministic solution will diminish and the PRS neutron energy spectrum will more closely resemble the neutron energy spectrum from MCNP. Figure 3.19 compares the 3 group PRS simulation of an assembly made of HEU to MCNP.

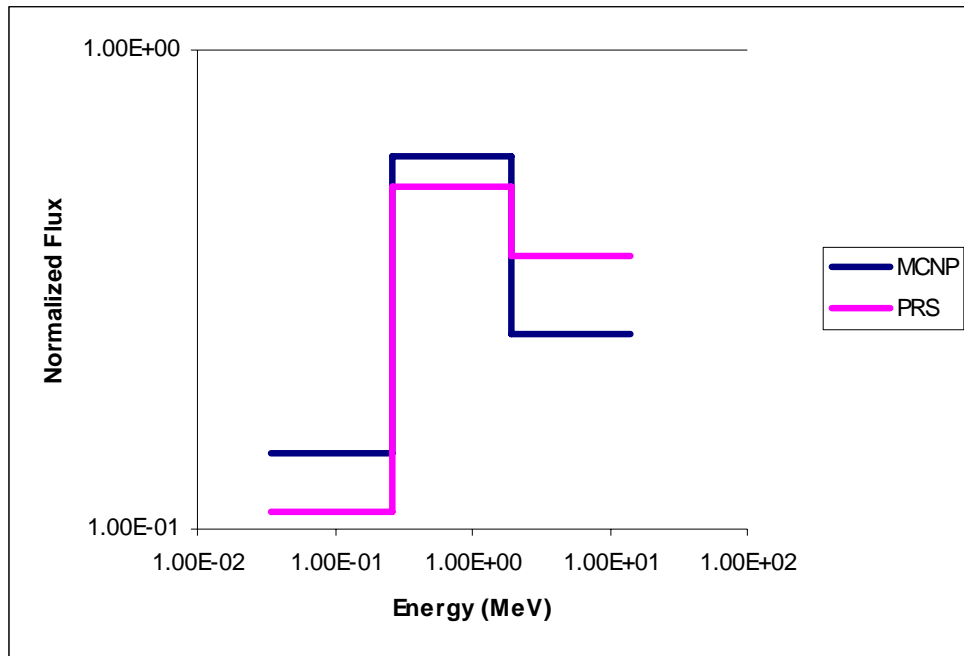


Figure 3.19: Three group neutron energy spectrum for assemblies made of HEU.

The same range of neutron energies is covered with additional energy group. The three group simulation had an error of 1.8 % in its criticality prediction when the grid spacing was equal to the diffusion length. Both PRS and MCNP predict the second group will have the highest flux value. However, the MCNP prediction differs from the PRS prediction with more neutrons in the lowest group and fewer in the highest. Figure 3.20 compares the 4 group PRS simulation of an assembly made of HEU to MCNP.

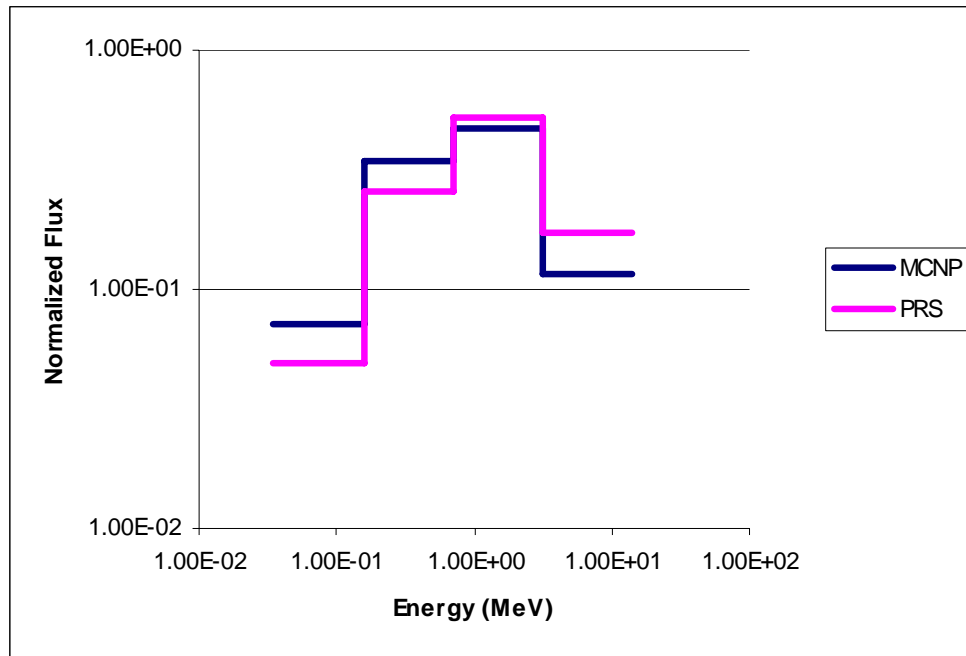


Figure 3.20: Four group neutron energy spectrum for assemblies made of HEU.

The four group simulation had an error of 2.1 % in its criticality prediction when the grid spacing was equal to the diffusion length. The PRS spectrum still has more neutrons in higher energy bins than MCNP. The four group PRS spectrum has 69 % of the spectrum in the two highest energy bins and 31 % of the spectrum in the two lowest energy bins. The two group PRS spectrum had 67 % and 33 % of the neutrons in the high and low energy groups. The likelihood of down scattering to the lower groups has not increased significantly yet. Figure 3.21 compares the 5 group PRS simulation of an assembly made of HEU to MCNP.

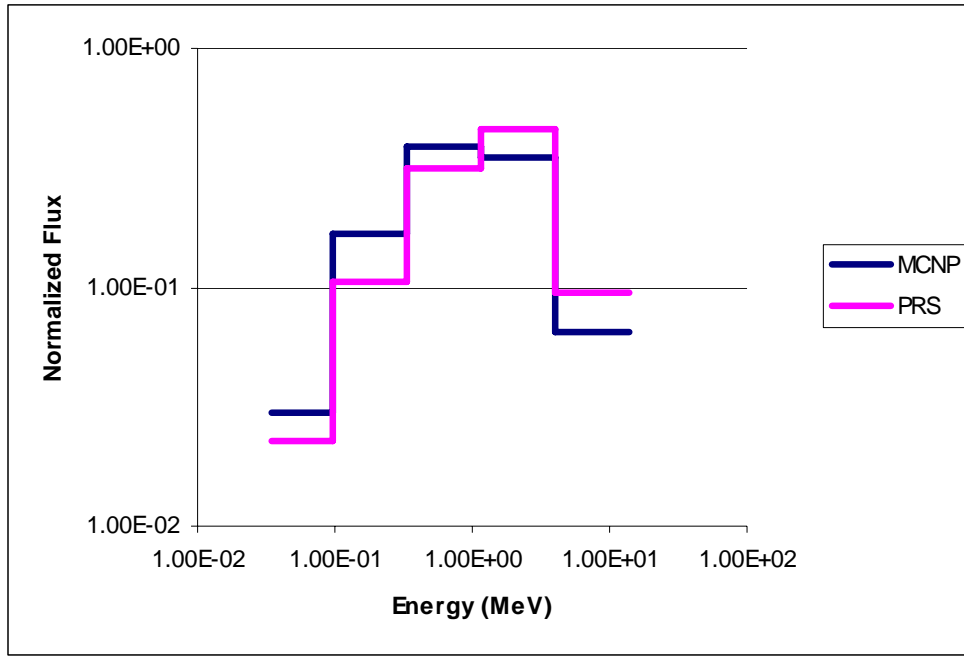


Figure 3.21: Five group neutron energy spectrum for assemblies made of HEU.

The five group simulation had an error of 2.0 % in its criticality prediction when the grid spacing was equal to the diffusion length. The MCNP spectrum continues to have more neutrons in the lower groups than the PRS spectrum. The likelihood of neutron down-scattering below the second highest group remains too low in the PRS simulation. Figure 3.22 compares the 6 group PRS simulation of an assembly made of HEU to MCNP.

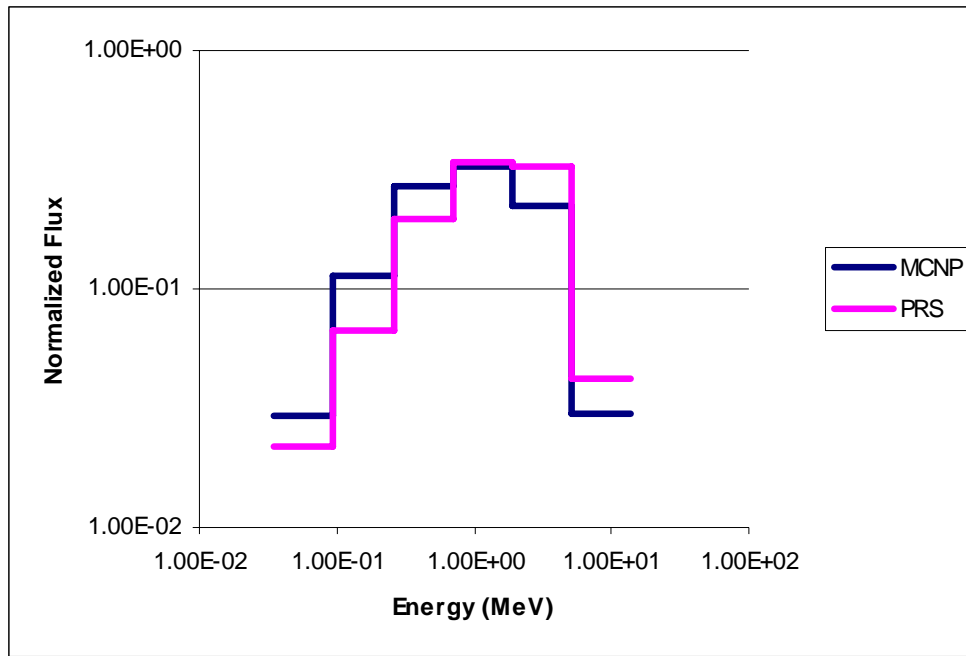


Figure 3.22: Six group neutron energy spectrum for assemblies made of HEU.

The PRS neutron energy spectrum, at the finest energy resolution, for assemblies made of HEU, does not match the MCNP neutron energy spectrum precisely. However, the six group simulation had an error of 1.9 % in its criticality prediction when the grid spacing was equal to the diffusion length. Additional energy groups were not added because they would make pulse simulations prohibitively time consuming on a desktop computer. Figure 3.23 compares the 2 group PRS simulation of an assembly made of LEU to MCNP.

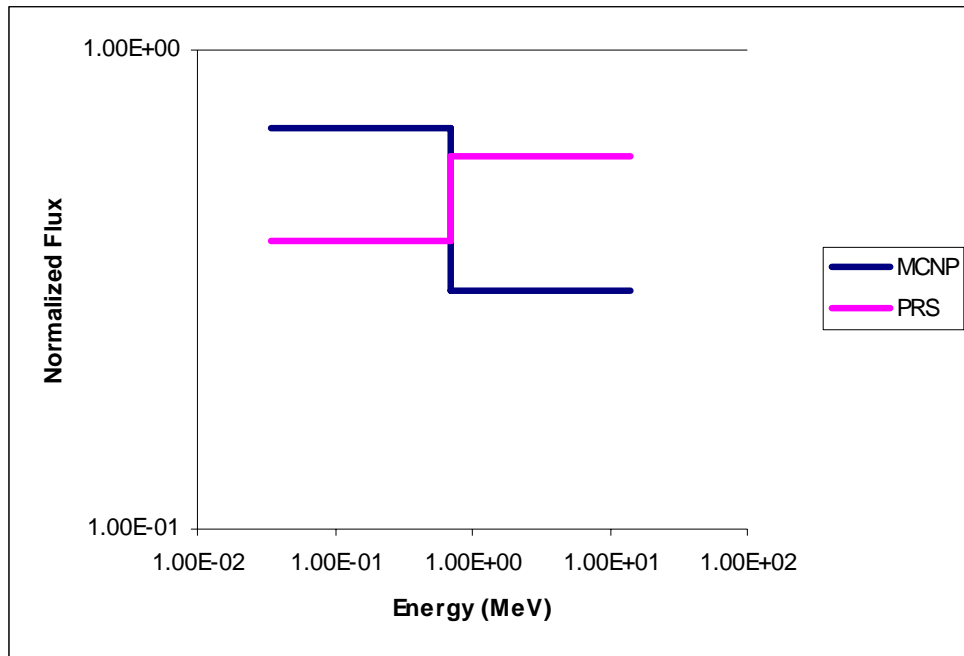


Figure 3.23: Two group neutron energy spectrum for assemblies made of LEU.

MCNP predicts more neutrons in the lower energy group than the higher energy group, while PRS predicts the opposite. The two group simulation had an error of 6.4 % in its criticality prediction when the grid spacing was equal to the diffusion length. Figure 3.24 compares the 3 group PRS simulation of an assembly made of LEU to MCNP.

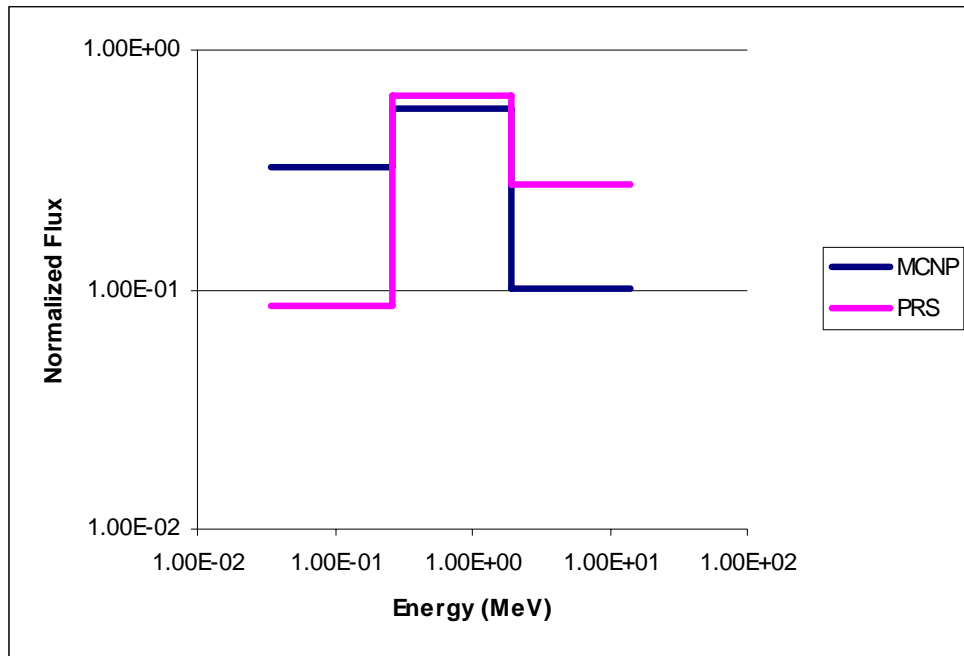


Figure 3.24: Three group neutron energy spectrum for assemblies made of LEU.

The three group simulation had an error of 7.1 % in its criticality prediction when the grid spacing was equal to the diffusion length. Both PRS and MCNP predict the second group will have the highest flux value. Figure 3.25 compares the 4 group PRS simulation of an assembly made of LEU to MCNP.

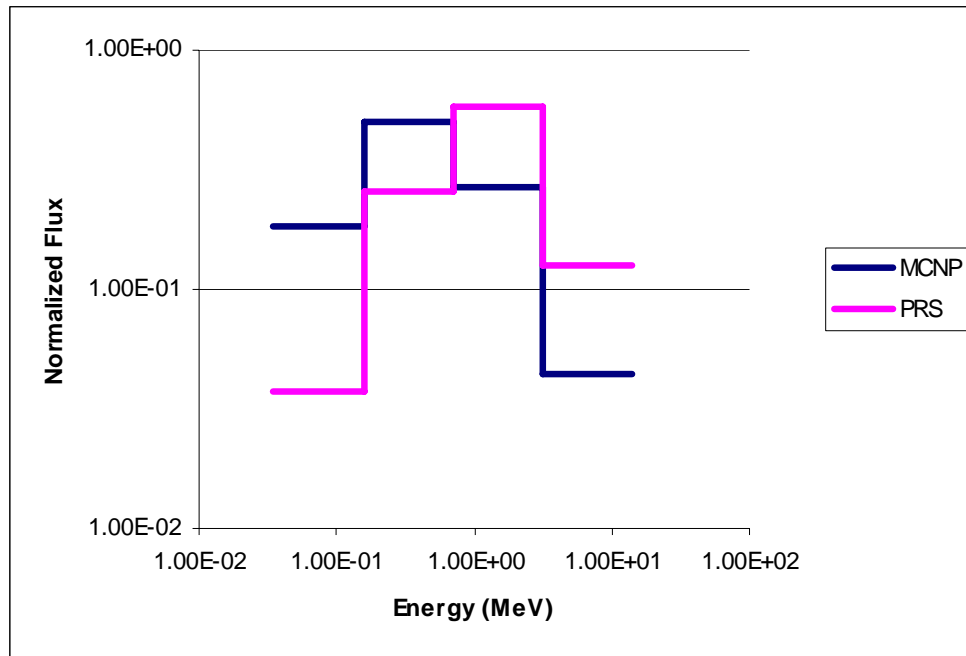


Figure 3.25: Four group neutron energy spectrum for assemblies made of LEU.

The four group simulation had an error of 7.0 % in its criticality prediction when the grid spacing was equal to the diffusion length. The error in down scattering probability is most prominent in the second highest group. The MCNP spectrum has a much larger low energy group presence in the LEU simulation because scattering is more likely with a larger scattering to absorption cross section ratio, and more scattering events occur before leakage due to the larger assembly size. Figure 3.26 compares the 5 group PRS simulation of an assembly made of LEU to MCNP.

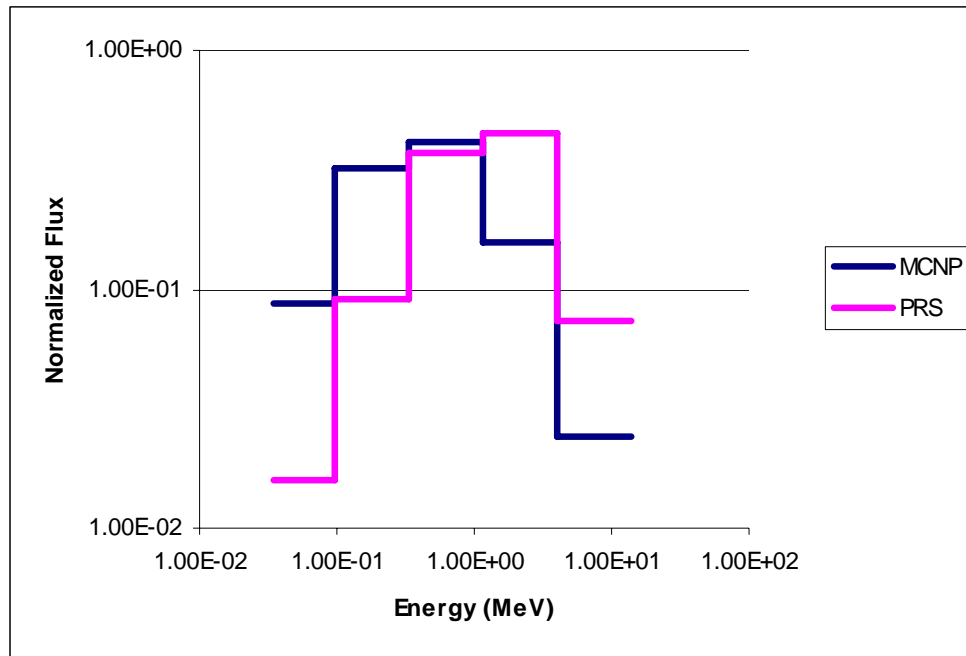


Figure 3.26: Five group neutron energy spectrum for assemblies made of LEU.

The five group simulation had an error of 7.4 % in its criticality prediction when the grid spacing was equal to the diffusion length. The highest energy bins are too large to accurately simulate down scattering. The peak of the neutron energy loss probability function places neutrons at energies that are lower than the scattering energy but not low enough to escape the group where the scattering event occurred. Figure 3.27 compares the 6 group PRS simulation of an assembly made of LEU to MCNP.

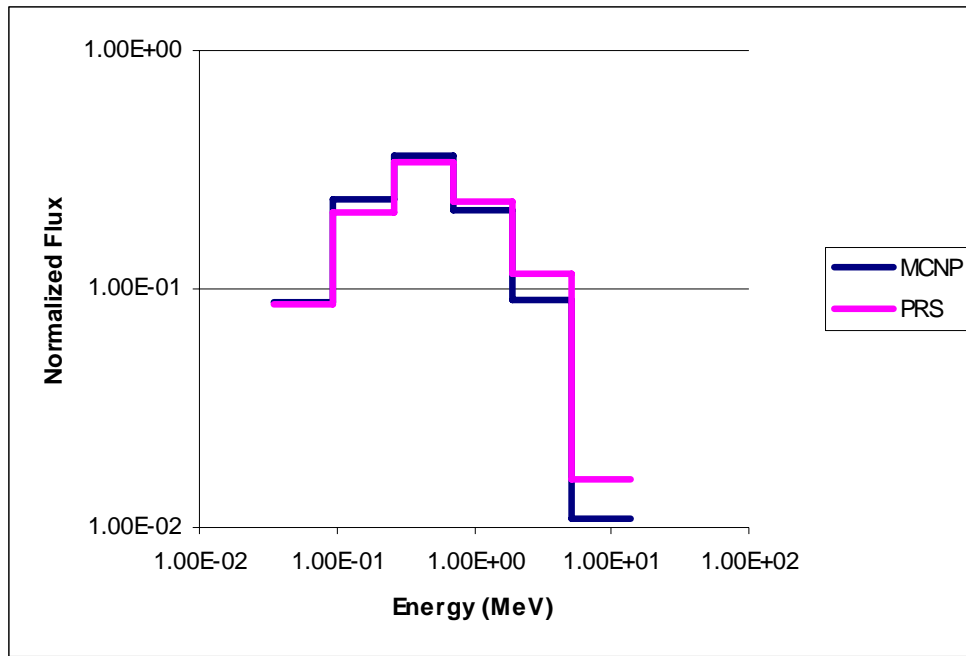


Figure 3.27: Six group neutron energy spectrum for assemblies made of LEU.

The six group simulation had an error of 7.2 % in its criticality prediction when the grid spacing was equal to the diffusion length. The elastic scattering cross section at the highest energy group for scattering events that send neutrons to the group below is an order of magnitude larger in the six group simulation than the five group simulation. Neutrons that are born in the highest group are much more likely to escape the highest group in the six group simulation than the five group simulation.

Chapter 4: Heat Transfer Benchmarking

The temperature profile of the assembly directly influences the magnitude and shape of the displacement profile. If heat transfer by conduction smoothes out the temperature profile the displacement profile will also become smoother. The assembly used in the heat transfer benchmarking had inner and outer radii of 10 and 16 cm respectively and a height of 30 cm. The assembly density, thermal conductivity, and specific heat are $18.134 \text{ (g cm}^{-3}\text{)}$, and $1000 \text{ (W m}^{-1} \text{ K}^{-1}\text{)}$, and $150 \text{ (J kg}^{-1} \text{ K}^{-1}\text{)}$ respectively. The heating function shown in Equation 4-1 was placed in the PRS and COMSOL programs to compare the heat transfer modules.

$$\dot{Q}'''(r, z) = 1 \times 10^{14} \frac{\pi^2}{4} \sin\left(\frac{\pi(r - r_{inner})}{(r_{outer} - r_{inner})}\right) \cos\left(\frac{\pi z}{h} - \frac{\pi}{2}\right) \quad (4-1)$$

The units of the heating function were in Watts per cubic meter. The heating function was shut off after $1 \text{ } \mu\text{s}$, yielding a total of 1.47 MJ of energy deposited into the assembly from the heat source. The temperature profile at the middle of the assembly axially was recorded every ms up to 1 s after the pulse. Values were recorded beginning at 1 ms because even with a very large thermal conductivity value the temperature profile remains virtually unchanged from the end of the pulse until 1 ms later. Figure 4.1 shows how the temperature profile values predicted by PRS 1 s after the pulse change as the time step size is altered.

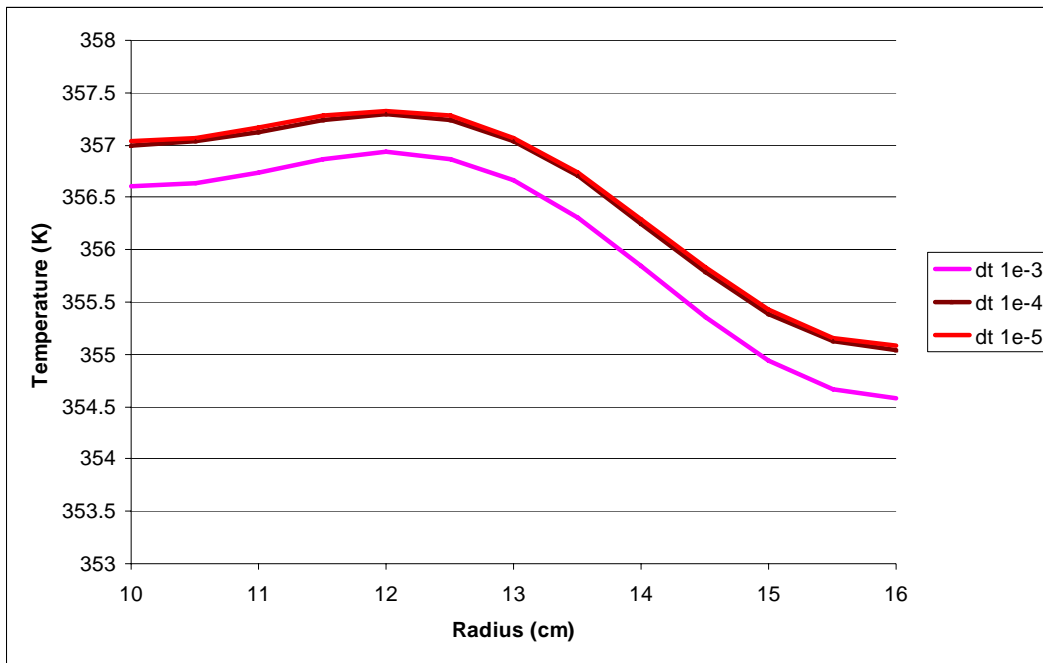


Figure 4.1: Convergence of PRS temperature profiles with decreasing time step size.

The time step size for all of the following heat transfer simulations is 10^{-5} s. The time step size was increased to 10^{-4} s and 10^{-3} s to ensure that the temperature profile values had converged to the correct answer. Figure 4.1 shows that further reductions in time step size would yield changes in the temperature profile values that can be assumed to be negligible. Figure 4.2 shows how the temperature profile values predicted by PRS 1 ms after the pulse change as the distance between nodes are altered.

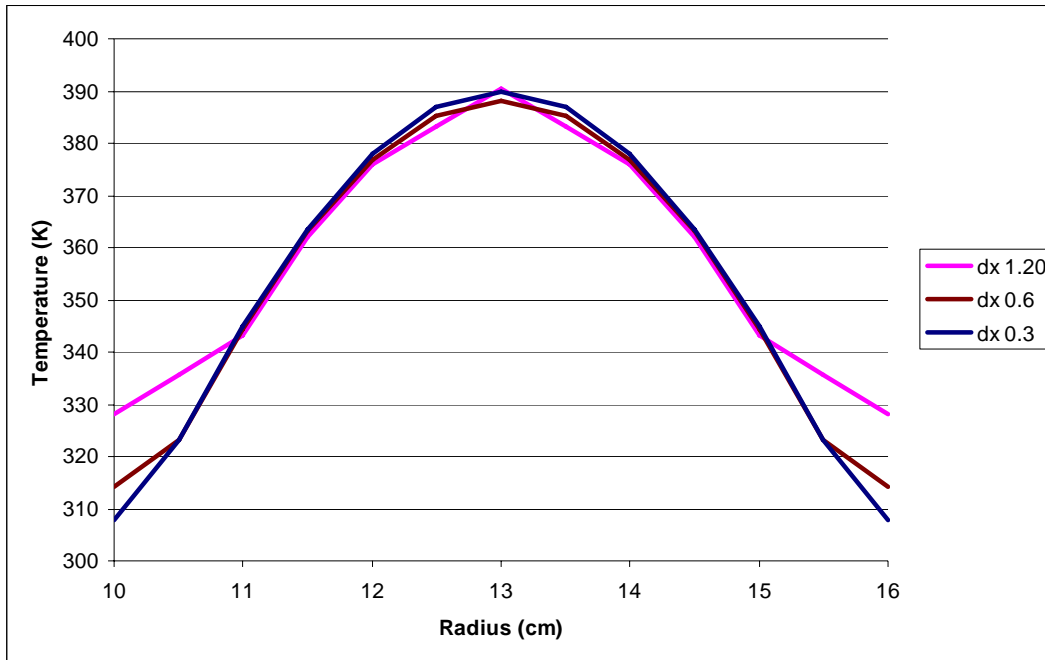


Figure 4.2: Convergence of PRS temperature profiles with decreasing dx .

The distance between nodes for all of the previous heat transfer simulations was 0.3 cm. The distance between nodes was varied from 1.20 cm to 0.3 cm to ensure that the temperature profile values had converged to the correct answer. The largest difference between the different temperature profiles are the boundary value temperatures. As the grid resolution becomes finer the temperature at the boundaries approaches 300 K. Figure 4.3 shows the radial temperature profile from PRS and COMSOL at the middle of the assembly axially, after 1 ms.

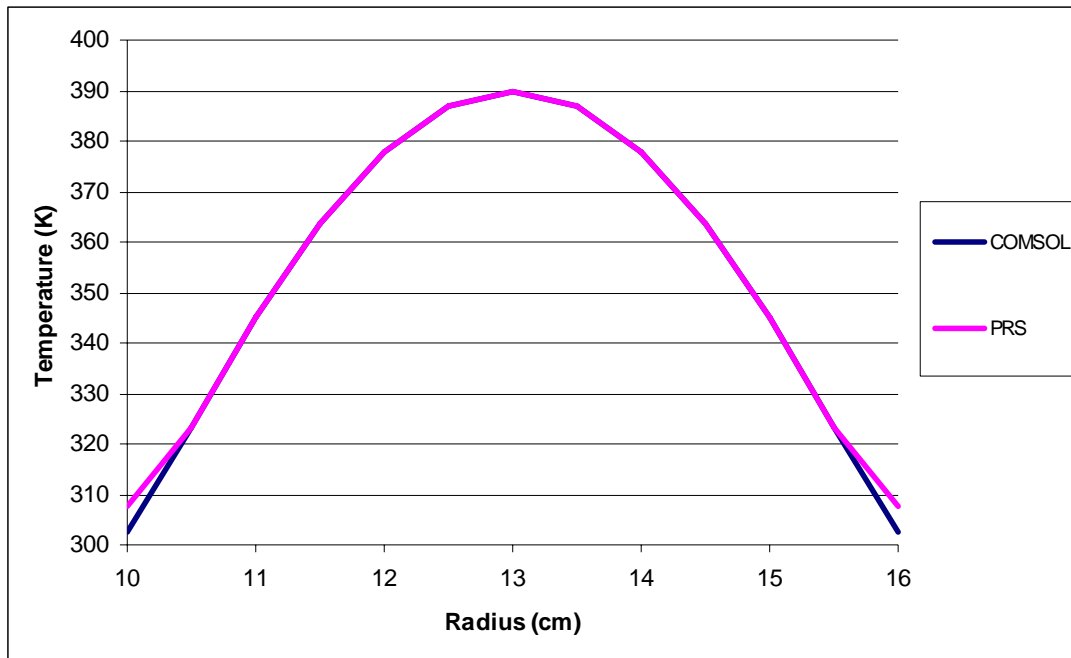


Figure 4.3: COMSOL and PRS temperature profiles after 1 ms.

The temperature profile matches very closely away from the boundaries. Discrepancies near the boundaries can be attributed to differences in the grid resolution. Figure 4.4 shows the radial temperature profile from PRS and COMSOL at the middle of the assembly axially, after 10 ms.

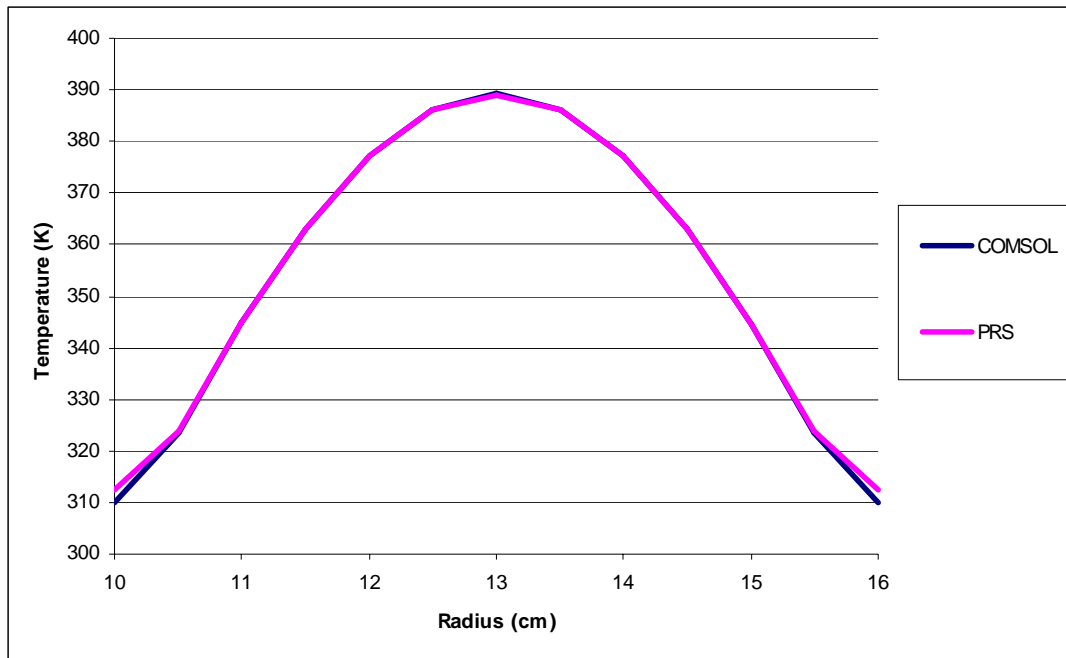


Figure 4.4: COMSOL and PRS temperature profiles after 10 ms.

After 10 ms the temperature profiles from PRS and COMSOL match very closely. Pulse simulations are not likely to last beyond 1 much less 10 ms. However, the temperature profile comparison is carried out further to observe differences between the two simulations. Figure 4.5 shows the radial temperature profile from PRS and COMSOL at the middle of the assembly axially, after 0.1 seconds.

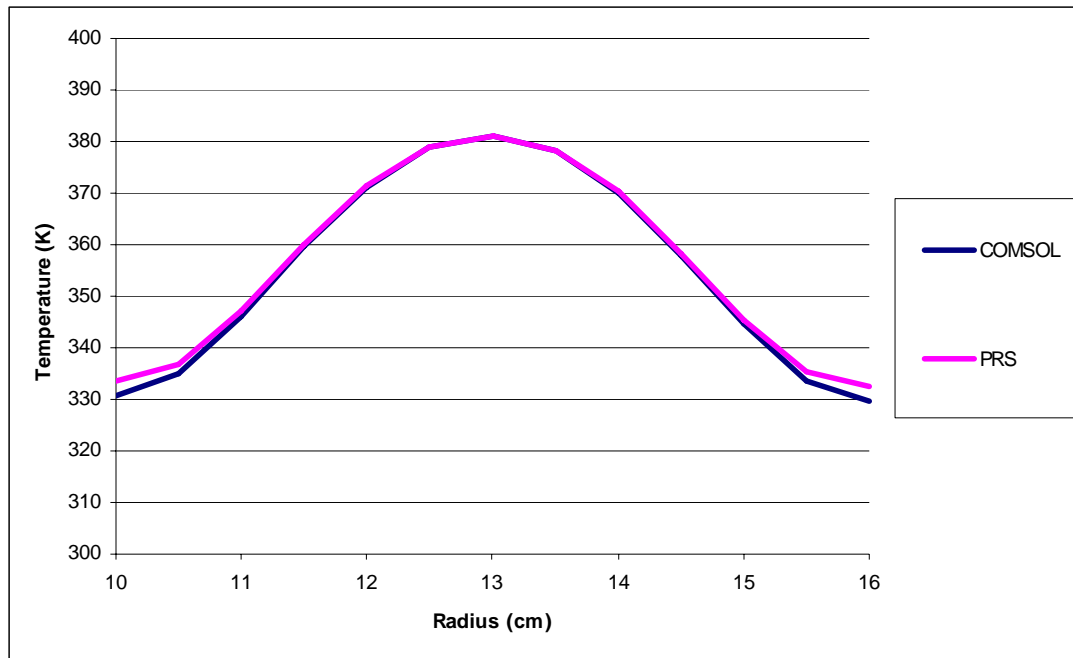


Figure 4.5: COMSOL and PRS temperature profiles after 0.1 seconds.

After 0.1 seconds the effects of heat transfer are easily noticeable. Temperatures near a radius of 13 cm decreased roughly 10 degrees K, and temperatures near the boundaries have risen nearly 30 degrees K. Figure 4.6 shows the radial temperature profile from PRS and COMSOL at the middle of the assembly axially, after 1 s.

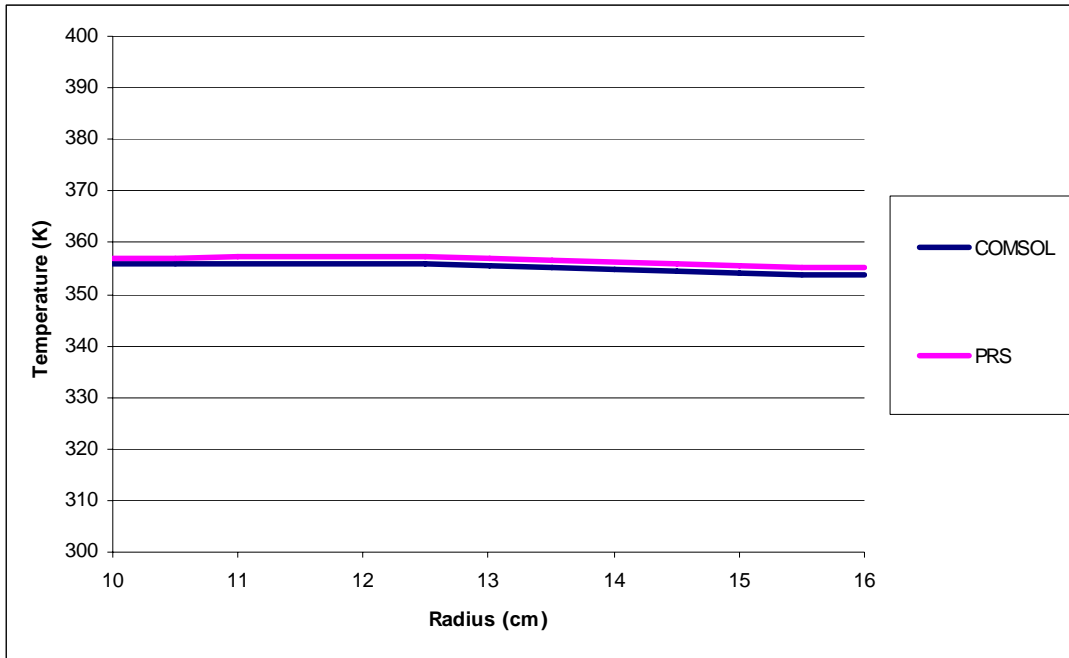


Figure 4.6: COMSOL and PRS temperature profiles after 1 s.

After 1 s the temperature profile is nearly flat. The largest difference in temperature values between PRS and COMSOL is no more than 2 degrees K.

In the course of one time step in the PRS simulation the heat transfer module follows the neutronics module and the mechanics module follows the heat transfer module. The next chapter will present an isolated comparison of the mechanics module and COMSOL during a simulation with the same heat source present in the current chapter.

Chapter 5: Mechanics Benchmarking

It is important to accurately model the thermal expansion of SPR pulses because it serves as the primary shut down mechanism. The ZEDNA concept employs a sub-critical assembly that eliminates the need for an intra-pulse shut down mechanism to prevent unsafe power excursions. However, it is still important to model thermal expansion in ZEDNA pulses to predict the stresses that are induced and any affect the thermal expansion might have on the assembly's ability to boost the external neutron source. The assembly used in the mechanics benchmarking had inner and outer radii of 10 and 16 cm respectively and a height of 30 cm. The assembly density, modulus of elasticity, Poisson's ratio and specific heat are $18.134 \text{ (g cm}^{-3}\text{)}$, 82 (GPa), 0.38, and $150 \text{ (J kg}^{-1} \text{ K}^{-1}\text{)}$ respectively. The heating function shown in Equation 4-1 was also used in the current chapter to isolate the mechanics module and compare it directly to a mechanics simulation run in COMSOL.

The heating function is turned off after $1 \text{ }\mu\text{s}$ in the simulation. The heating function is shaped in a sinusoidal fashion and turned of after a short amount of time to mimic the behavior of SPR and ZEDNA pulses. Due to the one dimensional nature of the mechanics equations, roller boundary conditions were imposed at the top and bottom of the COMSOL simulation. The maximum radial displacement and temperature rise

occurred at the axial center of the assembly. Figure 5.1 shows how the displacement at the inner radius predicted by PRS changes as the time step size is altered.

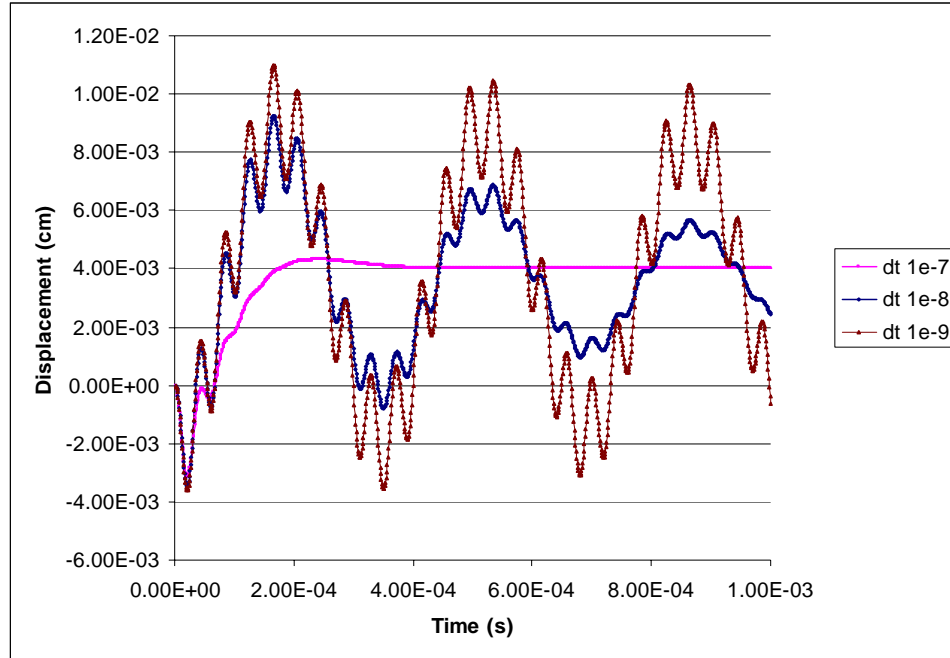


Figure 5.1: Time step convergence of the mechanics module.

The time step size used in the following PRS simulations is 10^{-9} s. The simulation was also run with time step sizes of 10^{-8} s and then 10^{-7} s to observe the changes in the displacement values predicted. As the time step size is increased the reduction in the size of the oscillation amplitude over time grows. This energy loss is due to the increased effects of truncation errors in the numerical derivatives as the step size is increased. Figure 5.2 shows how the displacement at the inner radius predicted by COMSOL changes as the time step size is altered.

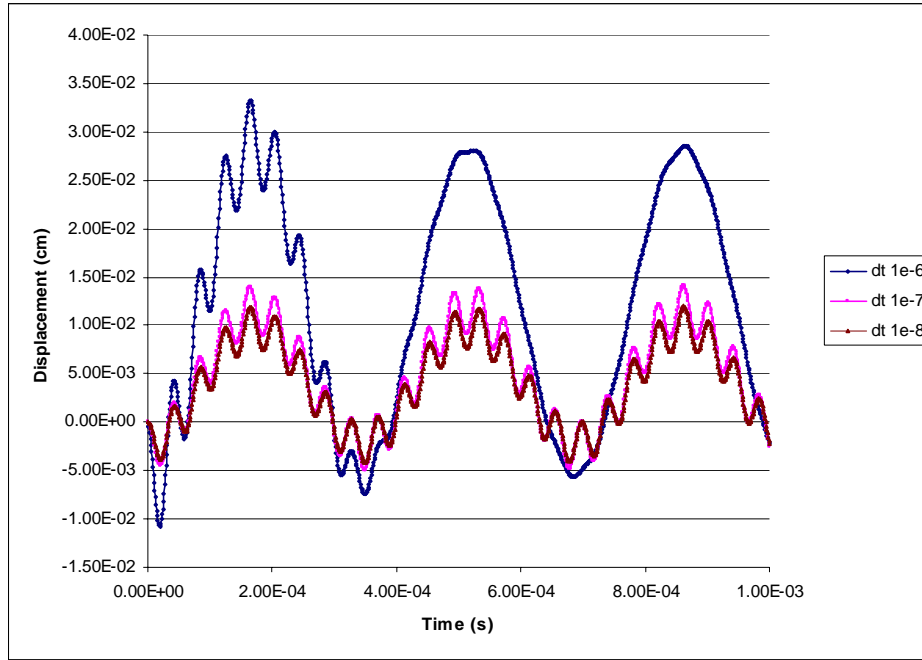


Figure 5.2: Time step convergence of COMSOL.

As the COMSOL time step size was increased from 10^{-8} s to 10^{-6} s the high frequency oscillation was dampened out and the low frequency oscillation became far too large. The time step used in the following simulations by COMSOL is 10^{-8} s. The effect of truncation error in the numerical derivatives in COMSOL is to add energy to the system. Differences in COMSOL and PRS vanish as the time step size is brought to zero. However, small differences in COMSOL and PRS can be expected for any finite step size due to the different choice of numerical derivative scheme.

The spatial distance between solution points also affected the error in displacement values. The ratio of the distance between grid points over the time step size must be significantly larger than the maximum wave propagation speed in the assembly.

The maximum wave propagation speed in an assembly can be found using Equation 5-1 shown below.

$$c = \sqrt{\frac{E(1-\nu)}{(1+\nu)(1-2\nu)\rho}} \quad (5-1)$$

Where E is the modulus of elasticity, ν is Poisson's ratio, and ρ is the density. Figure 5.3 shows how the displacement at the inner radius changes as the step size is held constant and the distance between grid points is increased.

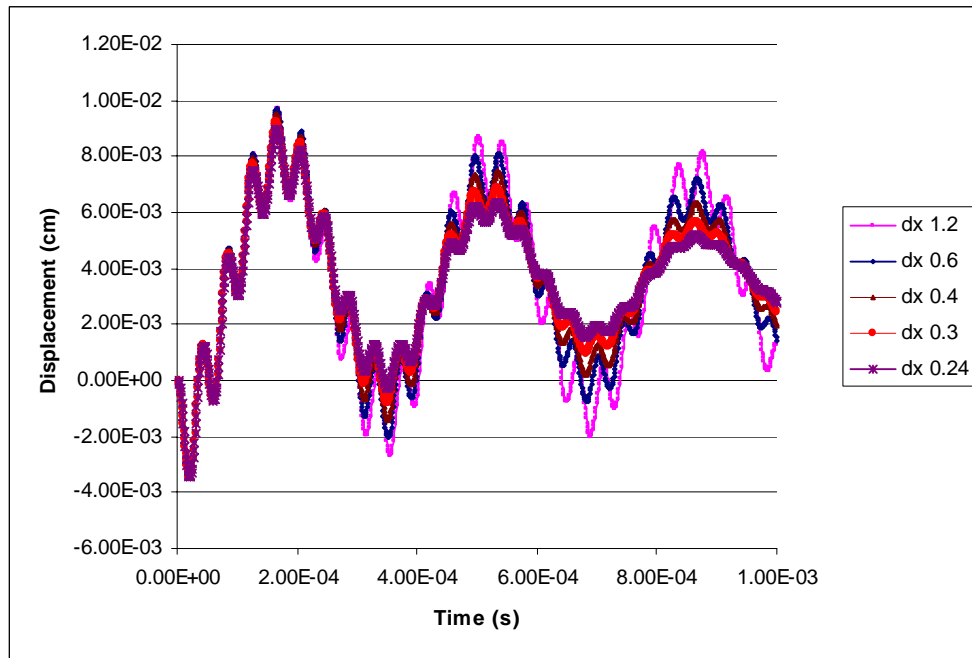


Figure 5.3: Grid resolution convergence for PRS.

The distance between nodes was varied from 1.2 cm to 0.24 cm. As the distance between nodes decreases, error in the solution begins to grow. The increased dampening seen in figure 5.3 may be attributed to the inability of simulations with higher grid resolutions to capture all of the waves propagating through the assembly because the ratio of node distance and time step size is too small.

Displacement values at the middle of the assembly axially, from the inner to the outer assembly radius were recorded at 1 μ s intervals from the beginning of the pulse to 1 ms after the pulse. Figure 5.4 shows the displacement at the outer radius in PRS and COMSOL from the beginning of the simulation to 100 μ s after the pulse.

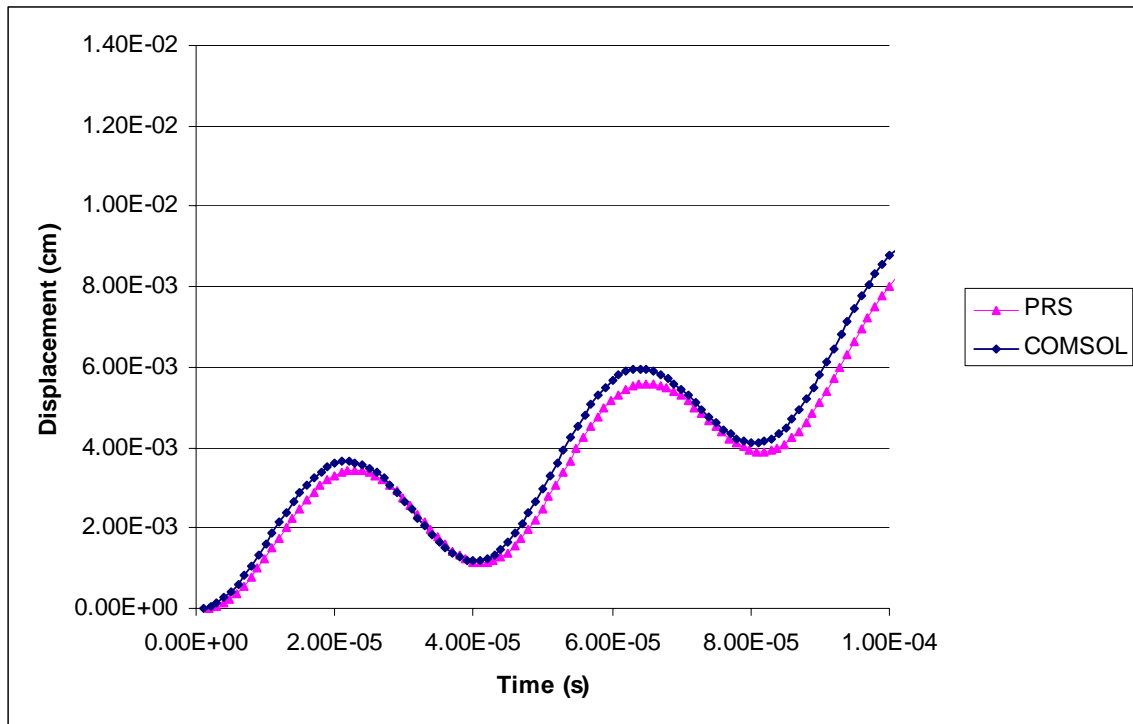


Figure 5.4: Displacement of the outer radius of the assembly, 100 μ s.

Despite the fact that the heat source is shut off after 1 μs , inertial effects cause the assembly to continue to expand. The general trend is for the assembly to expand in the first 100 μs despite the short oscillations. Figure 5.5 shows the displacement at the outer radius in PRS and COMSOL from the beginning of the simulation to 1 ms after the pulse.

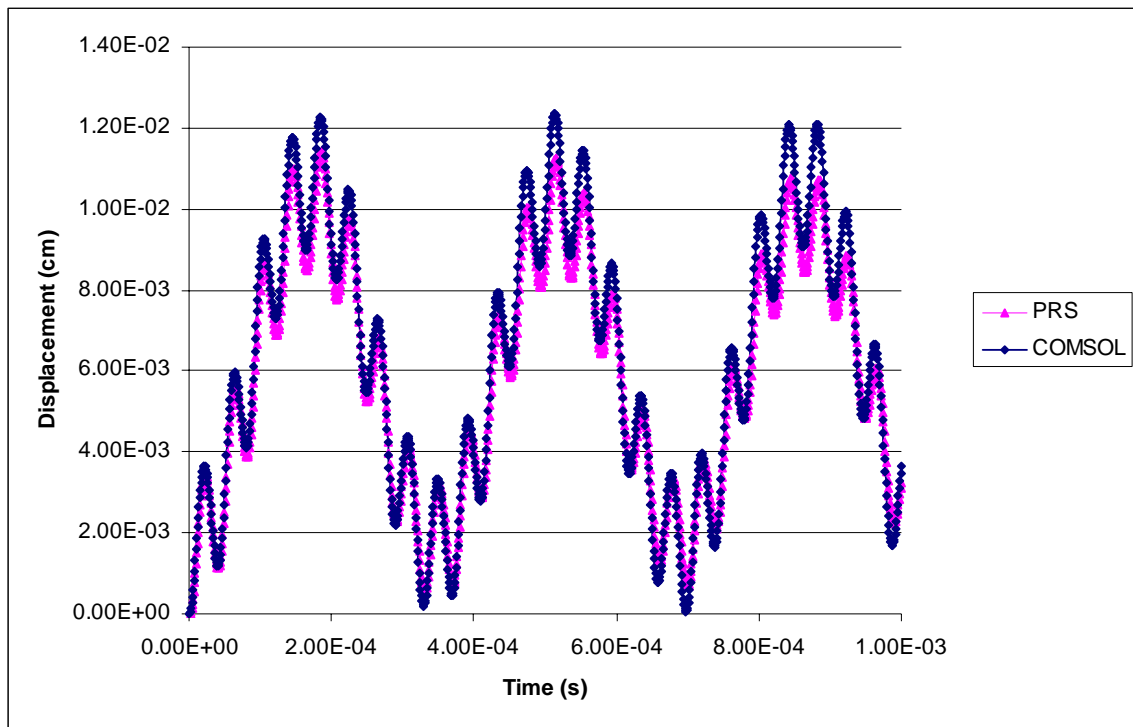


Figure 5.5: Displacement of the outer radius of the assembly, 1 ms.

In Figure 5.5 one can see that the outer radius is oscillating with two different frequencies. The slowly declining PRS values show that the time stepping scheme it uses slowly loses energy, while the COMSOL time stepping scheme appears to conserve

energy quite well. Since the equations used in the mechanics module do not account for dampening, the amplitude of the low frequency oscillations should remain constant. Time step convergence tests will confirm that errors between PRS and COMSOL are merely due to differences in step sizes and the methods used to solve the equations. Figure 5.6 shows the displacement at the inner radius in PRS and COMSOL from the beginning of the simulation to 100 μs after the pulse.

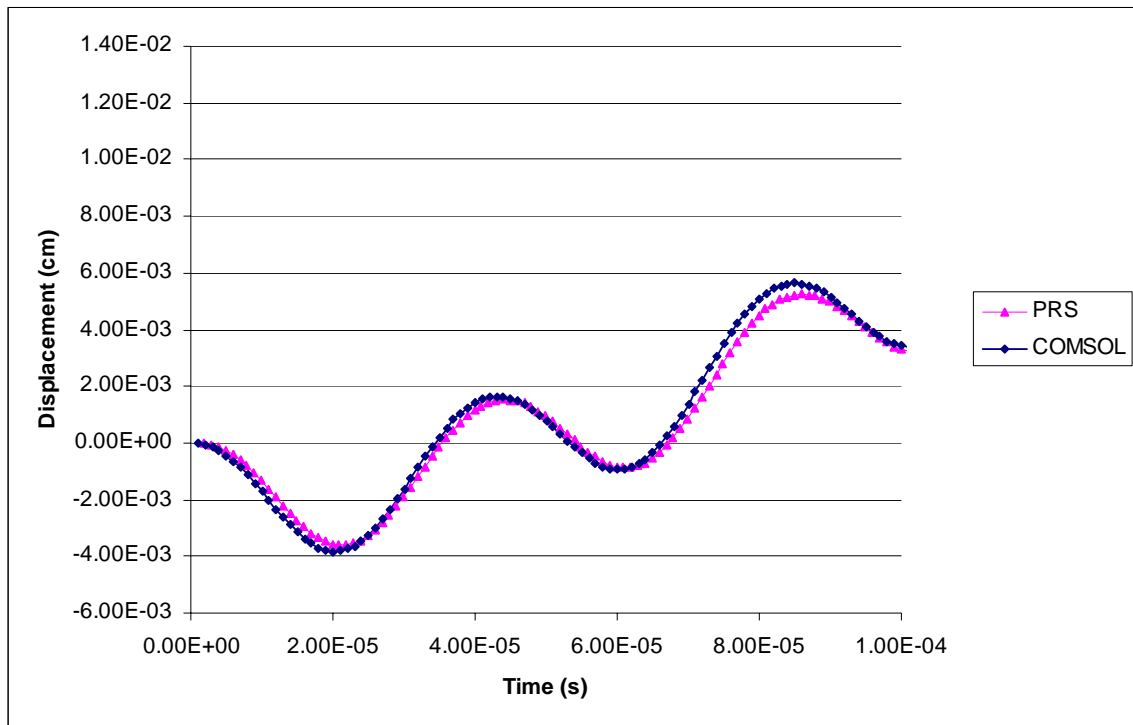


Figure 5.6: Displacement of the inner radius of the assembly, 100 μs .

In Figure 5.6 one can see that the inner radius contracts at the beginning of the pulse and then begins to expand after 2 μs . Intuitively, one expects objects to always

expand as they are heated. However, the rapid heating of the assembly between the inner and outer radii cause this portion of the assembly to expand, pushing areas inside the midway point between the inner and outer radii inward. Figure 5.7 shows the displacement at the inner radius in PRS and COMSOL from the beginning of the simulation to 1 ms after the pulse.

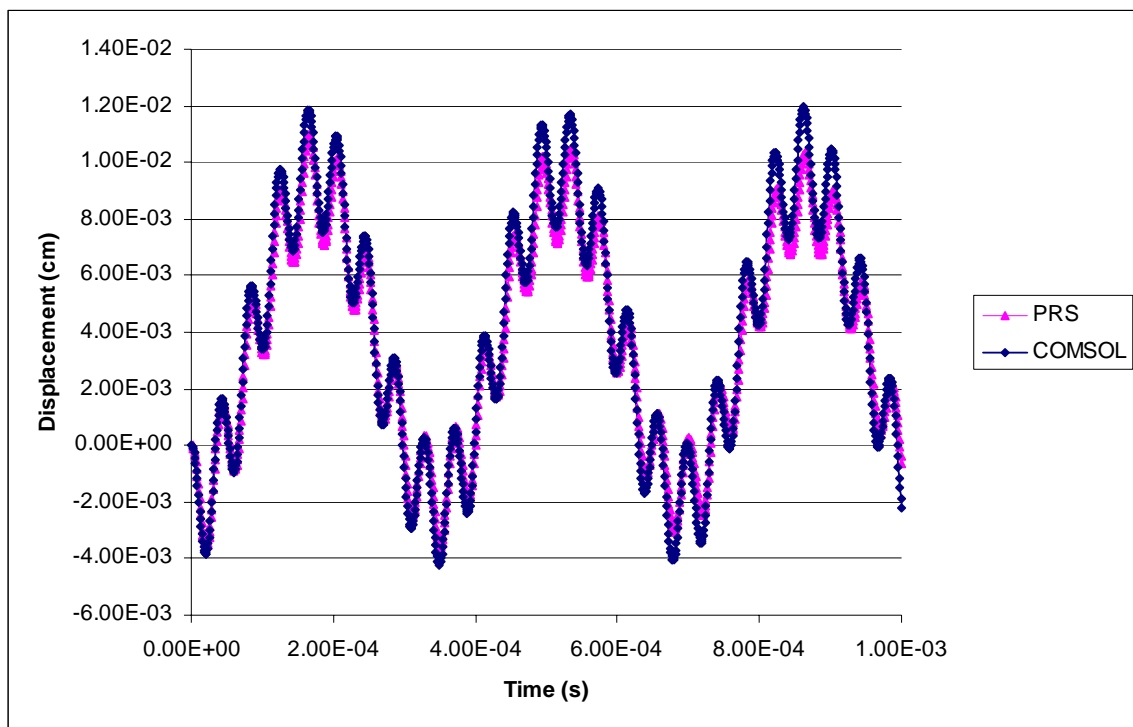


Figure 5.7: Displacement of the inner radius of the assembly, 1 ms.

The low and high frequency oscillations may also be seen at the inner radius. The amplitude of the oscillations should not decrease and the assembly should oscillate indefinitely if the deformation is perfectly elastic and there is no dampening, as the

mechanics equations would indicate. Figure 5.8 shows the displacement profile predicted by PRS and COMSOL at 20 μs , roughly the point where the inner radius contraction is the largest, and 160 μs , roughly the peak of the first displacement oscillation.

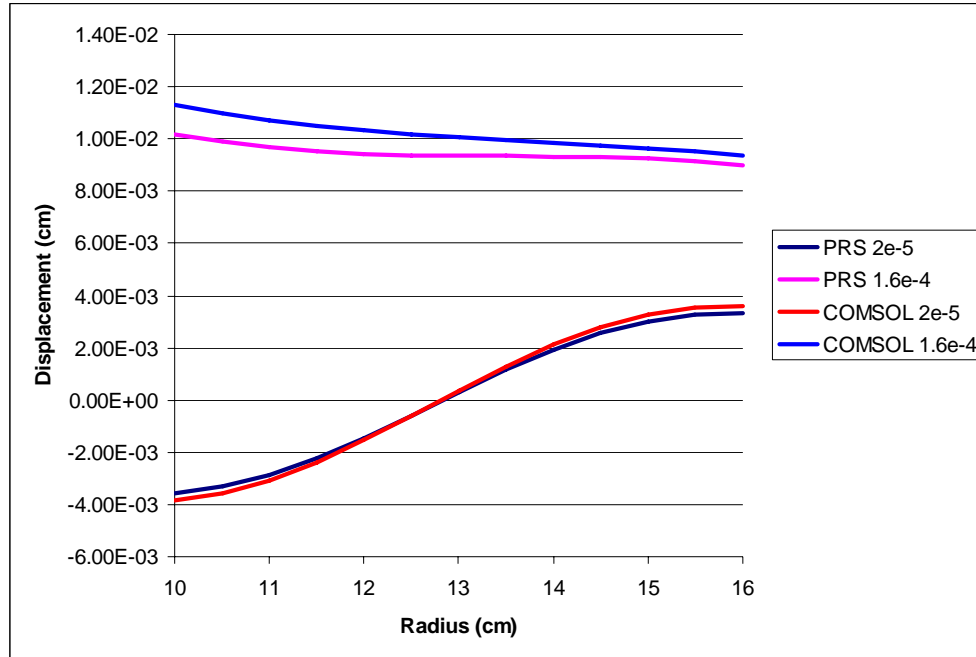


Figure 5.8: Displacement profile comparison.

The displacement profiles in Figure 4.8 show that PRS and COMSOL predict very similar displacement values as long as errors associated with grid spacing and time step size are minimized. The coupled PRS program will have separate grid structures for the neutronics and mechanics modules. The grid structures will remain separate for two reasons. The radial spacing of the mechanics module must be large enough to model the

propagation of the fastest waves, as shown above in Figure 5.3. Secondly, the axial spacing must correspond to the height of each fuel plate.

PRS will assume that each plate has its own radial temperature profile. The time step size will not necessarily be the same for both the mechanics and neutronics modules. The mechanics module time step will be varied again when the modules are coupled to determine how much energy can be deposited in each time step.

Chapter 6: SPR Pulse Simulation

Data from the SPR III reactor will be presented and compared to results from PRS simulations. The SPR III reactor core had a fuel height of 36.83 cm, an inner radius of 8.89 cm, an outer radius of 14.86 cm, and fuel plates that were 2.019 cm thick. The SPR III reactor criticality ranged from \$3.50 subcritical with all reflectors down, to in excess of 10 cents super prompt critical during pulses. Information about the SPR III reactor and data characterizing its pulses were found in its safety analysis report (Ford, 2003). The full width at half maximum (FWHM), and maximum temperature from pulses with a range of initial prompt reactivities is shown below in table 6.1.

Table 6.1. FWHM and maximum temperature for pulses with varying initial reactivity (Ford, 2003).

| Prompt Reactivity (cents) | FWHM (μ s) | T (C) |
|---------------------------|-----------------|-------|
| 4.5 | 205 | 100 |
| 6.5 | 150 | 150 |
| 7.7 | 119 | 200 |
| 8.8 | 100 | 250 |
| 9.8 | 85 | 300 |
| 10.7 | 81 | 350 |
| 11.6 | 77 | 400 |
| 12.6 | 74 | 450 |
| 13.4 | 71 | 500 |

As the pulse reactivity increases the pulses become shorter and the maximum assembly temperature rises. Maximum pulse power is much higher for pulses with larger reactivities because these pulses deposit more heat into the assembly in less time. The time step size of a simulation must vary to accurately simulate such sharp pulses without requiring excessive amounts of computational time. If time steps are too large the pulse energy will be severely over predicted. Measurements of the expansion of several fuel plates at the outer radius are shown in Figure 6.1 for a pulse with a 50 μ s FWHM, causing a 500 $^{\circ}$ C temperature increase.

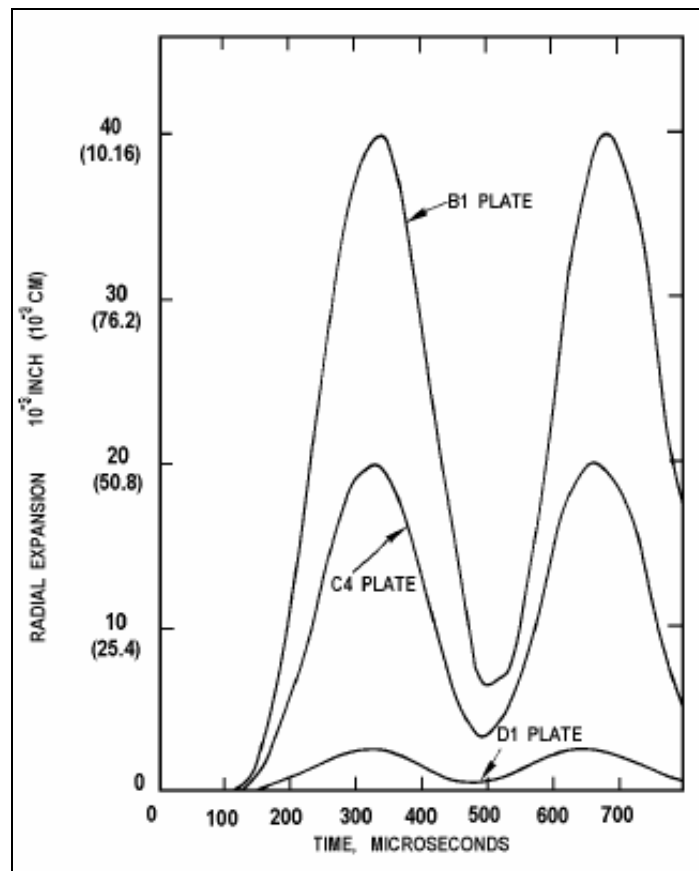


Figure 6.1: Outer radius expansion during a pulse with a 50 μ s FWHM (Ford, 2003).

Expansion of the outer radius, of the plate nearest to the center of the assembly, (B1), oscillates between 0.04 cm and 0.013 cm with a period of roughly 500 μ s. Some of the displacement information from the safety analysis report does not include mention of any other parameters describing the pulse during which the data was recorded. Inner and outer radius fuel plate expansion values are shown in Figure 6.2 for a typical SPR III pulse.

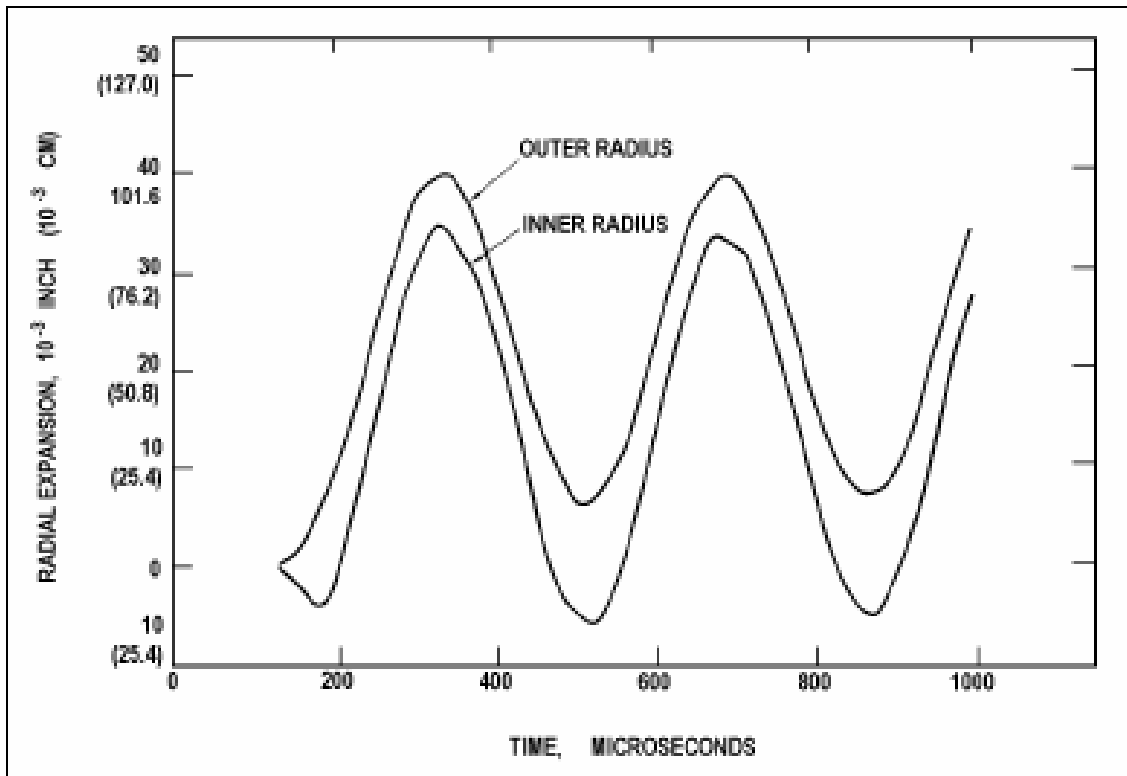


Figure 6.2: Inner and outer radius fuel plate expansion during a typical pulse (Ford, 2003).

The inner radius initially contracts, as seen in earlier mechanics module benchmarking. It is also important to note that oscillation amplitude does not decrease noticeably after the first 800 μs . Constant amplitude oscillations indicate that energy losses due to plastic deformation and friction between plates are small. The mechanics equation used to model SPR pulses assumed only elastic deformation and negligible energy losses from friction between plates. The fuel plate displacement values oscillate between -5×10^{-3} cm and 35×10^{-3} cm. Figure 6.3 shows the inner and outer radius tangential stress values that were calculated for a SPR reactor pulse.

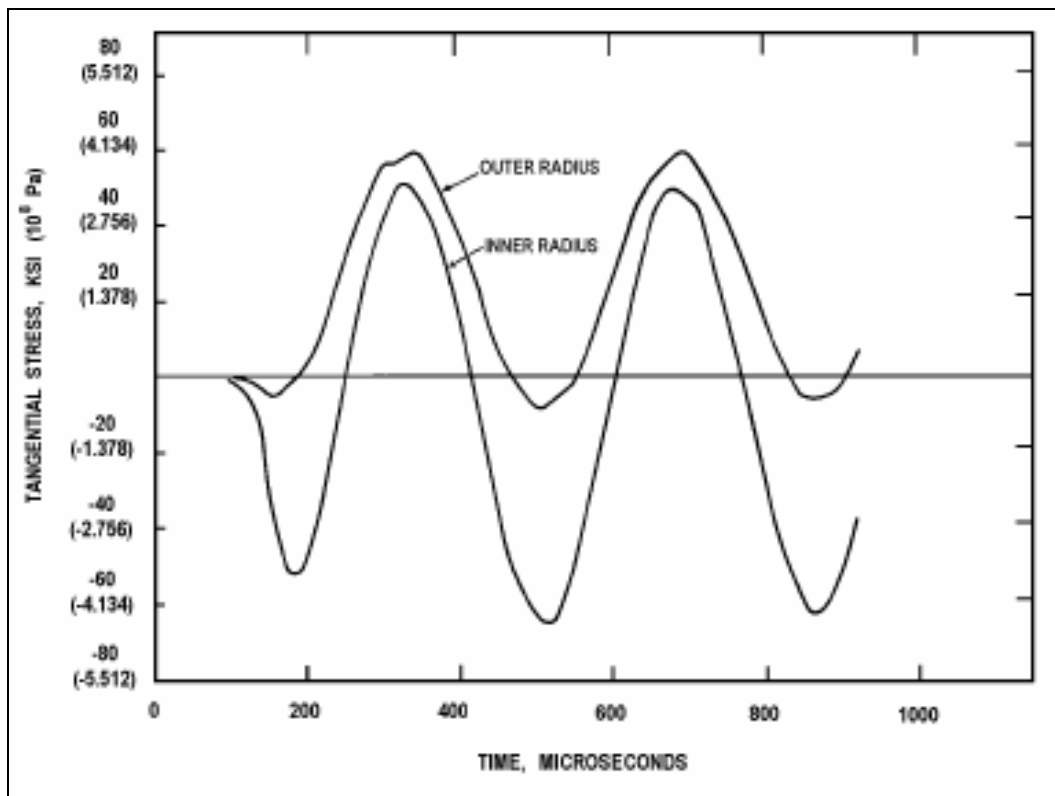


Figure 6.3: Inner and outer radius tangential stress values (Ford, 2003).

The tangential stress values range from 6 GPa to -7 GPa. Since stress values are directly proportional to displacement, stress oscillations will occur at the same frequency as displacement oscillations. It must be noted that stresses present during and immediately following pulses can exceed the static yield stress of the fuel at room temperature without plastically deforming the fuel. The maximum dynamic yield stress for the fuel exceeds the static yield stress.

PRS simulated a SPR III pulse with an initial prompt reactivity of 4.5 cents. The outer radius of the PRS simulation was changed from 14.86 cm to 15.13485 cm in order to produce a prompt reactivity of 4.5 cents, in lieu of reflectors. The PRS simulation used 1 group cross sections to reduce the computational time required. If the pulse simulations are excessively influenced by the change in assembly dimensions required to produce the correct criticality with 1 group, additional groups may be added to improve the criticality prediction and reduce the size of the assembly dimension adjustments. It is best to begin simulations with fewer groups to reduce computational times. The initial goal of the pulse simulations is to prove the functionality of the original deterministic neutron transport modeling methods, and show that the coupled partial differential equations approach to modeling pulses can produce data that is qualitatively correct and quantitatively correct within an order of magnitude.

The coupling of the three PRS modules was challenging despite the fact that each module performed quite well during isolated benchmarking trials. If the time step sizes in the mechanics module are too large, it will produce expansion values that are far too small, and pulse power will rise beyond what it should. Similarly, if neutron time step sizes are too small, PRS will predict a much larger pulse than it should. The neutron time

step multiplication parameter was used to adjust the step size used in the neutronics module. The neutron time step parameter would be multiplied by the smallest neutron lifetime to adjust the neutronics module time step size. A maximum energy deposition limit per time step was used to adjust the mechanics module time step. Figure 6.4 shows the pulse power as a function of time for several 4.5 cent SPR simulations in PRS with different mechanics module time step values.

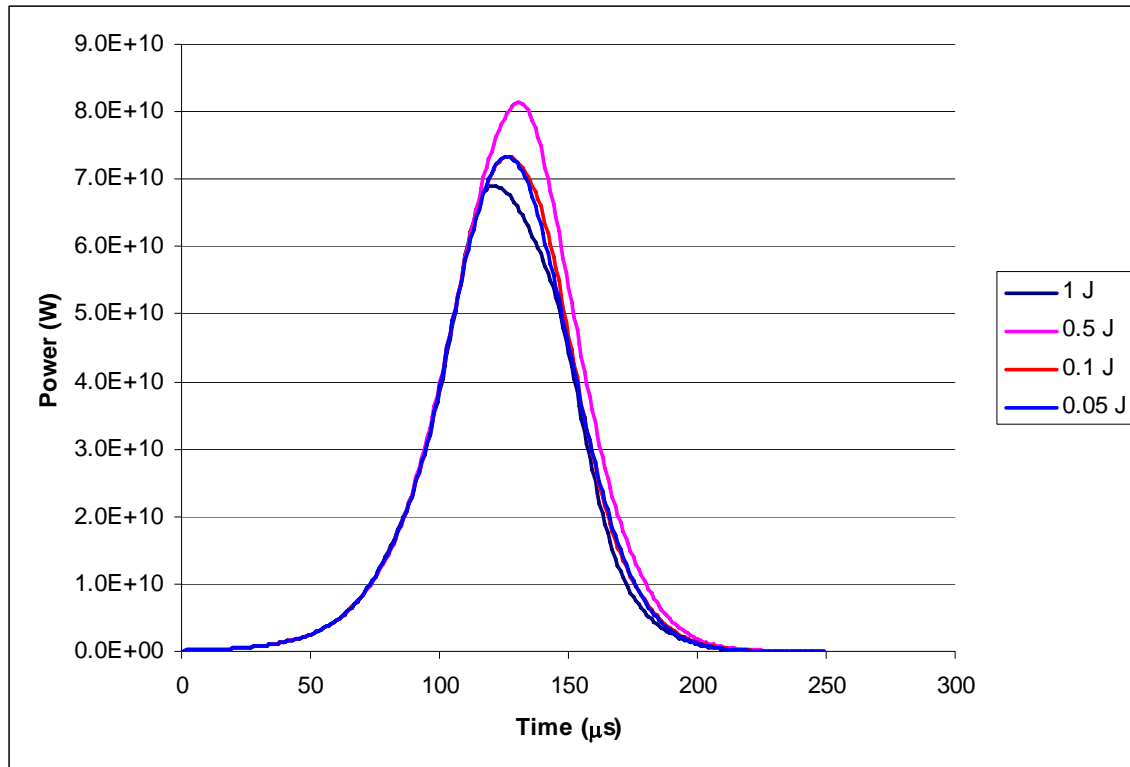


Figure 6.4: 4.5 cent pulse simulations with various mechanics energy deposition limits.

The neutron time step multiplication factor used in Figure 6.4 was 0.25, and the energy deposition per time step ranged from 1 to 0.05 J per mechanics time step. The

pulse shape reached convergence at an energy deposition per time step value of 0.1. PRS pulse simulations with mechanics modules operating with larger time step sizes will either over or underestimate the pulse power. Once the correct size for the mechanics module time step was found, the neutronics module time step was varied to find the largest possible value that would yield the correct pulse shape. Figure 6.5 shows the pulse power as a function of time for several 4.5 cent SPR simulations in PRS with different neutronics module time step values.

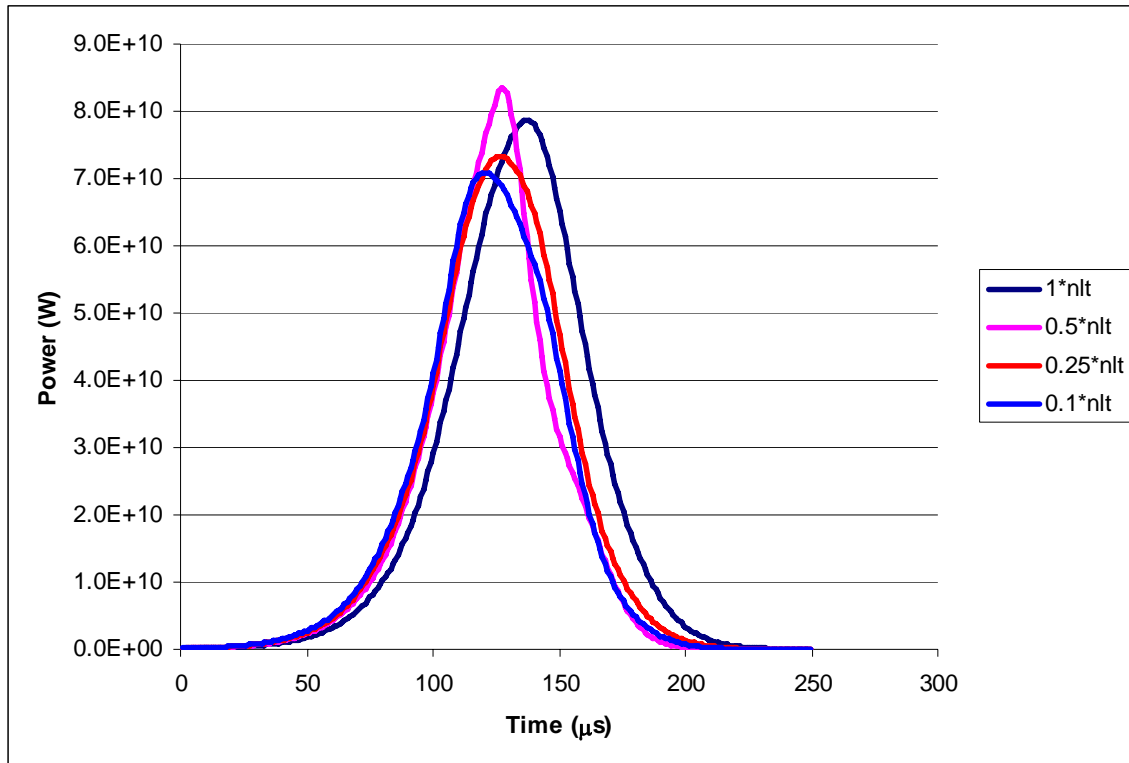


Figure 6.5: 4.5 cent pulse simulations with various neutronics time step sizes.

The neutronics module time step values ranged from the average neutron lifetime in the reactor to one tenth of the average neutron lifetime. One quarter of the average neutron lifetime was settled on as the neutronics module time step of choice. The total energy deposition from the “0.25*nlt” simulation differed from the “0.1*nlt” simulation by only 5 percent. The decision to choose “0.25*nlt” as the time step size was made to strike a balance between program usability and accuracy. If the program neutronics time step size were further reduced an increase in accuracy would be seen. However, the decreased time step size would make PRS require more than twice the computational time. PRS is more than capable of producing scoping calculations with order of magnitude accuracy with the time step sizes shown above. A complete listing of the simulation parameters is shown below. Appendix A describes how the input parameters relate to the PRS code.

- inner radius = 8.89 (cm)
- outer radius = varied (cm)
- height = 36.83 (cm)
- fuel plate thickness = 2.019 (cm)
- modulus of elasticity = 82 (GPa)
- poisson’s ratio = 0.38 (-)
- uranium density = 19.05 (g cm⁻³)
- molybdenum density = 10.28 (g cm⁻³)
- coefficient of thermal expansion = 4.8x10⁻⁶ (K⁻¹)
- source type = 0 (-)

- source height = 0 (cm)
- source neutrons = 0 (n)
- initial power = 10 (MW)
- thermal conductivity = 27 (W m⁻¹ K⁻¹)
- specific heat = 0 (J kg⁻¹ K⁻¹)
- enrichment = 1 (-)
- conduction = 0 (-)
- simulation type = 0 (-)
- tolerance = 0 (cents)
- simulation length = 6x10⁻⁴ (s)
- data output frequency = 1x10⁻⁶ (s)
- time step multiplication factor = 0.25 (-)
- grid spacing multiplication factor = 1 (-)
- number of groups = 1 (-)

The SPR pulse simulations discussed within this chapter should take roughly 12 to 15 hours to run on a modern desktop computer. Pulses that deposit larger amounts of energy into the fuel require smaller time steps in the mechanics module to accurately simulate the fuel expansion. However, larger pulses also have shorter FWHM values, so larger initial reactivities do not necessarily cause longer pulse simulation run times. If a parameter is not needed for a simulation the user must enter zero in its field. If the

specific heat field marked zero, PRS uses equation 6-1 to calculate specific heat values (Wilkinson, 1962).

$$c_p = 0.118526 * T + 104.698320 \quad (6-1)$$

Here T is in (C) and c_p is in ($\text{J kg}^{-1} \text{K}^{-1}$). It is important to list all the simulation parameters because an incorrect value in one of the modules will affect all of the results. Figure 6.6 shows the pulse power plot from the PRS simulation of a 4.5 cent pulse with the parameters listed above.

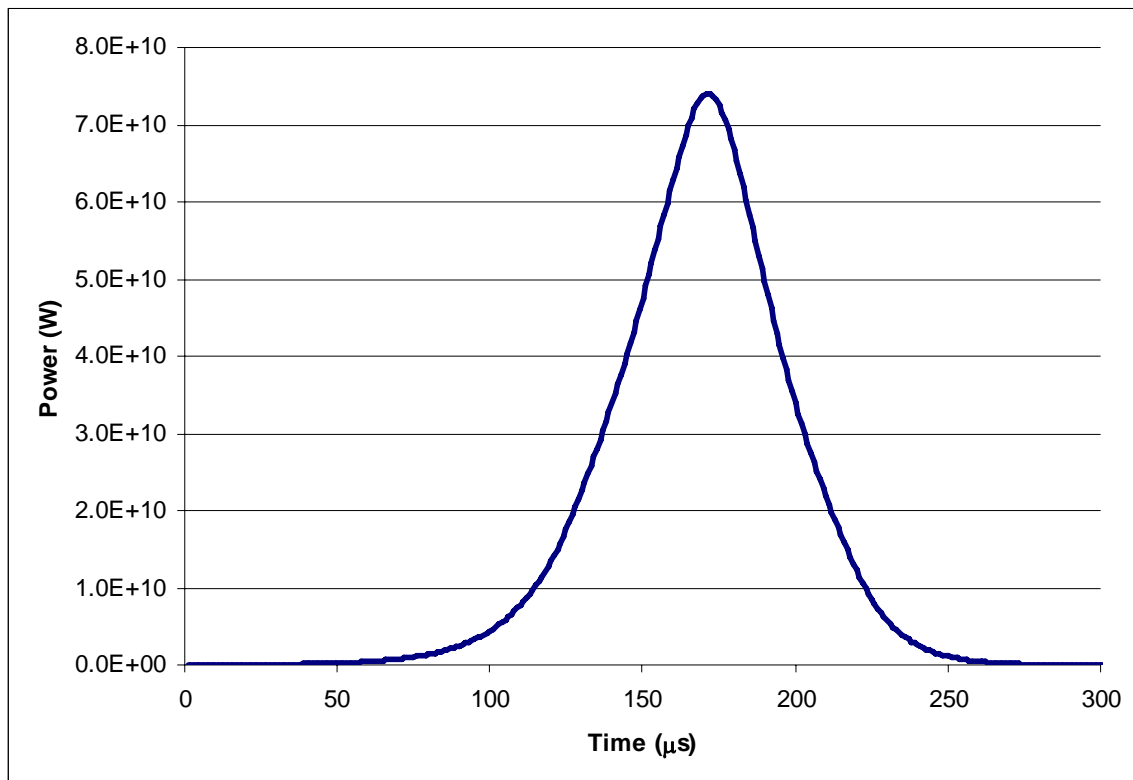


Figure 6.7: Pulse power plot from a PRS simulation of a SPR reactor pulse with an initial prompt reactivity of 4.5 cents.

The FWHM value of the pulse shown above was $56\ \mu\text{s}$ and the pulse ended after roughly $250\ \mu\text{s}$. The fuel plate expansion behavior changed noticeably after the pulse had finished. Figure 6.7 shows the inner and outer radius displacement values that follow a 4.5 cent pulse.

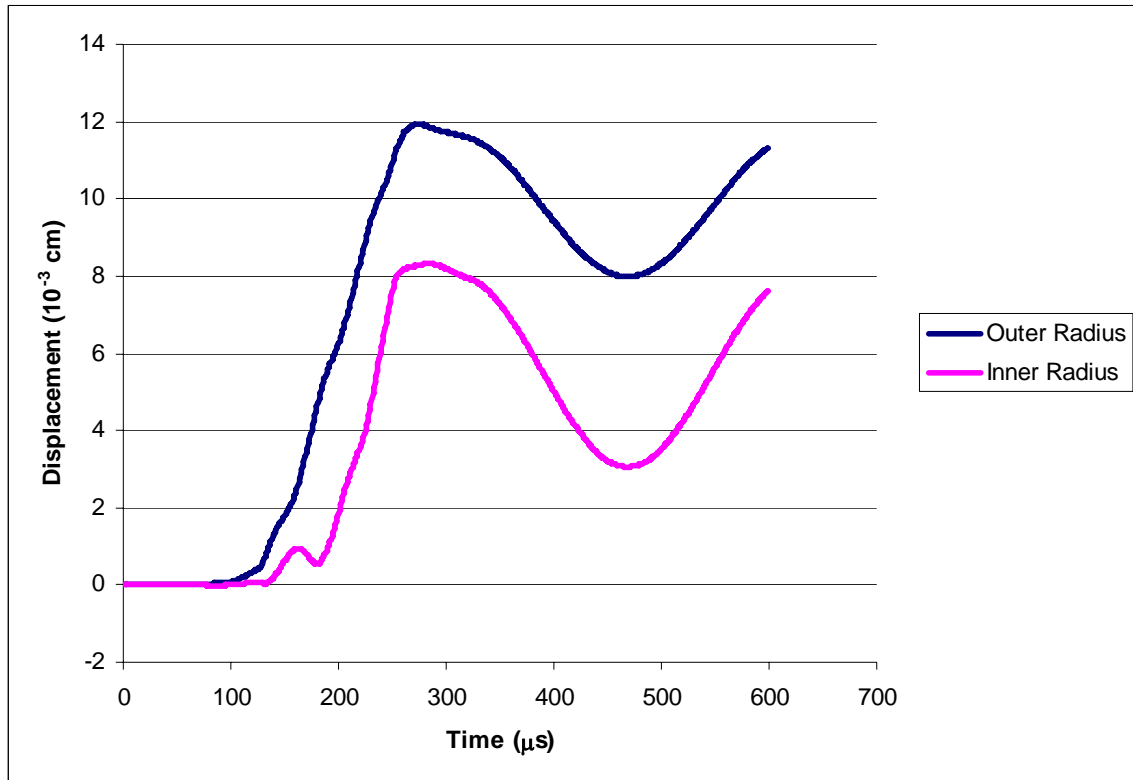


Figure 6.7: Inner and outer radius expansion following a 4.5 cent pulse.

Fuel plate displacement ramped up, peaked shortly after the ended due to inertial effects, and finally began to oscillate after roughly 300 μs . The displacement values from the 4.5 cent pulse are smaller than those given for a “typical” SPR reactor pulse. However, if the “typical” pulse is somewhere between the minimum and maximum listed pulse values, the 4.5 cent pulse displacement values should be smaller than the typical SPR pulse values. PRS predicted that the pulse would cause a 124 K temperature rise, a total sample cavity fluence of 1.36×10^{14} (n cm^{-2}). The 4.5 cent pulse deposited 4.7 MJ of energy into the assembly. Figure 6.8 shows the inner and outer tangential stress values following a 4.5 cent SPR pulse.

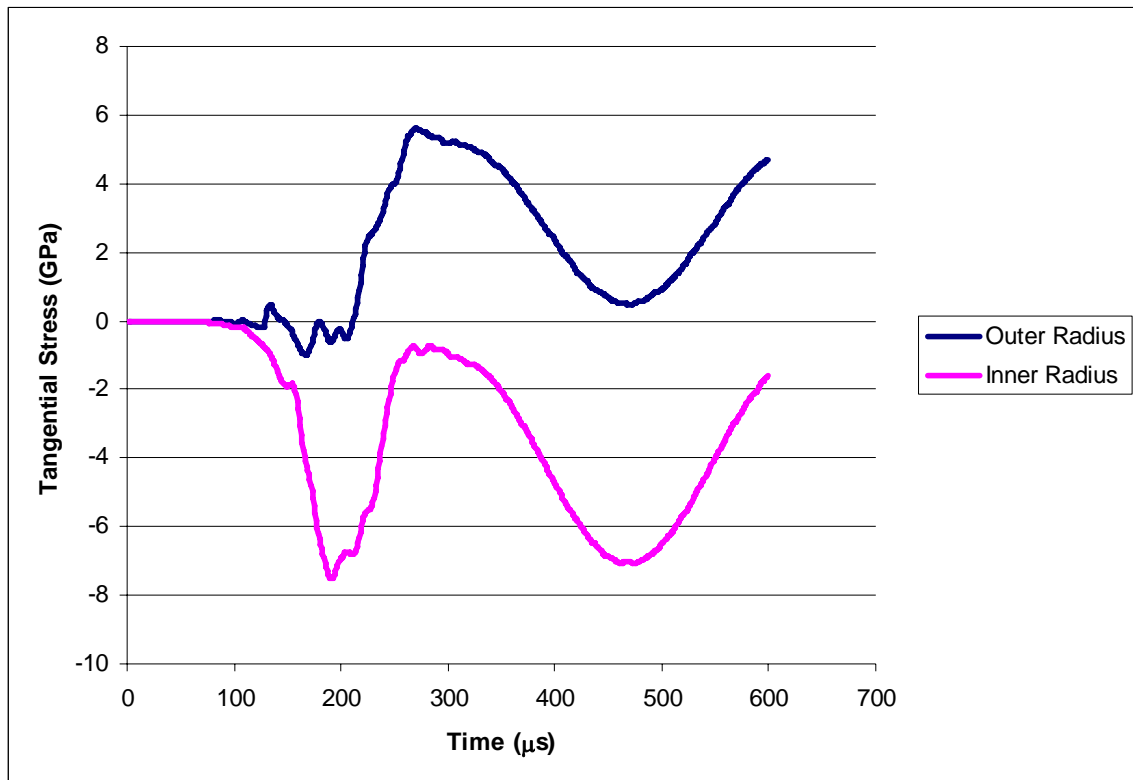


Figure 6.8: Inner and outer radius tangential stress following a 4.5 cent pulse.

The shape of the tangential stress oscillations mirror the radial expansion oscillations as one would expect. There is a clear difference in reactor behavior before and after the 300 μ s mark due to the pulse and the subsequent inertial effects. PRS tangential stress values oscillate between 6 GPa and -8 GPa. Tangential stress values are much closer to the “typical” SPR pulse data than the displacement values despite the fact that they should be roughly proportional. This difference may be attributed to the fact that PRS simulations do not account for the segmentation of each fuel plate into four pieces. It is unlikely that ZEDNA reactors will generate the large fuel plate stress values encountered by SPR reactors. As a result it is not clear if the segmentation of each fuel plate into four pieces will be necessary in their designs. Figure 6.9 shows the pulse power plot from the PRS simulation of a 13.4 cent pulse.

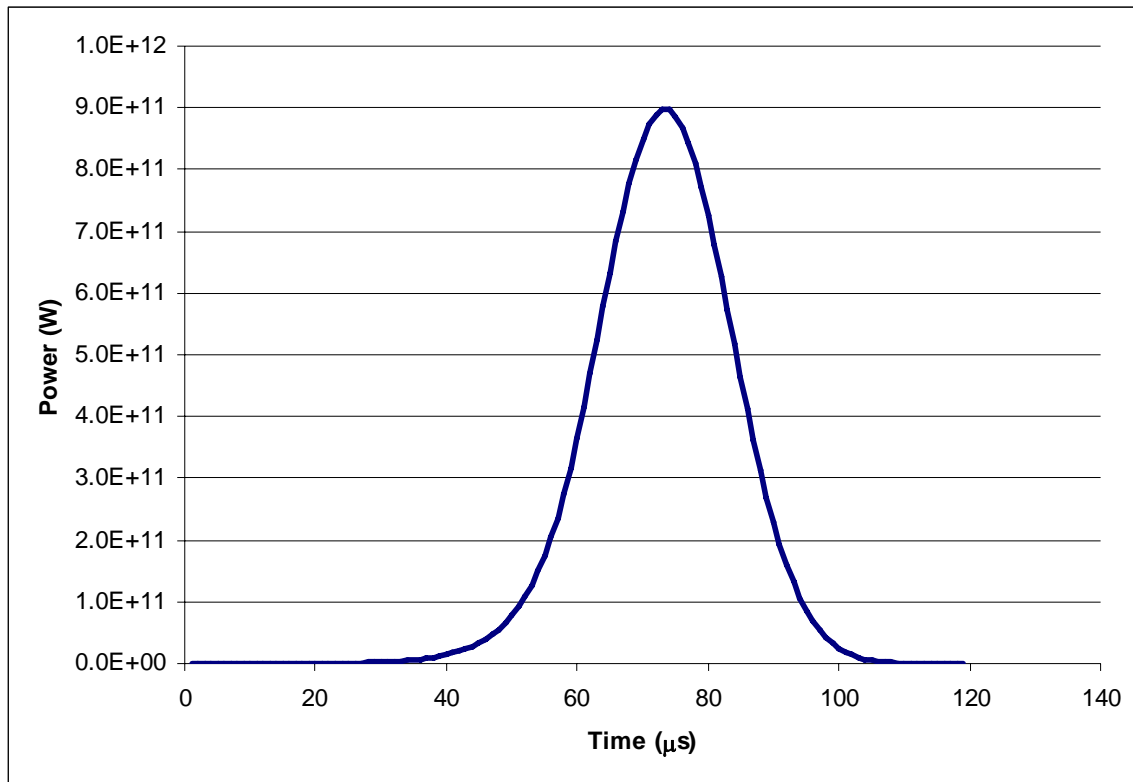


Figure 6.9: Pulse power plot from a PRS simulation of a SPR reactor pulse with an initial prompt reactivity of 13.4 cents.

The FWHM value of the pulse shown above was 23 μs and the pulse ended after roughly 110 μs . One would expect a larger initial reactivity to lead to a shorter more powerful reactor pulse. Once again, the fuel plate expansion behavior changed noticeably after the pulse had finished. Figure 6.10 shows the inner and outer radius displacement values that follow a 13.4 cent pulse.

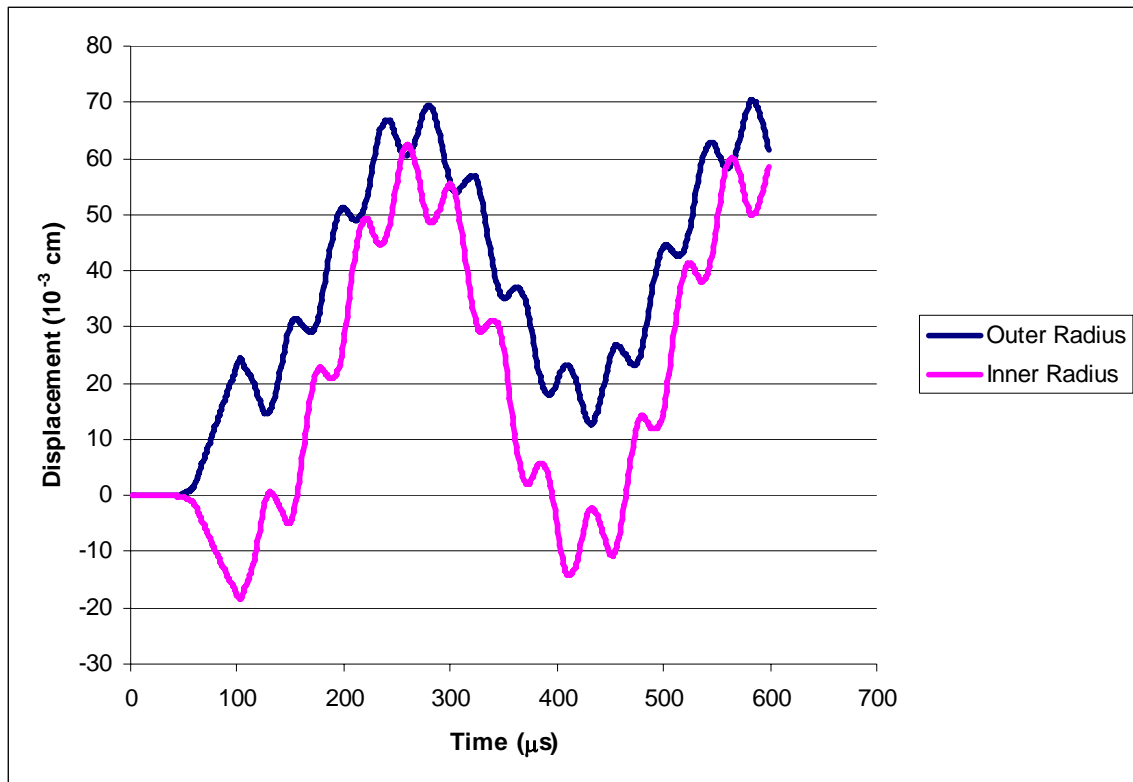


Figure 6.10: Inner and outer radius expansion following 13.4 cent pulse.

The change in fuel plate expansion after the pulse dies out is even more noticeable in the 13.4 cent pulse simulation. The outer radius displacement values from the 13.4 cent pulse oscillate between 0.07 and 0.01 cm. PRS predicted that the pulse would cause a 508 K temperature rise, a total sample cavity fluence of 6.65×10^{14} (n cm⁻²). The 13.4 cent pulse deposited 22.9 MJ of energy into the assembly. Figure 6.11 shows the inner and outer tangential stress values following a 13.4 cent SPR pulse.

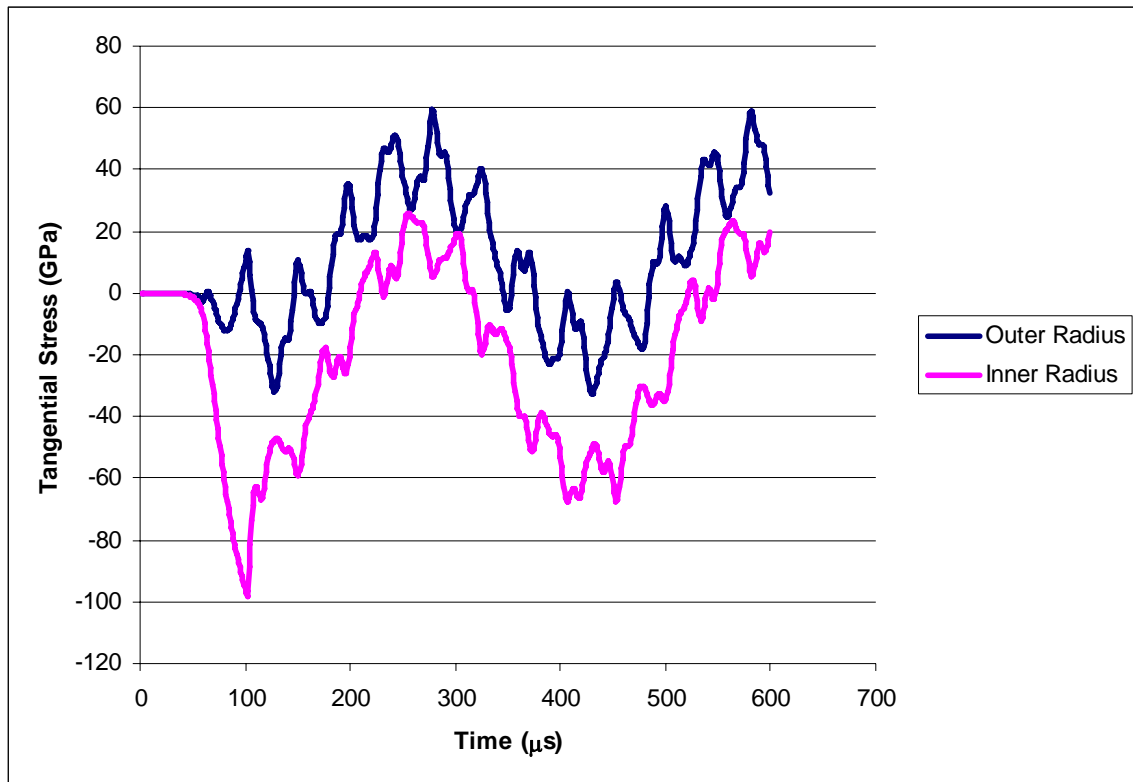


Figure 6.11: Inner and outer radius tangential stress following 13.4 cent pulse.

Once again, the tangential stress values closely mirror the displacement value trends. Stress values at the outer and inner radii oscillate between 60 and -100 GPa. It is interesting to note that a tremendous amount of stress induced at the inner radius at the beginning of the pulse due to the initial contraction of the inner radius surface toward the center of the sample cavity. Table 6.2 summarizes and compares some of the critical pulse parameters from the PRS simulations and the SPR experimental data.

Table 6.2. Critical pulse parameters from PRS and SPR experimental data (Ford, 2003).

| | | | |
|--|-----------------------|-----------------------|-----------------------|
| Prompt Reactivity (cents) | 4.5 | 9.8 | 13.4 |
| SPR FWHM (μs) | 205 | 85 | 71 |
| PRS FWHM (μs) | 56 | 28 | 23 |
| SPR ΔT (C) | 100 | 300 | 500 |
| PRS ΔT (C) | 124 | 321 | 508 |
| SPR Max. Disp. (10^{-3} cm) | 40 | | |
| PRS Max. Disp. (10^{-3} cm) | 11.9 | 35.5 | 70.4 |
| PRS Sample Cavity Fluence (n cm^{-2}) | 1.36×10^{14} | 3.86×10^{14} | 6.65×10^{14} |
| Fission Energy (MJ) | 4.7 | 13.3 | 22.9 |

PRS appears to be well within the qualitatively correct and quantitatively order of magnitude correct initial goals set at the beginning of this research. PRS temperature rise data agrees much more closely with experimental SPR data as the initial prompt reactivity of the pulses increases. It is unclear whether this reduction in error is the result of an unknown numerical simulation event, or if is due to an increased ability to measure larger changes in temperature with the experimental apparatus.

Improvements the agreement between PRS and SPR experimental FWHM values could be seen if axial displacement were accounted within the mechanics module. In the current module all of the deposited energy drives the radial expansion, which lowers assembly density and shuts off the reactor pulse. If axial expansion were accounted for the fission energy would drive both axial and radial expansion. Axial expansion would serve to close the gaps between successive fuel plates without lowering the net assembly

density. The amount of radial expansion per unit energy deposited into the assembly would be lowered and pulse widths would increase.

With the PRS benchmark comparisons of SPR reactor pulses complete we may now move on to ZEDNA reactor simulations. Plots of ZEDNA reactor power during pulses should be quite dissimilar to the SPR reactor data because they begin operation in a sub prompt critical state.

Chapter 7: ZEDNA Pulse Simulation

The reactor dimensions used in the ZEDNA calculations were chosen to bolster the external neutron source as much as possible while still allowing for sufficient sample cavity volume. Ideally the neutron source should be as close as possible to the assembly so fewer neutrons are lost to the surroundings. Additionally, smaller sample cavity sizes allow for higher fluence values given equal initial reactivity values. The simulated ZEDNA assembly has an initial reactivity of -15.38 cents (k_{eff} of 0.999) with prompt neutrons only. A complete listing of the simulation parameters is shown below.

- inner radius = 5 (cm)
- outer radius = 22.2218 (cm)
- height = 35 (cm)
- fuel plate thickness = 2.019 (cm)
- modulus of elasticity = 82 (GPa)
- poisson's ratio = 0.38 (-)
- uranium density = 19.05 (g cm⁻³)
- molybdenum density = 10.28 (g cm⁻³)
- coefficient of thermal expansion = 4.8x10⁻⁶ (K⁻¹)
- source type = 2 (-)
- source height = 5 (cm)

- source neutrons = 10^{13} (n)
- initial power = 0 (MW)
- thermal conductivity = 27 (W m⁻¹ K⁻¹)
- specific heat = 0 (J kg⁻¹ K⁻¹)
- enrichment = 0 (-)
- conduction = 0 (-)
- simulation type = 0 (-)
- tolerance = 0 (cents)
- simulation length = 10^{-4} (s)
- data output frequency = 10^{-6} (s)
- time step multiplication factor = 1 (-)
- grid spacing multiplication factor = 1 (-)
- number of groups = 1 (-)

The number of energy groups specified above does not include the external neutron source group. Time step multiplication factors below 1 are not recommended for ZEDNA simulations because very short the minimum neutron lifetime of the external source group causes the default time step to be much smaller than the average neutron lifetime. Figure 7.1 shows the assembly power in the first 100 μ s of the pulse.

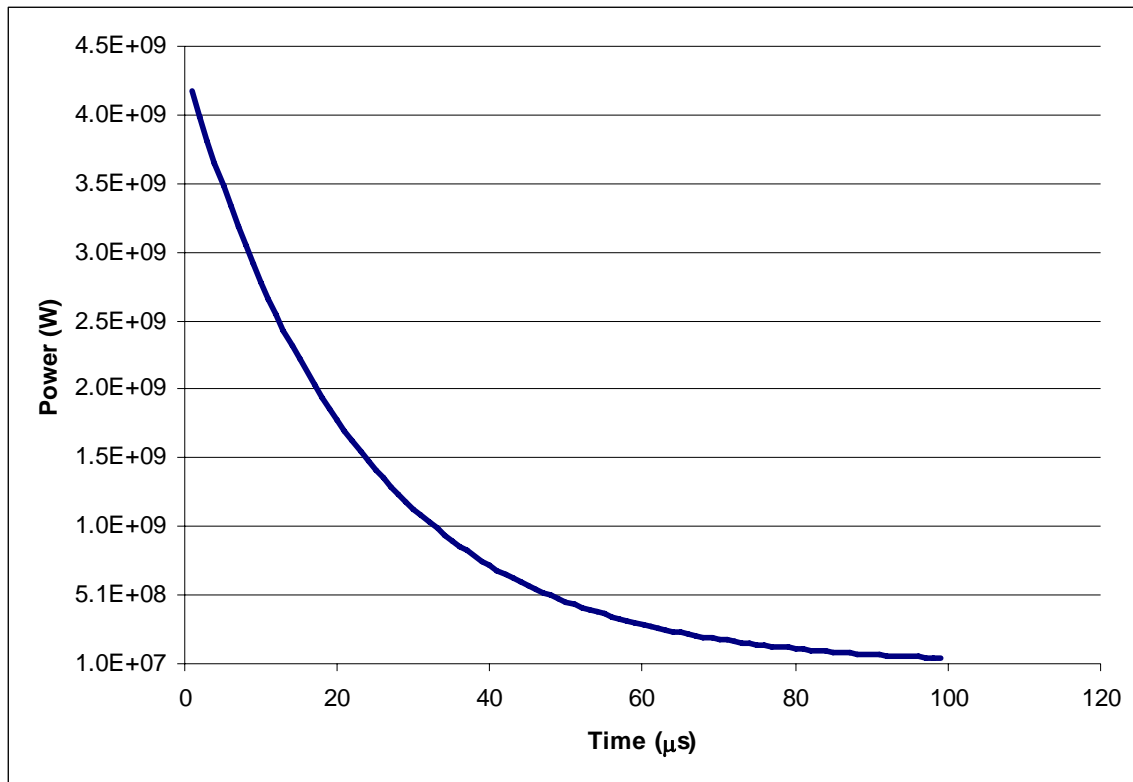


Figure 7.1: ZEDNA pulse power with a source size of 10^{13} neutrons.

The ZEDNA pulse power for a source size of 10^{13} neutrons is orders of magnitude lower than the power levels generated by small SPR pulses. The pulse power begins at its peak due to the fact that the assembly is sub-prompt critical. The rate of decay would be smaller if the assembly were closer to a k_{eff} value of 1. Figure 7.2 shows the maximum assembly temperature throughout the pulse.

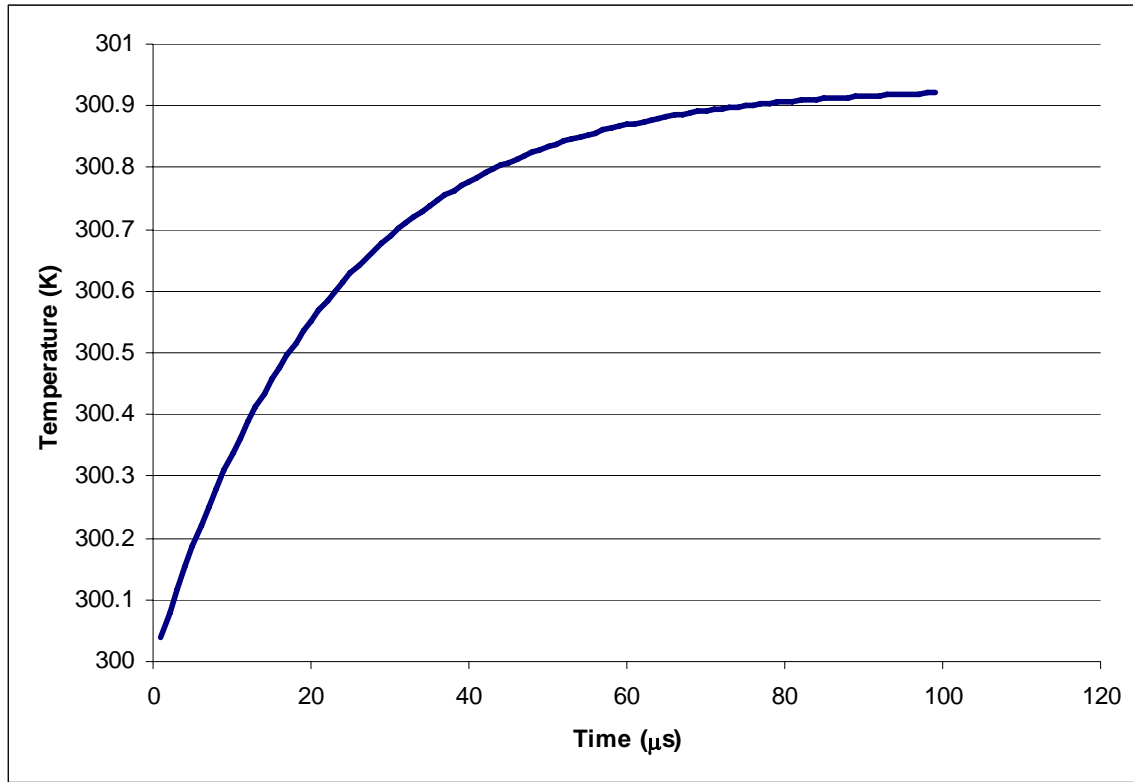


Figure 7.2: Maximum assembly temperature throughout the ZEDNA pulse with a source size of 10^{13} neutrons.

PRS predicted that the pulse would cause a 0.92 K temperature rise after 100 μ s. The asymptotic shape of the temperature plot suggests that the maximum temperature is unlikely to rise much further. The total fluence plot bears the same asymptotic shape and predicts a sample cavity fluence of 3.46×10^{12} (n cm^{-2}). Figure 7.3 shows the displacement at the inner and outer radii during the ZEDNA pulse with a source size of 10^{13} .

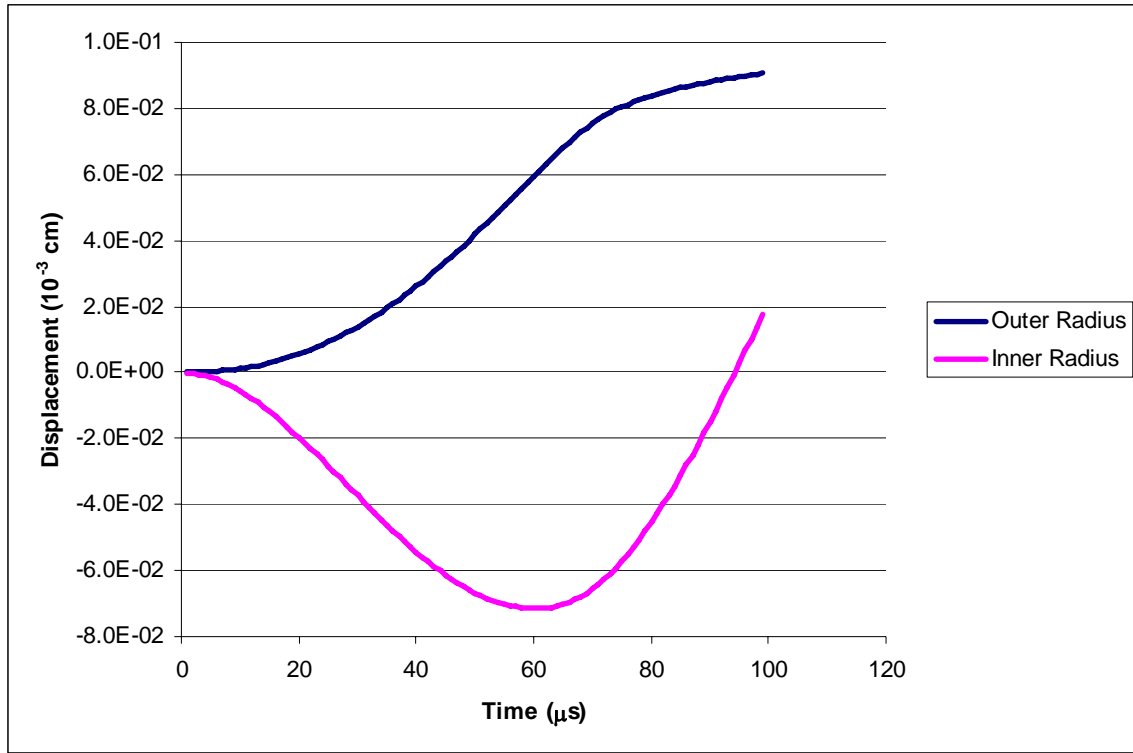


Figure 7.3: Inner and outer radius expansion following a pulse with a source size of 10^{13} neutrons.

Displacement values did not exceed 10^{-4} cm and appear unlikely to grow any further if the simulation lasted longer. Figure 7.4 shows the tangential stress at the inner and outer radii during the pulse with the source size of 10^{13} neutrons.

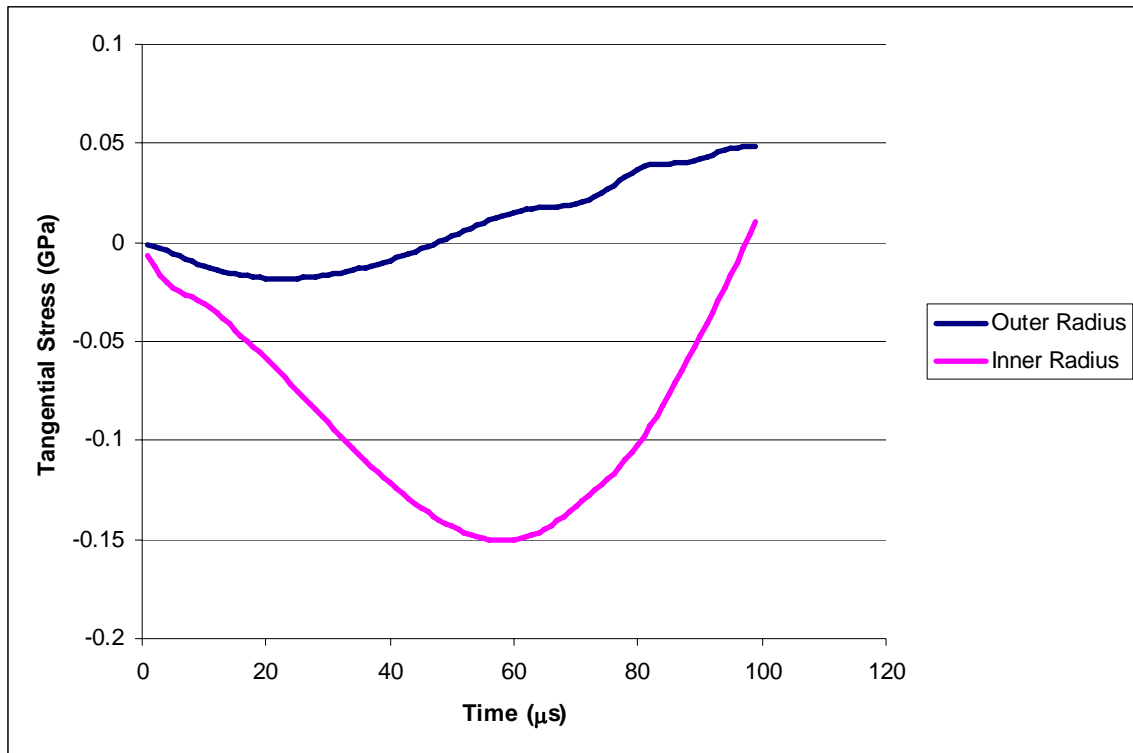


Figure 7.4: Inner and outer radius tangential stress following a pulse with a source size of 10^{13} neutrons.

Tangential stress values did not exceed 0.05 GPa. The first pulse simulation did not produce fluence values as large as the SPR pulses despite the large amount of sample cavity fluence. The change in reactivity due to fuel plate expansion in the PRS simulation was -0.12 cents. This minor change in reactivity means that the effect of the expansion was virtually negligible on the neutron transport within the assembly.

Should results scale linearly, an external source of 10^{15} would raise sample cavity fluence levels to the level seen during mid-sized SPR pulses. However, there are several variables that may be adjusted to alter sample cavity fluence.

Five additional ZEDNA simulations were created to test the sensitivity of sample cavity fluence to a range of variables. The first simulation increases the source size to 10^{15} neutrons to determine if a source of this magnitude will cause thermal expansion values large enough to affect the neutron transport process. The second simulation increases the initial assembly reactivity to -7.69 cents sub prompt critical. The third simulation increases the sample cavity radius to 10 cm and alters the outer radius to yield the original criticality of -15.38 cents sub prompt critical. The fourth simulation lowers the source height to 0.1cm above the assembly from 5 cm. Table 7.1 shows the pulse results from each of the simulations.

Table 7.1. Critical pulse parameters from PRS for several ZEDNA pulse simulations.

| Description | Small Source | Baseline | Increase Criticality | Wider Cavity | Closer Source |
|---|-----------------------|-----------------------|-----------------------|-----------------------|-----------------------|
| Source Size (n) | 10^{13} | 10^{15} | 10^{15} | 10^{15} | 10^{15} |
| Inner Radius (cm) | 5 | 5 | 5 | 10 | 5 |
| Outer Radius (cm) | 22.2218 | 22.2218 | 23.24885 | 29.42231 | 22.2218 |
| Height (cm) | 35 | 35 | 35 | 35 | 35 |
| Source Height Above Assembly (cm) | 5 | 5 | 5 | 5 | 0.1 |
| Prompt Reactivity (cents) | -15.38 | -15.38 | -7.69 | -15.38 | -15.38 |
| ΔT (C) | 1 | 86 | 143 | 63 | 129 |
| Max. Disp. (10^{-3} cm) | 0.1 | 5.4 | 8.2 | 4.5 | 8.8 |
| Fission Energy (MJ) | 0.01 | 9.4 | 16.1 | 9.7 | 14.4 |
| Max. Tangential Stress (GPa) | 0.2 | 16.0 | 11.5 | 9.1 | 29.1 |
| Sample Cavity Fluence (n cm^{-2}) | 3.46×10^{12} | 3.38×10^{14} | 5.77×10^{14} | 2.03×10^{14} | 5.18×10^{14} |
| $\Delta \rho$ (cents) | 0.73 | 6.02 | 5.17 | 3.37 | 7.38 |

Table 7.1 shows how sensitive the sample cavity fluence is to each of the four parameters. Sensitivity analysis is important in the study of new reactors because it

allows engineers to determine which design allows for as many desirable characteristics as possible. PRS allows users to vary any of the crucial assembly parameters to find the best possible ZEDNA design given an accurate set of design goals and restrictions.

Fuel expansion present in the ZEDNA simulation with the smallest external source only changes the assembly criticality by less than 1 cent. A small change in criticality should be expected from the simulation because of the small amounts of stress and change in temperature.

When the source is increased by two orders of magnitude the assembly criticality decreases by 6 cents during the pulse due to thermal expansion. The affect of the larger change in criticality on the neutron transport is made clear by the non-linear increase in sample cavity fluence. If the thermo-mechanical expansion present in the simulation did not affect the neutron transport, the sample cavity fluence would grow by exactly two orders of magnitude from the first simulation to the second. Instead, the sample cavity fluence in the second simulation is 2.73 % smaller than the value predicted by a linear increase from the first simulation to the second.

Larger criticality values allow the assembly to boost the external neutron source more effectively because the neutron population within the assembly dies away more slowly. When the initial assembly criticality was raised from -15.48 cents to -7.69 cents prompt critical, sample cavity fluence was increased by 71 percent.

When the inner radius is increased the sample cavity fluence decreases from 3.38×10^{14} to 2.03×10^{14} (n cm⁻²). The outer radius of the assembly must be increased by over 7 cm to maintain the initial criticality present in the baseline simulation. The increases in inner and outer radii change the radial flux profile, moving the peak away

from the inner radius, and subsequently reducing the amount of sample cavity fluence. The large inner radius simulation has a smaller temperature rise than the second simulation despite having a larger amount of total energy deposition due to the larger amount of fuel.

Source proximity to the assembly has a large effect on all of the reactor pulse parameters. When the source was moved from 4.9 cm closer to the assembly the sample cavity fluence increased from 3.38×10^{14} to 5.18×10^{14} (n cm⁻²). As the source is brought closer to the assembly, more neutrons either pass through the sample cavity or are deposited into the assembly.

ZEDNA simulations with large neutron sources or criticality values close to 1 cause significant fuel plate expansion and result in a greater need to simulate these pulses with programs capable of coupling neutronics, heat transfer, and mechanics. Commercial neutron transport codes, such as MCNP, are unable to capture the coupling between neutron transport and thermo-mechanical expansion required to simulate these pulses.

Chapter 8: Conclusions

Several new solutions to neutron transport problems were presented in this research. A new type of diffusion equation boundary condition incorporating view factors was developed to allow the accurate prediction of re-entrant current to the inner radius boundary of hollow cylindrical assemblies. The boundary condition was shown to produce the correct radial flux profile shape and magnitude. These new inner radius current calculations were coupled with original neutron path length equations to produce an accurate method of sample cavity fluence approximation. This research has shown via direct comparison of boundary flux gradients with MCNP that these methods are capable of correctly calculating the net current at the inner radius.

Additionally, a modified first collision source term was created to allow diffusion theory to accurately model a highly anisotropic point or planar source of 14 MeV neutrons. The neutronics calculations were benchmarked with MCNP, an industry standard stochastic neutron transport code, and showed close agreement. The new deterministic neutron transport modeling methods were then coupled with heat transfer and mechanics equations. The coupled equations were used to exceed what is possible with MCNP, and solve the coupled neutron transport and thermo-mechanical equations governing reactor pulses. This new direct method of pulse simulation employed by the PRS program allows users to characterize several reactor pulse parameters without the

use of catchall temperature feedback coefficients used by less complex pulse simulation methods.

PRS is a versatile program, capable of modeling fast burst and externally driven reactor pulses and providing users with detailed information about important reactor parameters. PRS has been shown to produce pulse parameters similar to experimental SPR reactor pulse data without relying on empirically derived temperature feedback coefficients. The use of neutron diffusion and thermoelastic partial differential equations in lieu of the Nordheim-Fuchs equations produces a tremendous amount of information about the reactor during the pulse.

In addition to reactor power information, PRS provides assembly neutron flux, energy spectrum, temperature, stress, and expansion data. Information about the neutron energy spectrum and flux distribution is also used to calculate the fluence and neutron energy spectrum present within the sample cavity. Furthermore, because all of the data produced by PRS is the result of several coupled equations, error in any of the modules would manifest in all of the results. Consequently, PRS may be used in conjunction with limited experimental or simulated data to produce a more complete characterization of reactor pulses.

Significant effort was taken to make the PRS program as user-friendly as possible. Simulations can be run with the use of a graphical user interface and the wealth of information produced by simulations can be sifted through using the plotting program. The plotting program produces 2 and 3 dimensional plots or movies and stores the data used to make the graphics in spreadsheet and text files. A short user manual describing the graphical user interface and user input is provided in Appendix A.

Benchmark trials on the heat transfer and mechanics modules with the COMSOL program showed close agreement. As long as the time step sizes are sufficiently small, the mechanics program is capable replicating one dimensional time dependent elastic thermal expansion. Heat transfer benchmarking showed that conduction effects are only relevant in scenarios where the reactor thermal conductivity is large and pulses are in the ms timeframes.

The MCNP benchmarking showed that the diffusion equation can be used to model the highly anisotropic behavior of the ZEDNA external neutron source with the aid of the external source term. PRS correctly predicted the flux values in space and time that result from the ZEDNA neutron source given an assembly with the same criticality as MCNP. The unique inner radius boundary condition was also crucial to the accurate simulation of neutron transport within the fuel and in the sample cavity. Fluence calculations made in PRS matched very closely with the values produced in MCNP.

Comparison with experimental data from the SPR reactor showed that PRS can simulate pulses, using only one group, with sufficient accuracy. If PRS were parallelized and run on a bank of computers, SPR reactor pulses with many groups, a finer grid resolution, and a smaller time steps would yield an even more accurate results. However, other improvements could be made to PRS to make it more accurate, and still allow it to simulate pulses in a few hours on a desktop computer.

Addition of axial displacement to the mechanics module, without axial wave propagation or axial fuel plate movement would make the simulation more realistic. Pulse simulations would exhibit larger FWHM values, and reduced radial expansion. This odd, non-physical modification to the program would increase the authenticity of the

simulation, because it would replicate the axial displacement that SPR reactors undergo. As mentioned in section 2.4, the SPR and ZEDNA reactors are designed with gaps between fuel plates near the inner radius. Successive fuel plates contact each other only near the outer radius. Since the largest axial expansion occurs near the inner radius, a simulation where axial expansion is present, yet does not change the axial distance between plates, would be more accurate.

ZEDNA pulse simulations appear quite promising. With a ZEDNA source of a given size, PRS allows users to determine the reactor dimensions and source location necessary to produce the desired amount of sample cavity fluence. Sample cavity fluence calculations also account for external point source neutrons that pass through the sample cavity without interacting with the fuel.

In the future, PRS could be modified to model accident scenarios at commercial power reactors. A two dimensional section of a single fuel pin surrounded by water in a large reactor could be modeled with a symmetry boundary condition at the inner radius and white boundary conditions elsewhere. Additionally, the group structure would need to be much different.

The range of neutron energies simulated would begin much lower and not reach as high as 14 MeV. The accuracy of criticality predictions would likely increase despite much larger energy bin widths, due to the presence of hydrogen. Hydrogen would allow neutrons to lose much larger fractions of its kinetic energy in scattering interactions. However, the coupling between modules and the partial differential equations would not need significant changes.

Appendix A: PRS User Manual

A.1 PRS SETUP

The PRS program was created and compiled using MATLAB. The compiled version of the PRS program and the PRS plotting program will function on computers that do not have MATLAB installed. The PRS executables come with a file labeled `mcr_release14_automatic_installer.zip`; the installer inside this zip file should be run one time on any computer where the PRS executable is to be used. Once the MCRInstaller has been run the PRS executables can be run as many times as necessary.

A.2 POINT SOURCE SIMULATION

The PRS program can run in four different modes, point source simulation, planar source simulation, volume source simulation, and criticality calculation. The point and planar source simulations are designed to simulate ZEDNA pulses. The volume source simulation is meant to simulate SPR pulses. The criticality calculation can be used to determine the criticality of an assembly in order to compare simulation results with MCNP.

The PRS.exe file must be run in the same directory with the PRS.ctf file after the MCRInstaller program has been installed on your computer. The user should see the graphical user interface shown below when the PRS.exe file is run.

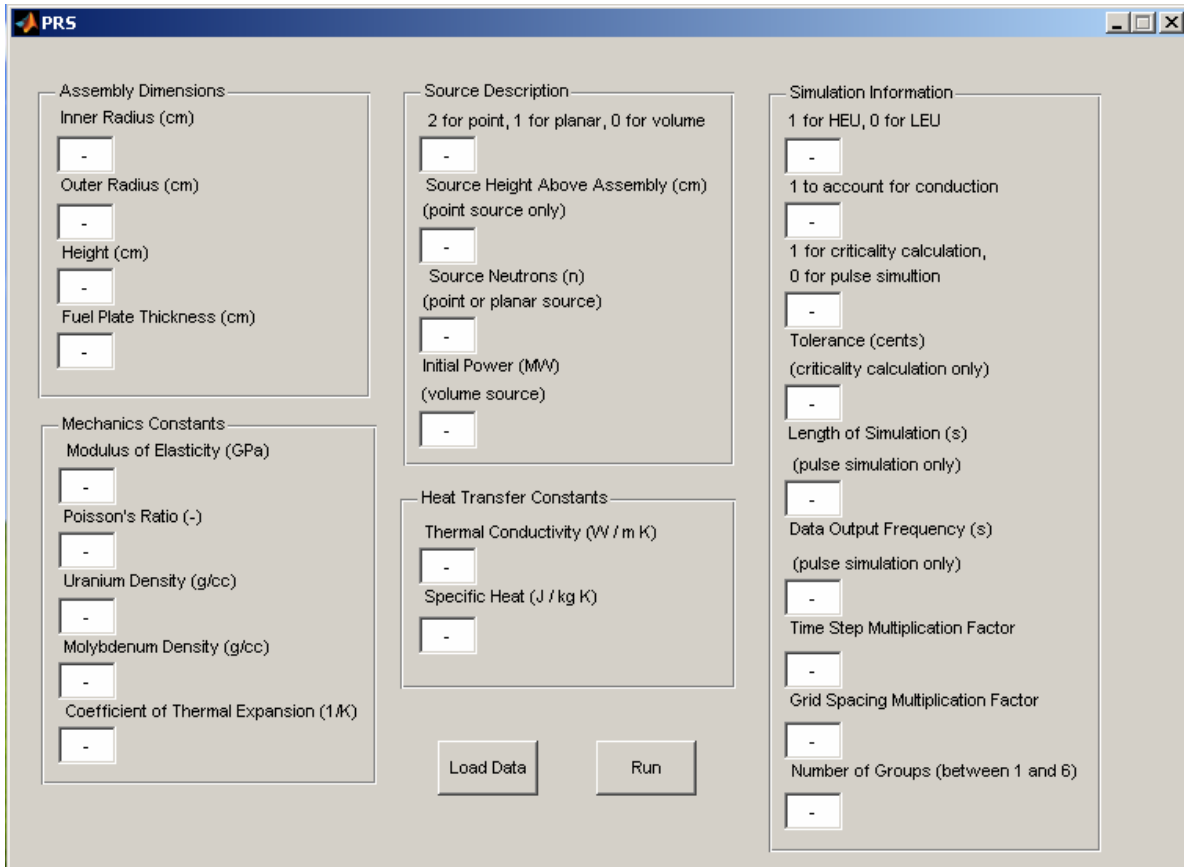


Figure A.1: Graphical user interface for the PRS program.

Information about the simulation is broken into five panels labeled, assembly dimensions, mechanics constants, source description, heat transfer constants, and simulation information. If the user has run a simulation before, in the same directory, and would like to run a new one with similar parameters, the user may press “Load Data” and parameters of the previous run will be loaded into the current simulation. Parameters of the current simulation will then appear in the command prompt window. The user may then make changes to the parameters by typing values in the appropriate boxes. If a user

has not yet run a simulation in the current directory the user must click on each box and either press enter or change the value in the box to the desired parameter for the simulation.

Point source simulations will use 22 out of the 24 available parameters. Any data input in the “Initial Power” or “Tolerance” fields will not be used. The values shown below can be used to reproduce the point source simulation described in Section 3.1 “First Test Scenario.”

- inner radius = 10 (cm)
- outer radius = 16 (cm)
- height = 30 (cm)
- fuel plate thickness = 2 (cm)
- modulus of elasticity = 82 (GPa)
- poisson’s ratio = 0.38 (-)
- uranium density = 19.05 (g cm⁻³)
- molybdenum density = 10.28 (g cm⁻³)
- coefficient of thermal expansion = 4.8x10⁻⁶ (K⁻¹)
- source type = 2 (-)
- source height = 5 (cm)
- source neutrons = 10¹⁵ (n)
- initial power = 0 (MW)
- thermal conductivity = 27 (W m⁻¹ K⁻¹)
- specific heat = 0 (J kg⁻¹ K⁻¹)

- enrichment = 1 (-)
- conduction = 0 (-)
- simulation type = 0 (-)
- tolerance = 0 (cents)
- simulation length = 10^{-7} (s)
- data output frequency = 0 (s)
- time step multiplication factor = 1 (-)
- grid spacing multiplication factor = 1 (-)
- number of groups = 6 (-)

The simulation should take roughly 5 minutes to run. If the specific heat field is left blank, PRS uses equation A-1 to calculate specific heat values (Wilkinson, 1962).

$$c_p = 0.118526 * T + 104.698320 \quad (\text{A-1})$$

Where T is in (C) and c_p is in ($\text{J kg}^{-1} \text{K}^{-1}$). If the data output frequency field is left blank, PRS will output data after each time step. In scenarios where the point or planar source is used, the assembly is made of HEU, and the time step multiplication factor is 1, the time step will be equal to 0.5 nanoseconds; the neutron lifetime of the 14 MeV neutrons.

The time step multiplication factor allows the user to adjust the time step size of simulations. The default time step size is the minimum neutron lifetime out of each of

the energy groups in the assembly. The grid spacing multiplication factor allows the user to adjust the grid resolution of the simulation. The default grid spacing is the minimum diffusion length out of each of the groups in the assembly.

Planar source simulations use 21 of the 24 available parameters. The “Source Height Above Assembly” “Tolerance” and “Initial Power” fields go unused in planar source simulations. Volume source simulations also require 21 parameters. The unused parameters in volume source simulations are “Source Height Above Assembly” “Tolerance” and “Source Neutrons.”

A.3 CRITICALITY CALCULATION

Criticality calculations require information from 11 of the 24 data fields in the PRS graphical user interface. The values shown below can be used to make a criticality calculation that should yield a k_{eff} value of 0.9590468.

- inner radius = 5 (cm)
- outer radius = 10.94 (cm)
- height = 30 (cm)
- fuel plate thickness = 2 (cm)
- modulus of elasticity = 0 (GPa)
- poisson's ratio = 0 (-)
- uranium density = 19.05 (g cm⁻³)
- molybdenum density = 10.28 (g cm⁻³)
- coefficient of thermal expansion = 0 (K⁻¹)

- source type = 0 (-)
- source height = 0 (cm)
- source neutrons = 0 (n)
- initial power = 0 (MW)
- thermal conductivity = 0 (W m⁻¹ K⁻¹)
- specific heat = 0 (J kg⁻¹ K⁻¹)
- enrichment = 1 (-)
- conduction = 0 (-)
- simulation type = 1 (-)
- tolerance = 0.01 (cents)
- simulation length = 0 (s)
- data output frequency = - (s)
- time step multiplication factor = 1 (-)
- grid spacing multiplication factor = 1 (-)
- number of groups = 1 (-)

The criticality calculation described above should take less than 1 minute to run. The k_{eff} value produced by MCNP for an identical simulation is 0.99075. Remember to use prompt fission neutron production values in MCNP if you attempt to verify the MCNP criticality calculation. Prompt fission neutron production values are invoked by using the “totnu no” command. The error of 3.20 % between MCNP and PRS will

decrease as the number of energy groups is increased, and the time step and grid spacing multiplication factors are decreased.

Criticality calculations in PRS must still solve the time dependant diffusion equation to properly model neutron transport. Time dependency must be accounted for because of the large effect of neutrons traversing the sample cavity. If the time dependency of the neutron transport model is removed and the k_{eff} value is not exactly equal to 1, the re-entrant flux will either be grossly over or underestimated. Due to the effect of the time step size on the criticality prediction, it is recommended that the user choose the same time step size in the criticality calculation and the subsequent pulse simulation.

A.4 PRS PLOTTER

Once a simulation has run, the PRSplotter executable may be used to view the results. The plotter program must have the associated .ctf file in the same directory along with all of the PRS executable output data. The graphical user interface for the PRSplotter is shown below.

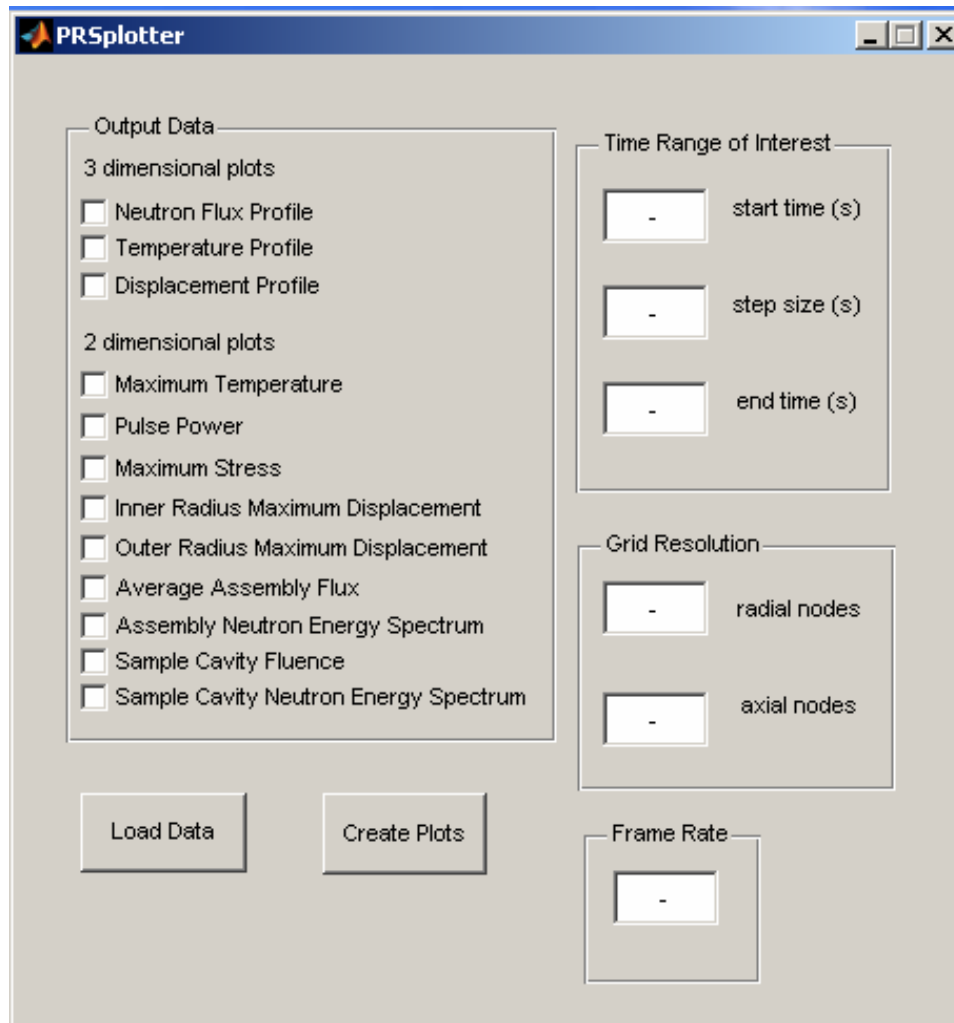


Figure A.2: Graphical user interface for the PRSplotter program.

There are four panels in the PRSplotter graphical user interface: Output Data, Time Range of Interest, Grid Resolution, and Frame Rate. In the “Time Range of Interest” panel the three fields allow the user to specify the pulse time from which information is desired. To find data at a certain point in time, enter the desired time in all three of the “Time Range of Interest” fields. If different values are placed in the three

fields, the plotter will create movies for 3 dimensional plots or plot a value over a range of times for the 2 dimensional plots.

The “Grid Resolution” panel allows the user to adjust the resolution of data produced for the 3 dimensional plots. If the user leaved the fields blank the program will use the same grid resolution as the PRS program. The “Frame Rate” allows the user to adjust the number of frames per s in the movies created by the plotter.

In order to produce plots the user must first click the “Load Data” button. The minimum and maximum simulation times will appear in the command prompt window along with the minimum step size. The simulation time values for the plotter are determined by the “Simulation Length” and “Data Output Frequency” values used in the simulation. Next, the user must click on one or several checkboxes in the “Output Data” panel to choose the type of plots or movies. The user then enters the appropriate values in the “Time Range of Interest” “Grid Resolution” and “Frame Rate” fields and clicks on the “Create Plots” button.

Plots are saved as either bitmap images or .avi files, depending on if they are movies or static images. Spreadsheets and text files are created to store the data from each plot that is produced.

References

- A. BEDFORD and K. M. LIECHTI, *Mechanics of Materials*. Prentice Hall Publishing, Upper Saddle, NJ, 2000.
- A. BEDFORD and W. FOWLER, *Engineering Mechanics Statics* 3rd Ed.. Prentice Hall Publishing, Upper Saddle, NJ, 2002.
- I. F. BRIESMEISTER, Ed., “MCNP –A General Monte Carlo N-Particle Transport Code, Version 4C,” LA-133709-M, Los Alamos National Laboratory, April 2000.
- R. L. BURDEN and J. D. FAIRES, *Numerical Analysis* 7th Ed.. Brooks and Cole, Belmont, CA, 2001.
- D. BURGREN, “Thermoelastic Dynamics of Rods, Thin Shells and Solid Spheres,” *Nuclear Science and Engineering*, Vol. 12, 203-217, 1962.
- A. BUSCHMAN, P. CLAUD, 1961, “Configuration Factors for Exchange of Radiant Energy Between Axisymmetrical Sections of Cylinders, Cones, and Hemispheres and their Bases,” NASA TN D-944.
- R. L. COATS, “The Sandia Booster Assembly (EDNA Program),” *Proc. National Topical Meeting on Fast Burst Reactors*, Albuquerque, NM, pp. 403-426, 1969.
- D. J. DORSEY, T. R. LOCKNER, R. L. COATS, “Pulse Neutron Source Alternatives to the Sandia Pulsed Reactor Facility,” SAND2005-5311, Sandia National Laboratory, Albuquerque, NM, August 2005.

- A. FEINGOLD, K. G. GUPTA, 1970, "New Analytical Approach to the Evaluation of Configuration Factors in Radiation from Spheres and Infinitely Long Cylinders," J. Heat Transfer, vol. 92, no.1, pp. 69-76, February.
- J. T. FORD, R. L. COATS, J. J. DAHL, S. A. WALKER, "Safety Analysis Report for the Sandia Pulsed Reactor Facility," SAND2003-2805, Sandia National Laboratories, Albuquerque, NM, December 2003.
- P. J. GRIFFIN, et al., "Design Trade-Off Study for a Large Volume Short Pulse Neutron Assembly," Proc. Pulse Reactor Workshop, Washington, D. C., November 13-17, 1994.
- D. E. GROCE, "Feasibility Study of an Accelerator-Booster, Fast, Pulsed Research Reactor – Neutron Yield Studies," GA-8087, Gulf General Atomic, Inc., San Diego, CA, June 1967.
- G.E. HANSEN, "Burst Characteristics Associated with the Slow Assembly of Fissionable Materials," LA-1441, Los Alamos National Laboratory, July 1952.
- D. L. HETRICK. Dynamics of Nuclear Reactors, University of Chicago Press, Chicago, 1971; reprinted by the American Nuclear Society, La Grange Park, IL, 1993.
- F. P. INCROPERA and D. P. DEWITT. Fundamentals of Heat and Mass Transfer 5th Ed.. John Wiley & Sons, New York, NY, 2002.
- E. KAUSEL. Fundamental Solutions in Elastodynamics. Cambridge University Press, New York, NY, 2006.
- J. LAMARSH and A. BARATTA. Introduction to Nuclear Engineering 3rd Ed.. Prentice Hall Publishing, Upper Saddle, NJ, 2001.

- J. R. LEE, et al., "Design Feasibility of an Externally Driven Nuclear Assembly (EDNA)," SAND89-1578, Sandia National Laboratory, Albuquerque, NM, May 1990.
- E. E. LEWIS and W. F. MILLER, Computational Methods of Neutron Transport. American Nuclear Society, La Grange Park, IL, 1993.
- H. LEUENBERGER, R. A. PERSON, 1956, "Compilation of Radiation Shape Factors for Cylindrical Assemblies," paper no. 56-A-144, ASME, November.
- R. E. MACFARLANE, and D. W. MUIR, "The NJOY Nuclear Data Processing System Version 91," LA-12740-M (October 1994).
- J. D. MILLER, "Thermomechanical Analysis Of Fast-Burst Reactors," Proceedings of the Topical Meeting on Physics, Safety, and Applications of Pulse Reactors, Washington D.C., November 13–17, 1994.
- A. F. MILLS. Heat Transfer 2nd Ed.. Prentice Hall Publishing, Upper Saddle, NJ, 1999.
- M. H. N. NARAGHI, B. T. F. CHUNG, 1982, "Radiation Configuration Between Disks and a class of Axisymmetric Bodies," J. Heat Transfer, vol. 104, no. 3, pp. 426-431, August.
- K. O. OTT and R. J. NEUHOLD. Introductory Nuclear Reactor Dynamics. American Nuclear Society, La Grange Park, IL, 1985.

- J. A. REUSCHER, "Thermomechanical Analysis of Fast Burst Reactors," Proc. of the National Topical Meeting on Fast-Burst Reactors, part of AEC Symposium Proc., CONF-690102, January 1969.
- J. A. REUSCHER, "Analysis of Internal Heating Shock Effects in Reactor Fuel Components," First International Conference on: Structural Mechanics in Reactor Technology, Berlin, September 20-24, 1971.
- J. A. REUSCHER, "In-Pile Testing of Fast-Burst Reactor Fuel Materials," AMC Research Reactor Symposium, White Sands Missile Range, New Mexico, February 20-21, 1973.
- Y. SAAD, Iterative Methods for Sparse Linear Systems 3rd Ed.. Society for Industrial and Applied Mathematics, Philadelphia, PA, 2003.
- W. M. STACEY, Nuclear Reactor Physics. John Wiley & Sons, New York, NY, 2001.
- W. D. WILKINSON, Uranium Metallurgy, Volume 2: Uranium Corrosion and Alloys, Interscience Publishers, New York, pp. 1184-1190, 1962.
- S.C. WILSON, "Development and Implementation of a Finite Element Solution of the Coupled Neutron Transport and Thermoelastic Equations Governing the Behavior of Small Nuclear Assemblies," Ph.D. Dissertation, University of Texas at Austin, Austin, TX 2006.
- T. F. WIMETT, et al., "Godiva II - An Unmoderated Pulse-Irradiation Reactor," Nuclear Science and Engineering, Vol. 8, pp. 691-708, 1960.
- T. F. WIMETT, "Dynamics and Power Prediction in Fission Bursts," Nuclear Science and Engineering, Vol. 110, pp. 209-236, 1992.

W. B. J. ZIMMERMAN. Multiphysics Modeling with Finite Element Methods. World Scientific, Hackensack, NJ, 2006.

Vita

Taylor Caldwell Green IV was born on July 17th, 1981 in Santa Cruz, Bolivia. Taylor is the son of Taylor Caldwell Green III and Maria Conceicao Green. Taylor Caldwell Green III was employed as a fluids engineer in Natal Brazil when he met his wife. The author has an older sister named Vicky Green who was born in Natal Brazil. Both the author and his sister were raised in Willis Texas from an early age.

The author graduated Willis High School in May of 2000 and was admitted to the University of Texas at Austin (UT) on a provisional basis in August of the same year. The author completed his B.S. in Mechanical Engineering at UT in 2004 and immediately began his graduate studies in June of 2004 in the area of Nuclear Engineering at UT. The focus of the author's first graduate degree was the Reactor Accelerator Coupling Experiments (RACE) where he simulated and measured total flux and neutron energy spectra. The author completed his M.S. studies in Nuclear Engineering in May of 2006.

Work on his second graduate degree began in June of 2006 at UT with support from Sandia National Laboratory. The focus of his Doctorate research was multi-physics simulations of fast burst and externally driven nuclear reactors, where he made original contributions to the field of deterministic neutron transport and pulsed reactor simulations. The author plans to begin his professional career in June of 2008 at Schlumberger in Sugarland Texas as a reservoir engineer. A list of the author's publications is shown below.

T. Green, S. R. Biegalski, S. O’Kelly, “Neutron Energy Spectrum Determination and Flux Measurement Using Maxed, Gravel and MCNP for RACE Experiments,” accepted for publication in Journal of Radioanalytical and Nuclear Chemistry, 2008

S. R. Biegalski, E. Alvarez, T. Green, “Confirmation of germanium interference with hydrogen for prompt gamma-ray activation analysis,” Nuclear Instruments and Methods: B, 2005

W. S. Charlton, V. R. Taraknath Woddi, S. O’Kelly, T. Green, D. Beller, “Reactor-Accelerator Coupling Experiments (RACE): Heat Generation Rates Using W-Cu and U Targets,” Transactions of the American Nuclear Society, 2005

S.R. Biegalski, T.C. Green, E. Alvarez, S. Aghara, "Sources of Background at The University of Texas PGAA Facility," Journal of Radioanalytical and Nuclear Chemistry, 2004

S. R. Biegalski, T. C. Green, G. A. Sayre, W. C. Charlton, D. J. Dorsey, S. Landsberger, "Flux Weighted Efficiency Calibration of The University of Texas at Austin PGAA Facility," Journal of Radioanalytical and Nuclear Chemistry, 2004

Permanent address: 12826 Kingsbridge Ln., Houston, TX 77077

This dissertation was typed by the author.